Artificial Magnetic Materials: Limitations, Synthesis and Possibilities

by

Ali Kabiri

A thesis
presented to the University of Waterloo
in fulfillment of the
thesis requirement for the degree of
Doctor of Philosophy
in
Electrical and Computer Engineering

Waterloo, Ontario, Canada, 2010

I hereby declare that I am the sole author of this thesis. This is a true copy of the thesis, including any required final revisions, as accepted by my examiners.

I understand that my thesis may be made electronically available to the public.

Abstract

Artificial magnetic materials (AMMs) are a type of metamaterials which are engineered to exhibit desirable magnetic properties not found in nature. AMMs are realized by embedding electrically small metallic resonators aligned in parallel planes in a host dielectric medium. In the presence of a magnetic field, an electric current is induced on the inclusions leading to the emergence of an enhanced magnetic response inside the medium at the resonance frequency of the inclusions. AMMs with negative permeability are used to develop single negative, or double negative metamaterials. AMMs with enhanced positive permeability are used to provide magneto-dielectric materials at microwave or optical frequencies where the natural magnetic materials fail to work efficiently.

Artificial magnetic materials have proliferating applications in microwave and optical frequency region. Such applications include inversely refracting the light beam, invisibility cloaking, ultra miniaturizing and frequency bandwidth enhancing low profile antennas, planar superlensing, super-sensitive sensing, decoupling proximal high profile antennas, and enhancing solar cells efficiency, among others. AMMs have unique enabling features that allow for these important applications.

I derive fundamental limitations on the performance of artificial magnetic materials. The first limitation which depends on the generic model of permeability functions expresses that the frequency dispersion in an AMM is limited by the desired operational bandwidth. The other constraints are derived based on the geometrical limitations of inclusions. These limitations are calculated based on a circuit model. Therefore, a formulation for permeability and magnetic susceptibility of the media based on a circuit model is developed. The formulation is in terms of a geometrical parameter that represents the geometrical characteristics of the inclusions such as area, perimeter and curvature, and a physical parameter that represents the physical, structural and fabrication characteristics of the medium. The effect of the newly introduced parameters on the effective permeability of the medium and the magnetic loss tangent are studied. In addition, the constraints and relations are used to methodically design artificial magnetic material meeting specific operational requirements.

A novel design methodology based on an introduced analytical formulation for artificial magnetic material with desired properties is implemented. The synthesis methodology is performed in an iterative four-step algorithm. In the first step, the feasibility of the design is tested to meet the fundamental constraints. In consecutive steps, the geometrical and physical factors which are attributed to the area and perimeter of the inclusion are synthesized and calculated. An updated range of the inclusion's area and perimeter is obtained through consecutive iterations. Finally, the outcome of the iterative procedure is checked for geometrical realizability. The strategy behind the design methodology is generic and can be applied to any adopted circuit based model for AMMs.

Several generic geometries are introduced to realize any combination of geometrically realizable area and perimeter (s, l) pairs. A realizable geometry is referred to a contour that satisfies Dido's inequality, i.e., $l \geq \sqrt{2\pi s}$. The generic geometries introduced here can be used to fabricate feasible AMMs. The novel generic geometries not only can be used to enhance magnetic properties, but also they can be configured to provide specific permeability with desired dispersion function over a certain frequency bandwidth with a maximum magnetic loss tangent. The proposed generic geometries are parametric contours with uncorrelated perimeter and area function. Geometries are configured by tuning parameters in order to possess specified perimeter and surface area. The produced contour is considered as the inclusion's shape. The inclusions are accordingly termed Rose curve resonators (RCRs), Corrugated rectangular resonators (CRRs) and Sine oval resonators (SORs). Moreover, the detailed characteristics of the RCR are studied. The RCRs are used as complementary resonators in design of the ground plane in a microstrip stop-band filter, and as the substrate in design of a miniaturized patch antenna. The performance of new designs is compared with the counterpart devices, and the advantages are discussed.

Waterloo, August 15, 2010,

$\mathcal{A}.\mathcal{K}.$

Acknowledgement

First and foremost, I would like to record my gratitude to Professor Omar Ramahi for his supervision, suggestions and guidance since the very early stage of my research, as well as for giving me wise advice for my future throughout my PhD period. Above all and the most needed, he provided me with unflinching encouragement and support in unlimited ways. His truly scientific intuition and professional aptitude have made him a constant oasis of ideas and passions in science, in profession and in life, which exceptionally inspire and enrich my growth as a human, a student, a researcher and as a future scientist. Throughout my PhD year, he was supportive and encouraging in every aspect, and for this I feel greatly indebted to him more than he knows. I have had the opportunity to known Omar since 2001 when I first finished my masters and was granted a position in his group at Maryland University, College Park, but unfortunately refused the US visa. I was introduced to him by my former supervisor, Professor Kasra Barkeshli, and was in touch with him until I had the privilege of joining him at the University of Waterloo.

I would like to take this opportunity to send my blessings to Professor Barkeshli. He passed away due to an ALS disease. May his soul live in peace in heaven. He was the one who inspired me to pursue a career in electromagnetics, and solidified my knowledge foundation in this field. He supervised me from my undergrad senior years at Sharif University of Technology up to my Master graduation in academic and ethical excellence. He was, in all meaning, a compassionate and truly wonderful human being. He was a brilliant yet very humble scientist, and highly respected.

Many special thanks go in particular to Professor Saini Simarjeet. I am much indebted to him for his valuable advice and guidance during our occasional scientific discussions. He is an exceptionally adept and brilliant scientist. I am proud to say that I had the opportunity to take a course in "Photonic Integrated Circuits" and to work with him as a teaching assistant for two courses. I always benefited from his careful attention and support. I am very grateful for the high level of teaching experience that I received from him through involvement in the teaching process.

I convey special acknowledgement to Professor Achim Kempf for his advice and his willingness to share his bright thoughts with me whenever asked, which was very beneficial whilst shaping my ideas. I also took a few advanced courses in math and physics with him which always reminded me of my productive years in theoretical physics during my Masters. I always had something to take away from his lectures. While he taught, his strong understanding of the concepts always intrigued me to explore new ideas.

I owe a mountain of gratitude to my committee member Professor Ali Safavi-Naini for serving in my examination committee and for his invaluable feedback. I greatly appreciate the time he devoted and his sincere counsel.

I would like to thank Professor Steven Anlage for participating in my defence exam as the external faculty member. I recognize that this thesis is lengthy, and I therefore value his precious time and his feedback on my work.

Collective and individual acknowledgments are also owed to my colleagues Leila Yousefi, Muhammad Boybay, Babak Alavikia, Hussein Attia, Mohammed Bait-Suwailam, Zhao Ren and Nael Suwan. Their friendly discussions always inspire new ideas.

My heartfelt gratitude goes out especially to my first two mentors, my dear Mother and my dear Father. My parents deserve a special mention for their unwavering support and prayers. They taught me the basics of life. My Mother is the one who sincerely raised me with her caring and gentle love. My Father is the person who gave me his endless support and sacrificed so much for me since I was a child.

Words fail me to express my appreciation to my wife Farnoosh whose dedication, love, and persistent confidence in me has taken the load off my shoulders. I can never repay nor deservingly acknowledge the true dimensions of the debt I owe to my wife for gracing my life. She always heartened me with her cheerful disposition, wise counsel, and loyal support. She is the person who puts up with me and my idiosyncrasies. Therefore, I would also like to thank my Mother-in-law and Father-in-law for letting me take her hand in marriage, and warmly accepting me as a member of their family. They have always been a support to us, especially during my PhD years.

I wholeheartedly thank my Grandparents, and am deeply indebted to them. During several of my Masters years, I lived with them. Their love and support provided me with the energy and endurance to attain my highest potential. I would equally like to express my thanks to Adel and Erfan for being supportive and caring brothers.

This is dedicated to

My green country, Iran, *The Land of Nobles*, and

Those who believe that God gifted *freedom* and devote
their endeavors to flourish God's gift of freedom in the world.

Contents

List of Figures

xiii

List of Tables

List of Abbreviations

AMM	Artificial Magnetic Material
PBG	Photonic Bandgap Structure
ENG	ϵ-Negative Material
LHM	Left-Handed Material
DNG	Double Negative
SNG	Single Negative
MNG	μ-Negative Material
EMT	Effective Medium Theory
HT	Homogenization Theory
IR	Infra Red
PR	Plasmonic Resonance
MLT	Magnetic Loss Tangent
SRR	Split Ring Resonator
SR-R	Swiss Roll Resonator
MSRR	Modified SRR
bc-SRR	broadside coupled SRR
n-SR	n-turn Spiral Resonator
d-SRR	Double Split Ring Resonator
d-SSR	Double Split Square Resonator
s-SRR	Singly Split Ring Resonator
nc-SR	n-turn (circular) Spiral Resonator
nr-SR	n-turn (rectangular) Spiral Resonator
n-RCR	n^{th} order Rose Curve Resonator
HFR	Hilbert Fractal Resonator
CSRR	Complementary Split Ring Resonator
k-CRR	k^{th} order Corrugated Rectangular Resonator
RCR	Rose Curve Resonator
CRCR	Complementary Rose Curve Resonator
m-SOR	m^{th} order Sine Oval Resonator
CS-RR	Complimentary Spiral Ring Resonator

List of Symbols

c	speed of electromagnetic waves in vacuum
λ_0	wavelength of electromagnetic waves in vacuum
ω	angular frequency of an electromagnetic wave
ϵ_{eff}	effective permittivity
μ_{eff}	effective permeability
n_{eff}	effective refractive index
$\mathbf{k}$	wave vector
$\mathbf{E}$	electric field
$\mathbf{H}$	magnetic field
ϵ_r	relative permittivity of a material
μ_r	relative permeability of a material
χ_m	magnetic susceptibility
$\mathbf{M}$	magnetization vector
V_{emf}	electromotive force
H_{ind}	induced magnetic field
H_{ave}	averaged magnetic field
$\delta x, \quad \delta y, \quad \delta z$	x, y and z dimensions of a unit cell of an AMM
$\vec{\Gamma}[.]$	curve vector
m_{incl}	magnetic moment of inclusions
σ	conductivity
$R_0\sqrt{\omega}$	resistance per unit length of an inclusion
C_0	capacitance per unit length of an inclusion
L_0	inductance per unit area of an inclusion
F	geometrical factor of an inclusion
P	physical factor of an inclusion
l	perimeter of an inclusion
s	area of an inclusion
ϵ_0	permittivity of the free space
μ_0	permeability of the free space
$\mathcal{M}_{\text{factor}}$	Miniaturization Factor

α	dissipation factor
χ_0	magnetic susceptibility of lossless medium
ξ	loss function in the effective permeability of a medium
ω_0	resonance frequency of an inclusion
Ω	normalized frequency with respect to the resonance frequency
BW	fequency bandwidth
$\mathcal{R}e$	real part of a complex function
$\mathcal{I}m$	imaginary part of a complex function
f_{op}	operational frequency
χ_0	magnetic susceptibility of lossless medium
(s, l)	($area, perimeter$) pair of geometrically relizable curves
$Pr \quad Pr[.]$	perimeter function of a curve
$Ar \quad Ar[.]$	area function of a curve
$R_n(r, a)$	n^{th} order Rose curve of radius r and amplitude a
$C_k^i(a, h)$	i sided , k^{th} order Corrugated rectangular curve
$S_m(b, a_j)$	m^{th} order Sine oval curve
$\kappa(\theta)$	curvature function
Λ	curvature integral

No problem is too small or too trivial
if we can really do something about it.

Richard Feynman

Chapter 1

Preface

1.1 Thesis

The marvel of *metamaterials* has engrossed numerous minds since the last decade. Scientists, science journalists as well as fictionists are fascinated and astonished in its incredible enabling potential to realize unique, exotic and unprecedented applications. Some scientists count the advent of metamaterials as an evolutionary event in the field of electromagnetics, optics and electronics. A metamaterial-*beyond* natural material- discloses properties not readily found in natural materials. Applications include inversely refracting the light beam, invisibility cloaking, ultra miniaturizing low profile antennas, planar superlensing, super-sensitive sensing, and enhancing solar cell efficiency, among others. Metamaterials have enabling features that allow for these innovative applications. However, some scientists are not yet contented that metamaterials reveal any novelty but rather believe that they are a restoration of an old, well-known concept which has recently been revisited and spuriously boasted. That is, a medium composed of inclusions reveals extraordinary properties based on the geometry and structure of inclusions while exposed to an electromagnetic radiation. Whether or not this concept is believed to be a novel idea, the advent of modern fabrication technology along with the outburst of an interest in realization of far-reaching applications have given a high credibility to metamaterials in the scientific community.

Metamaterials can be categorized into various classes. If the medium is engineered

with broken loop metallic inclusions, the magnetization of the medium is enhanced while impinged by an electromagnetic field radiation. This engineered medium referred to as an artificial magnetic material (AMM). This dissertation focuses particularly on the magnetic class of metamaterials in the microwave frequency. It discusses the limitations, synthesis and possibilities of artificial magnetic materials.

First, a fundamental limitation on the minimum variation of the magnetic susceptibility, and accordingly the permeability dispersion over a frequency bandwidth, is calculated. This limitation is used as a rule of thumb by designers of AMMs to define a proper measure on the minimum required flatness of engineered AMMs. This limit also provides insight into the minimum dispersion that should be reckoned with when using an AMM for any application such as the antenna miniaturization.

Next, a methodology for designing of AMMs is developed to characterize the inclusions' shape. The main novelty is that a *recipe* is provided to design artificial magnetic materials fulfilling certain specifications. The proposed design recipe can be followed by a designer of the artificial magnetic medium even if the designer experience on the topic is limited. The design methodology can be linked with many circuit models available in the literature. In this work, I employ the circuit model which is commonly adopted in the literature [1]-[4], and then I suitably reformulate the magnetic susceptibility for the design purposes.

As the design methodology is generic, it does not prescribe any particular geometry, but it merely determines the geometrical properties of the inclusion. Hence, for completeness, I introduce three families of parametric geometries reconfigurable for *all* realizable geometries. Then, the specific shape is characterized for each class of geometries. To verify the proposed technique, the designed artificial media are numerically simulated using full-wave three dimensional electromagnetic simulators. The introduced inclusions are the Rose curve resonators (RCRs), the Corrugated rectangular resonators (CRRs) and the Sine oval resonators (SORs).

Finally, an AMM composed of Rose curve resonators is studied in more details to be used in potential applications. Two devices, a microstrip band-stop filter and a miniaturized patch antenna, are introduced. The devices exploit Rose curve artificial materials to miniaturize the devices size. The devices are simulated by using full-wave simulator software packages to characterize their features.

2

1.2   Organization

The thesis contains eight chapters including preface and afterword and five appendices.

In chapter 2, the concept of an artificial material is defined, and its feasible electromagnetic features are discussed. The discussion includes the plausibility of defining effective constitutive parameters and the range of variation of these parameters. It is also shown that the discussed parameters meet the causality relation. In addition, artificial magnetic materials are defined as a separate category of artificial materials which provides magnetism. Thereafter, various composite structures, available analytical models describing the magnetic behavior of the structures as well as some potential applications are introduced.

In chapter 3, a commonly accepted circuit model for periodic arrays of metallic broken loops is presented. The model describes the magnetic behavior of an AMM composed of an arbitrary shape inclusions in terms of lumped elements attributed to capacitance of metallic traces and the inductance of the looped metallic inclusions. The model's capacitance and inductance are in connection with the area and perimeter of an inclusion. A heuristic formulation is derived for the magnetic susceptibility and permeability of an AMM based on a unique strategy of encapsulating the geometrical and structural factors. The novel formulation is later used for design of AMMs.

In chapter 4, fundamental limitations of artificial magnetic materials are derived. These limitation includes an equality on dispersive characteristic of the medium, a relationship between the maximum achievable permeability and the magnetic loss limit in the medium. Proper graphs as a design factbook for designer of artificial magnetic materials is presented.

In chapter 5, guidelines for a methodic design of an artificial magnetic material fulfilling a particular specification is developed. The design recipe is implemented on a design case study, and each step is described in details. The output of the proposed recipe is geometrical characteristics of the metallic inclusions, i.e., the area and the perimeter. The methodology is limited to artificial magnetic materials composed of metallic objects and operating in the microwave region of the electromagnetic frequency spectrum. The design algorithm is also presented in a comprehensive flowchart diagram, and implemented in a software package to simplify and expedite a design

task. The software receives the magnetic properties of a desired AMM as an input, and produces the geometrical parameters of inclusions as an output. The software code is also available for academic purposes.

In chapter 6, three families of parametric curves are introduced. These curves are considered as a generic inclusions for any feasible AMMs. Moreover, these curves are customized to mimic the area and perimeter calculated in the design procedure. Thereafter, AMMs composed of the inclusions of each type are simulated with full-wave electromagnetic simulators. The results are compared with desired properties and design errors are estimated. These parametric curves are referred to as Rose curve resonators (RCRs), Corrugated rectangular resonators (CRRs) and Sine oval resonators (SORs). A software package is also implemented to automatically configure each curve in order to have a specific area and perimeter. The software is also available for academic purposes. Next, an AMM composed of the Rose curve inclusions is investigated further and its unique properties are introduced for suitable applications. In addition, the ubiquitous split ring resonator and other inclusion geometry were compared and their inability to be nominated as a generic inclusion is explicated.

In chapter 7, applying the RCRs, two key applications are introduced. The proposed devices are a *small-form* microstrip stop-band filter with a complementary Rose curve ground plane and an *ultra-miniaturized* low profile antenna with a substrate of Rose curve resonators. Devices which embedding Rose curve inclusions show enhanced features. The features are tested and simulated with a full-wave software simulator.

Chapter 2

Introduction

The world of electromagnetics has revealed recent breakthroughs in diverse areas of science and technology such as telecommunications, biomedical imaging, chemical spectroscopy and sub-wavelength sensing. Much of the progresses has been accomplished by the advent of complex engineered media especially at the mesoscopic scale. At the dawn of the twenty first century, a family of artificial (or engineered) media known with the generic title of *Metamaterials* has enabled incredible functionalities not achievable through the natural materials. It has been known for at least half a century that periodically or aperiodically structured electrically small particles alter the electromagnetic properties of the host medium. However, due to the ease of fabrication techniques and the need for new applications, the exceptional behaviors of such structures have recently received considerable attention from the scientific community, as witnessed by the exponential growth of the number of related publications. The surge of interest in the development of metamaterials has ramified in experimental verifications, theoretical explications and technical applications, but not yet ratified in methodical realization for commercially mass productions.

2.1   Artificial Materials

In microwave and sub-microwave frequencies, naturally occurring materials are limited to certain levels of polarization and magnetization. Even if certain levels of magnetization and polarization are achievable, the materials suffer from high electric

and magnetic loss. For example, ferrite composites are strongly magnetized yet they suffer from appreciable magnetic loss and high resistivity in the microwave frequency range [5], [6]. Due to these limitations, artificially engineered materials are designed to provide specific permeability and permittivity over microwave frequency ranges.

An artificial material, also termed as a *metamaterial,* is an engineered structure that has electromagnetic properties which are not readily available in nature. The metamaterial is a material medium which is aggregated with electrically small inclusions. The inclusions are periodically or aperiodically arranged in the host medium. The engineered structure alters and advances the electromagnetic properties of the host medium due to mainly the inclusions' resonating behavior in presence of an electromagnetic excitation [7]. While such a composite is excited by an electromagnetic radiation whose wavelength is much larger than inclusions' dimension and separation, the medium exhibits unique behaviors not covered by ordinary materials.

From electromagnetic point of view, the heterogenous artificial structure can be featured as a homogenous medium ascribed by an *effective* material parameters, an effective permittivity ϵ_{eff} and an effective permeability μ_{eff}. The effective description would be valid if any length scale d associated with the structure is much smaller than the electromagnetic radiation wavelength λ,

$$d \ll \lambda = 2\pi c/\omega \tag{2.1}$$

where ω is the angular frequency of the electromagnetic radiation. This condition ensures that electromagnetic wave is refracted and not diffracted in the underlying medium, and therefore, the effective permittivity and permeability are plausible concepts. Note that, unlike the photonic bandgap structure (PBG), metamaterials are not required to be periodic. However, in this context I mainly seek the properties of periodically structured metamaterials.

The inequality (2.1) defines the effective medium limit [8], [9]. Thus, even though the composite medium is complex, the electromagnetic response of the structure can be sought through the effective response functions of $\epsilon_{\text{eff}}(\omega)$ and $\mu_{\text{eff}}(\omega)$. Hence, the source-free Maxwell's equations with a set of constitutive relations defined by $\epsilon_{\text{eff}}(\omega)$ and $\mu_{\text{eff}}(\omega)$ describe the electromagnetic properties of the artificial medium. Design of an artificial electromagnetic material with ϵ_{eff} and μ_{eff} is motivating if one can achieve values of the effective functions which are not normally found in natural materials.

However, a significant question is that whether there are limitations on ϵ_{eff} and μ_{eff}, and if so, what are those limitations? I particularly address this question later in the light of effective medium models for μ_{eff}. However, in general, for passive linear media, the analysis of $\epsilon_{\text{eff}}(\omega)$ and $\mu_{\text{eff}}(\omega)$ leads to the following conditions [10]:

$$\lim_{\omega \to \infty} \epsilon_{\text{eff}}(\omega) = 1 \quad \text{and} \quad \lim_{\omega \to \infty} \mu_{\text{eff}}(\omega) = 1 \tag{2.2}$$

$$\frac{\mathrm{d}(\omega \epsilon_{\text{eff}}(\omega))}{\mathrm{d}\omega} > 1 \quad \text{and} \quad \frac{\mathrm{d}(\omega \mu_{\text{eff}}(\omega))}{\mathrm{d}\omega} > 1 \tag{2.3}$$

The relations (2.2) imply that beyond some frequency, materials cannot be polarized or magnetized, thus, the effective permittivity and permeability are limited to unity. At extremely high frequencies, the assumption in (2.1) is violated, and in principle, it is not valid to introduce effective material parameters. The second conditions in (2.3), derived from the Kramers-Kronig relation [1][10], [11], is a consequence of the causality principle. These conditions apply a restriction on the frequency dispersion relation of the permittivity and permeability functions. In fact, the conditions (2.3) imply that the absorbed energy density in a passive linear lossless medium must always be larger than the energy density of the same field in vacuum.

Fig.2.1 shows the various possible combinations of $\epsilon_{\text{eff}}(\omega)$ and $\mu_{\text{eff}}(\omega)$. Consider the propagation of an electromagnetic wave in the medium. The refractive index $n(\omega)$ and the wave vector k are defined as:

$$n = \sqrt{\epsilon_{\text{eff}}(\omega)\mu_{\text{eff}}(\omega)} \tag{2.4}$$

$$k = \frac{\omega}{c}n(\omega) \tag{2.5}$$

In the first quadrant, since $\epsilon_{\text{eff}}(\omega)\mu_{\text{eff}}(\omega) > 0$, and hence, the wave vector is a real number. All materials at least for a band of frequency lie in this quadrant. The second quadrant are epsilon negative materials (ENGs), and provides an imaginary k which implies that electromagnetic waves are evanescent. The noble metals at high frequencies have negative permittivity. Another example is the plasma medium such as the ionosphere.

---

[1]More details on Kramers-Kronig relations and causality constraints is provided in chapter 3.

In the lower half-plane of $\epsilon - \mu$ space in Fig.2.1, μ_{eff} is negative [12]. Note that the occurrence of negative permeability in materials does not contradict with causality due to the fact that the second inequality in relations (2.3) predicts this property through sufficient frequency dispersion. Thus, realization of that through reconstructing a composite medium has motivated many scientists in the last decade. In the third quadrant, the permittivity and permeability functions are simultaneously negative [13]. The materials in this quadrant are refereed to as left-handed materials (LHMs) by Veselago [14] due to the fact that the triad $(\mathbf{E}, \mathbf{H}, \mathbf{k})$ forms a left-handed system, where $\mathbf{E}$ and $\mathbf{H}$ correspond to the electric and magnetic fields, respectively. The left-handedness can clearly be seen through Maxwell's equation written for a harmonic electromagnetic field,

$$
\begin{aligned}
\mathbf{k} \times \mathbf{E} &= \frac{\omega}{c} \mu_0 \mu_{\text{eff}}(\omega) \mathbf{H} & (2.6) \\
\mathbf{k} \times \mathbf{H} &= -\frac{\omega}{c} \epsilon_0 \epsilon_{\text{eff}}(\omega) \mathbf{E} & (2.7)
\end{aligned}
$$

Interesting consequence of left-handedness is that the group velocity and phase velocity are in opposite direction which is known as backward propagation of electromagnetic waves in double negative (DNG) media. As a consequence, the refractive index $n(\omega)$ is negative in DNG materials [15], [16], [17], [18]. Negative refractive index (NRI) materials have been fabricated and measured [19], [20]. The quadrant (IV) specifies materials with negative permeability and positive permittivity functions. This single negative (SNG) region is referred to as μ-negative materials (MNGs).

One important consequence of negativity of a medium parameter is the amplification of evanescent waves in the SNG medium, which leads to a perfect lensing and sub-wavelength imaging, a high-resolution imaging beyond the diffraction limit [21], [22], [23], [24], [25], [26]. Metamaterials open the door to new applications such as invisibility cloaking and the synthesis of materials index-matched to air, for potential enhancement of light collection in solar cells.

Metamaterials based on their heterogeneities are classified in different types. Metamaterials which are designed to enhance the magnetic properties of the host medium are referred to as artificial magnetic materials (AMM). The inclusions in this type respond significantly to the magnetic field. The limitations, synthesis and applications
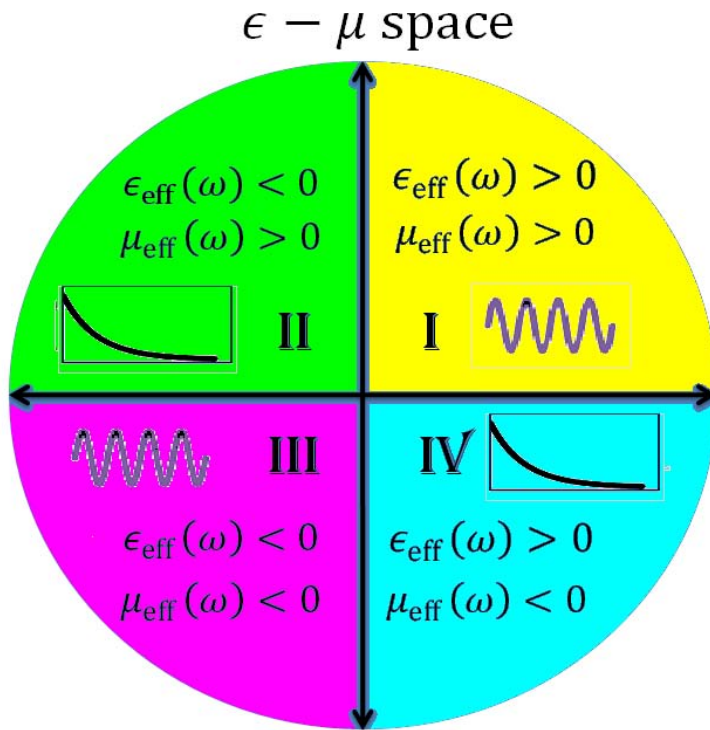
Figure 2.1: Effective material parameters represented on a set of $\epsilon - \mu$ axes)

of artificial magnetic materials in microwave frequency are the main subject of this thesis.

2.2 Artificial Magnetic Materials

Among artificial structures, those exhibiting magnetic properties have received tremendous attention because of not only providing positive or even negative permeability values at radio frequencies but also being an enabling technology in several key applications. Emergence of new magnetic features by means of artificial magnetic materials has affected proliferating wireless systems such as the antenna technology useful in telecommunication systems and near-field sensing probes such as portable ground-penetrating sensors.

An artificial magnetic material (AMM) known as a magnetic metamaterial is a

composition of electrically small metallic broken-loop inclusions, aligned in parallel planes perpendicular to the direction of incident magnetic field. The incident magnetic field induces electric current on the inclusions leading the emergence of an enhanced magnetic response inside the medium at the vicinity of the LC resonances of the looped ring.

In the microwave region, metals can be approximated as perfect conductors as the skin depth is much smaller than the feature size of the structure. Thus, the resonance frequencies and dispersive behavior of AMMs are determined entirely by the geometry and size of the metallic broken-loop inclusions. Hence, the LC resonances of perfectly conducting metallic structures are referred to as geometric LC resonances. The geometric-circuit analysis of AMMs can be extended roughly up to mid-IR frequencies where the size of metallic component are comparable to or less than the skin depth [27], [28]. However, in infra-red (IR) and optical frequencies, the electromagnetic properties of metals dominate, and the magnetic response of inclusions is due to electric and magnetic plasmonic resonances (PRs). For optical magnetism, various shapes such as parallel plates, fishnet, u-shape and loop-dots magnetically respond in presence of electromagnetic field [29]-[31].

The first inclusion, a single broken-loop, was proposed by Schelkunov and Friis in 1950's [32]. Three decades later, Hardy and Whitehead introduced a cylindrical sheet having a gap on its surface parallel to a cylinder axis to exhibit magnetic behavior [33]. In addition, Kostin and Shevchenko arranged the broken loops in a periodic lattice to create paramagnetic properties in a medium [34], [35].

An inundation of publication commenced by the appearance of Pendrys seminal work on the feasibility of creating magnetism from metallic conductors [1]. The ever-renowned split ring resonators (SRRs) and Swiss roll resonators (SR-Rs), a cylindrical wounded metal sheet, were introduced by Pendry *et al.* [1]. Since then, to obtain enhanced magnetic properties, numerous inclusions having various geometrical configurations have been proposed in the literature [2]-[38]. Fig.2.2 shows a sample set of metallic broken-loop inclusions presented in the literature as building blocks of AMMs. Each proposed structure provides its own advantages and disadvantages in terms of resultant permeability, dispersive characteristics and dissipation factor. A modified SRR (m-SRR), or broadside coupled SRR (bc-SRR) was introduced in [36]. In [2], a new configuration named metasolenoid was proposed with the potential to
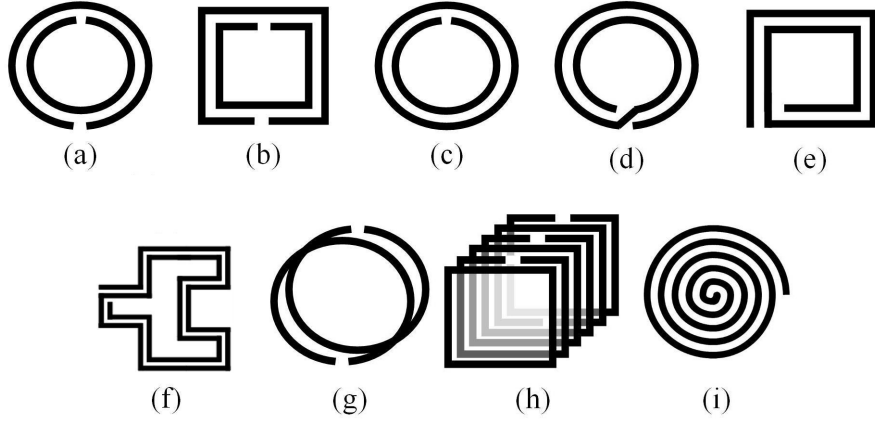
Figure 2.2: Different inclusions used to implement artificial magnetic materials. (a) Double Split Ring Resonators (d-SRR), (b) Double Split Square Resonators (d-SSR), (c) Singly Split Ring Resonator (s-SRR), (d) Two-turn (circular) Spiral Resonator (2c-SR), (e) Two-turn (rectangular) Spiral Resonator (2r-SR), (f) Hilbert Fractal Resonator, (g) Modified Ring Resonator (m-SRR), (h) Metasolenoid, (i) cross section of a Swiss Roll (SR).

provide higher permeability compared to SRR and m-SRR configurations, in [38], the n-turn Spiral Resonator (n-SR) configuration was introduced, and in [37], [39]-[43] inclusions based on fractal curves were proposed to reduce the size of inclusions. Note that all various inclusions which are electrically small compared to incident electromagnetic wavelength are being exploited as a building block of AMM slabs.

A number of analytical models were developed to explicate the physics behind the peculiar characteristics of AMMs [1, 36, 44, 45]. When the periodicity and the size of the inclusions are small compared to the wavelength, electromagnetic mixing formulas such effective medium theory (EMT) and homogenization theories (HT) can be used to derive the effective permeability and permittivity for composite media [46]. Using the EMT technique, Pendry *et al.* calculated the effective permeability of a medium containing looped metallic inclusions such as metal cylinders, Swiss Rolls, and SRRs and showed that negative permeability can be obtained in microwave frequencies [1]. EMT allows identifying the average field propagating inside a composite medium with respect to the field propagating inside a homogeneous medium with the same effective electrical characteristic [47].

The circuit-based models of metamaterials, especially artificial magnetic materials, were developed to capture either the behavior of the entire composite medium or the behavior of the separate inclusions [2]. These models, which depend on the geometry and dimension of the inclusions, have been proposed to describe the magnetic behavior of the inclusions rather than the electric behavior.

Different shapes of inclusions have been studied in the literature. The SRR consists of two concentric metallic broken rings printed on a dielectric circuit board. Marques *et al.* presented a quasi-static study of the SRR by proposing a circuit model for the capacitive behavior of the inclusions [36]. Sauviac *et al.* and Shamonin *et al.* proposed more accurate models for SRR inclusions [44], [48]. Sauviac *et al.* used a detailed circuit-based model to extract the magnetic and electric polarization of the SRR [44]. Shamonin *et al.* expanded a set of differential equations describing the current and voltage distribution in SRRs [48]. Most recently, Ikonen *et al.* offered a generalized equivalent-circuit model which mimics the experimental permeability function [49].

The unique properties of metamaterials have encouraged researchers to use metamaterial slabs in various microwave applications including using metamaterials as a substrate or a superstrate for enhancing low-profile antenna performance [50], [51], as a probe for the near-field imaging [52], or for shielding applications and microwave absorbers [53]-[55]. In [50], extensive research was done on the performance of developed engineered magnetic materials when used for antenna miniaturization. It was shown in [37] that new inclusions can provide lower dispersion, nevertheless, high magnetic losses persist. In [56], the effective properties of the medium are expressed in terms of the Q-factor. It was claimed that by measuring the Q-factor of a single fabricated SRR, the effective permeability and permittivity of an AMM can be estimated to better than 20% accuracy. In addition, in [56], a lower limit for the magnetic loss tangent was proposed for frequencies up to about 1GHz.

Chapter 3

Formulating Artificial Magnetic Materials

Various geometrical patterns have been proposed to develop artificial magnetic materials [1, 2, 57, 38]. The key idea to produce magnetic properties is to generate a circulating electric current that mimics a magnetic dipole. The current circulation occurs in a metallic contour leading to increased magnetic flux. To generate a *capacitive* property, another metallic contour is positioned concentrically adjacent to the first contour. The coupling between the two contours creates capacitance between them. The capacitive load with the solenoidal inductance of the rings leading to a resonating behavior at a frequency. As a result, the magnetic field is enhanced in the medium, and it to a net effective increase in the permeability of the medium. The resultant capacitance and inductance create the potential for resonance at a certain frequency, henceforth referred to as the *resonance frequency*.

Fig.2.2 (from chapter 2) shows a sample set of metallic loop resonators presented in the literature as building blocks of AMMs. The ring resonators in a unit cell are categorized in two general geometrical patterns based on the number of loops of rings and the coupling scheme between rings. The first category consists of metallic rings with (1) multiple elements such as double split ring resonators (Fig.2.2-a) and double split square ring resonators (Fig.2.2-b) or (2) single element but spiral (Fig.2.2-d,-e,-f) or helical shape [38], [58]. The second category divides ring resonators based on the coupling scheme established between metallic rings of a unit cell. The coupling

t
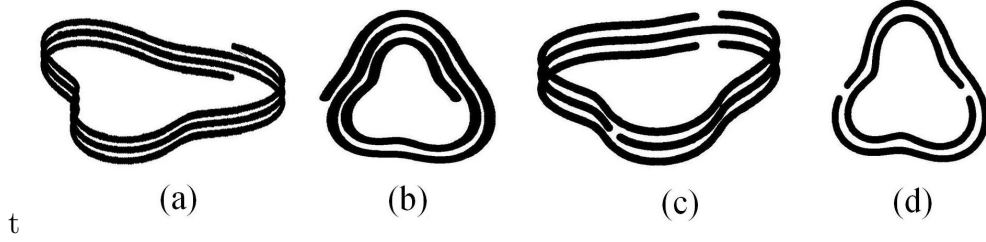
Figure 3.1: Different categories of inclusions. (a) Broadside-coupled 3-turn helical inclusion, (b) Edge-coupled 2.5-turn spiral inclusion , (c) Broadside-coupled triple split looped inclusion, (e) Edge-coupled double split looped inclusion.
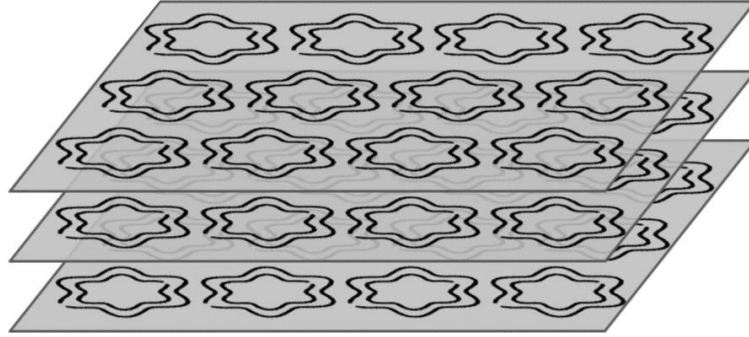
Figure 3.2: A metamaterial slab (an artificial composite of metallic inclusions) composed of generic metallic broken loop inclusion

schemes are *edge-coupled*, if the rings are concentric in a plane, and *broadside-coupled*, if the rings are parallel along their axes [57]. Fig.3.1 shows an arbitrary inclusions contour in different categories. The artificial magnetic medium is then created by periodically or aperiodically reproducing the contour. Fig. 3.2 shows an artificial magnetic medium composed of periodic unit cells of generic metallic rings.

As the inclusions were arranged in parallel planes, the AMM in Fig.3.2 is essentially anisotropic structure, and provides magnetic moment vectors only in the direction perpendicular to the inclusion surface. Hence, the magnetic permeability $\bar{\bar{\mu}}_{\text{eff}}$ describing the medium is a tensor. If we consider the inclusions distributed perpendicular to y-axis the induced magnetic moments are in y direction and the permeability in x and z directions is equal to that of the host media which is unity for nonmagnetic host medium. Therefore, the artificial magnetic material will be anisotropic with permeability tensor of

14

$$\bar{\bar{\mu}}_{\text{eff}} = \begin{pmatrix} \mu_r & 0 & 0 \\ 0 & \mu_{\text{eff}} & 0 \\ 0 & 0 & \mu_r \end{pmatrix} \tag{3.1}$$

where μ_r is the permeability of the host medium. To achieve an isotropic AMM the same inclusions can be rearranged in parallel planes intersecting the plane of inclusions, i.e., in x and z directions. Therefore, a unit cell is designed as a cubit cell with inclusions attached on the three walls, i.e., in xy, xz and yz planes [59]. Also, it has been discussed that among various orientations of the rings, for an isotropic response the rings can only intersect along symmetric points [1] [60], [61].

In this chapter, a general formulation describing the magnetic behavior of an AMM composed of generic inclusions is derived. The formulation is based on a popular circuit model in the literature. In addition , the magnetic susceptibility and permeability functions are reformulation is in a heuristic formalism suitable for further study and synthesis of AMMs.

3.1 Characterization of an AMM

In an artificial medium impinged with an external monochromatic magnetic field $\mathbf{H}_{ext}$, the effective magnetic susceptibility represents the degree of magnetization of the medium in response to an applied magnetic field, defined as:

$$\chi_m = \frac{M_{med}}{H_{ave}} \tag{3.2}$$

where H_{ave}, the magnitude of an averaged (macroscopic) magnetic field $\mathbf{H}_{ave}$ inside the medium, is defined by averaging the magnetic field along the sides of the unit cell, and M_{med} is the magnitude of the magnetization vector of the medium. Magnetization

---

[1]A precise consideration of the behavior of the inclusions shows that near the resonance frequency, the particles response to an external magnetic field not only as a strong magnetic dipole, but also as a strong electric dipole. This behavior makes the structure bi-anisotropic. This effect is reduced for the frequency of operation far enough from the resonance frequency, and it becomes negligible value for inclusions coupled along their broadside. In this work, I only address the magnetic behavior of the structures.

is defined as the magnetic moment per volume. When the magnetic dipole moments are in phase with the averaged magnetic field, the effective magnetic susceptibility become larger than zero (correspondingly, the effective permeability become larger than unity) causing the medium to be magnetized. Note that in some special cases such as placing an AMM inside a long solenoid, $\mathbf{H}_{ext} = \mathbf{H}_{ave}$ [1], [2], [60].

An expression for the magnetic susceptibility is formulated by considering an AMM with a general inclusion's shape. Fig. 3.3 shows unit cell of a generic inclusion in perspective. Fig. 3.3(a), (b) and (c) show a two-turn split ring resonator with an arbitrary trace geometry denoted by $\Gamma(s, l)$. Γ is characterized by s and l , the area and the perimeter of the inclusion, respectively. Fig. 3.3(e) and Fig. 3.3(f) show an edge-coupled and a broadside-coupled ring resonator, respectively. The unit sample in Fig. 3.3 has a height of δz width of δx and depth of δy. The area of the cell is $A = \delta x \delta z$ and its volume is $V = A \delta y = \delta x \delta y \delta z$. The conductor material used in printed inclusions is assumed to have electric conductivity of σ, width of b, and height of t. Without loss of generality, we can assume the other (twin) conductor is positioned either inside and follow the shape of the outer conductor with the uniform gap g (see Fig. 3.3(e)) or parallel to the former and separated by a distance of g (see Fig. 3.3(f)). A dense array can be arranged in a periodic fashion, spread perpendicular to y-axis and along the x, y and z axes to produce the AMM.

When an external monochromatic magnetic field $\mathbf{H}_{ext}$ is applied, it induces a circulating current on the metallic inclusion. As a consequence, an induced magnetic field $\mathbf{H}_{ind}$ develops. Based on Faraday's law an electromotive force, V_{emf}, develops on the metallic rings given by:

$$V_{emf} = -j\omega\mu_0 n s \left(H_{ave} + H_{ind}\right) \tag{3.3}$$

$$H_{ind} = \frac{nI}{\delta y} \tag{3.4}$$

where H_{ind} is the magnitude of the vectors $\mathbf{H}_{ind}$, I is the induced current, n is the number of wire turns that carries the induced current ($n = 2$ for Fig. 2(a) [51], and $n = 1$ for Figs. 2(b) and 2(c)) [2], ω is the angular frequency of the applied field, and μ_0 is the permeability of air. The inclusions are also distributed in the y-direction (along their axis), and, thus, the produced magnetic field in each column passes
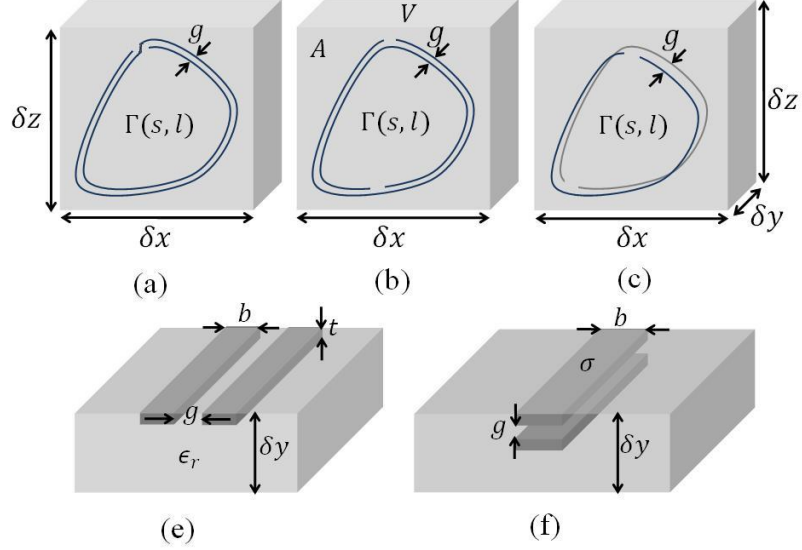
Figure 3.3: (a) A configuration of a unit cell of an AMM with an arbitrary shape SRR. V and A represent the volume and surface area of the unit cell. The inclusions' contour, area and perimeter are denoted by Γ, s, and l, respectively. (b) Edge-coupled inclusion, (c) Broadside-coupled inclusion.

through the other inclusions of the same stack. For evaluating the magnetic field, δy is considered to be smaller than the largest dimension of the inclusion. Therefore, each column of inclusions in the y-direction can properly be modeled as a solenoid with the magnetic field given by (3.4).

The magnetic dipole moment of inclusions can be simply derived:

$$m_{incl} = nIs \qquad (3.5)$$

To derive an explicit relation for the magnetic susceptibility based on physical and geometrical characteristics of an inclusion, I propose a circuit model for the inclusions. Accordingly, the induced V_{emf} dropped over any inclusion can be expressed by the impedance of the rings and the induced current on the inclusion as [2]:

$$V_{emf} = I(R + \frac{1}{j\omega C}) \qquad (3.6)$$

where the effective impedance of the loops has been modeled with a resistor, R, in

17

series with a capacitor, C [2]. The main focus of this work in on frequencies less than resonance frequency of the inclusions. Therefore, the skin depth of the conductor determines the relationship between the resistance and the frequency. Therefore, R is given by:

$$R = \frac{1}{\delta\sigma}\left(\frac{n'l}{b}\right) = \frac{n'l}{b}\left(\sqrt{\frac{\mu_0\omega}{2\sigma}}\right) = R_0 l\sqrt{\omega} \tag{3.8}$$

where n' is the number of wire turns which contribute to ohmic losses ($n' = 2$ for case (a), (b) and (c)), and R_0 is

$$R_0 = \frac{n'}{b}\left(\sqrt{\frac{\mu_0}{2\sigma}}\right). \tag{3.9}$$

The relative permeability of the conductor in (3.9) was considered to be 1. Also, C is given by

$$C = C_0 l \tag{3.10}$$

$R_0\sqrt{\omega}$, and C_0 are defined as the per-unit-length resistance and the per-unit-length capacitance of the inclusion. The per-unit-length capacitance, for the edge-coupled inclusion can be expressed as [63]:

$$C_0 = \epsilon_0\epsilon_r\frac{F\left(\sqrt{1-u^2}, \frac{\pi}{2}\right)}{F\left(u, \frac{\pi}{2}\right)}, \qquad u = \frac{g}{2b+g} \tag{3.11}$$

and for the broadside-coupled inclusion as [2]:

$$C_0 = \frac{1}{4}\epsilon_0\epsilon_r\frac{F\left(u, \frac{\pi}{2}\right)}{F\left(\sqrt{1-u^2}, \frac{\pi}{2}\right)}, \qquad u = \tanh\left(\frac{\pi b}{2g}\right) \tag{3.12}$$

---

[2] The inductance of the ring's trace was not considered in the formula due to the small value of the inductive impedance compare to capacitive impedance of an inclusion. However, for obtaining further accuracy in predicting the magnetic behavior of an AMM, it can be included in the model. An approximate formula for inductance of a round loop of radius R made of a conducting strip of width w can be read as [44], [62], [11]:

$$L = \mu_0 R\left[\ln\left(\frac{32R}{c}\right) - 2\right]. \tag{3.7}$$

where ϵ_r is the relative permittivity of the host substrate, and $F(k, \phi)$ is the elliptical Integral of the first kind:

$$F(k, \phi) = \int_0^\phi \frac{d\theta}{\sqrt{1 - k^2 \sin^2 \theta}} \tag{3.13}$$

Note that in the case of *metasolenoid* [2] the gap, g, between the parallel inclusions is equal to the unit cell height, δy.

Equating (3.3) and (3.6), and using (3.4) and (3.2), the effective magnetic susceptibility can be expressed as:

$$\chi_m = -\frac{s}{A} \left(\frac{j\omega L}{R + j\omega L + \frac{1}{j\omega C}} \right) = \frac{s}{A} \left(\frac{\omega^2 LC}{1 - \omega^2 LC + j\omega RC} \right) \tag{3.14}$$

where the inductance, L, is defined as:

$$L = \left(\frac{n^2 \mu_0}{\delta y} \right) s = L_0 s \tag{3.15}$$

and L_0 is the per-unit-area inductance of the inclusion [3].

Substituting the resistance, inductance and capacitance from equation (3.8), (3.10) and (3.15) in (3.14) results in an expression for the net magnetic susceptibility as a function of the geometrical and physical properties of the contour Γ:

$$\chi_m(\omega) = \frac{1}{A} \left(\frac{L_0 C_0 \omega^2 s^2 l}{1 - L_0 C_0 \omega^2 sl + j R_0 C_0 \omega \sqrt{\omega} \, l^2} \right) \tag{3.16}$$

As observed in (3.16), the susceptibility is related to the perimeter l and area s of the contour. Thus, inclusions with different topologies but having the same perimeter and area, result in the same values for the magnetic susceptibility and permeability (assuming all other physical parameters remain constant). Equation (3.16) can be rewritten as:

$$\chi_m(\omega; s, l) = \frac{\left(\frac{\omega}{\omega_0'} \right)^2 \left(\frac{s}{A} \right) sl}{1 - \left(\frac{\omega}{\omega_0'} \right)^2 sl + j \left(\frac{\omega}{\omega_0''} \right)^{3/2} l^2} \tag{3.17}$$

---

[3]For obtaining more accuracy in the circuit model, the capacitance produced over the inclusion slit can be considered as a small correction in the calculation of the circuit model.

where ω'_0, ω''_0 are defined as

$$\omega'^2_0 = \frac{1}{L_0 C_0} \;, \qquad \omega''^3_0 = \frac{1}{(R_0 C_0)^2}$$

ω'_0 and ω''_0 have the dimensions of $(meter)^{\frac{3}{2}}/sec$ and $(sec)^{\frac{3}{2}}/(meter)^2$, respectively.

The perimeter and area of the contour, however, are not independent parameters. They are related according to the following relation:

$$\omega_0 = \frac{1}{\sqrt{LC}} = \frac{1}{\sqrt{L_0 C_0 sl}} = \frac{\mathcal{Q}}{\times}(sl)^{\frac{-1}{2}} \tag{3.18}$$

where $\mathcal{Q}$ is a function of the structural and electrical properties of the inclusions and host medium. Hence,

$$s\,l = \left(\frac{\omega'_0}{\omega_0}\right)^2 \tag{3.19}$$

where the frequency ω_0 is considered as the *resonance* frequency of the artificial magnetic medium.

Considering equation (3.19), grouping all the physical parameters into one parameter P, and defining Ω as the normalized frequency (with respect to the resonance frequency ω_0), (3.17) can be rewritten as [4]:

---

[4]In the Literature, a prevalently accepted magnetic susceptibility model as an effective medium description of an AMM expressed as:

$$\chi_m(\omega) = \frac{K\omega^2}{\omega_0^2 - \omega^2 + j\gamma\omega} \tag{3.20}$$

where K, $(0 < K < 1)$, is the amplitude factor, ω_0 is the resonant frequency of the inclusions, defined to be the frequency at which χ_m is purely imaginary, and γ is the loss factor.

The model described in (3.20) provides valid responses at low frequencies and in the vicinity of the resonance frequency. However, in the limit as $\omega \to \infty$, $\chi_m \to -K$, which contradicts the expected physical behavior of χ_m. At extremely high frequencies, because of the electron's inertia, the materials cannot be magnetized, implying $\chi_m \to 0$, and hence, the model breaks down [10].

From (3.20) and (3.35), the equivalence between (3.20) and (3.29) is established through

$$F = K \tag{3.21}$$

$$P = \frac{\gamma K^2}{\sqrt{\omega\omega_0}} \tag{3.22}$$

$$\chi_m\left(\Omega; F, P\right) = \frac{F\Omega^2}{1 - \Omega^2 + jPF^{-2}\sqrt{\Omega^3}} \tag{3.23}$$

where

$$\Omega = \omega/\omega_0, \tag{3.24}$$

and F is the fractional area of the cell occupied by the interior of the inclusion, ranging from 0 to 1, given by:

$$F = \frac{s}{\delta x \ \delta z} = \frac{s}{A} \tag{3.25}$$

and P is defined as:

$$P = \frac{1}{A^2} \frac{{\omega'_0}^4}{\sqrt{{\omega_0}^5 {\omega''_0}^3}} \tag{3.26}$$

P depends on the resonance frequency ω_0, as well as the physical properties of the design such as the permittivity of the host substrate, ϵ_r, width of the metal strips, b, and space between the strips, g, (in edge-coupled inclusions) or gap, g, between parallel contours in a unit cell (in broadside-coupled inclusion) and the resistance. By factoring the frequency-related parts, the physical parameter P can be expressed as:

$$P = \mathcal{K} \ \omega_0^{-\frac{5}{2}} \tag{3.27}$$

where $\mathcal{K} \equiv \mathcal{K}(A, b, g, t, \sigma, \epsilon_r, \mu_r)$ is related only to the physical parameters (conductivity of inclusion, width and height of route of an inclusion, and permittivity of host medium), and is expressed as:

$$\mathcal{K} = \frac{R_0}{A^2 L_0^2 C_0} = \frac{n'(\delta y)^2}{n^4 (\delta x)^2 (\delta z)^2 b \sqrt{2\mu_0^3 \sigma} C_0\left(\epsilon_r, g, b, t\right)} \tag{3.28}$$

Note that since γ has a linear dependence on $\sqrt{\omega}$ [49], and F and P are *completely* independent of the operational frequency, the introduced model formulation is advantageous in forthcoming applications presented in the following chapters.

Note that P is expressed as the multiplication of a frequency-invariant coefficient, $\mathcal{K}$ and a simple function of the resonance frequency which is typically specified in a given design problem.

The relation in (3.23) can be expressed in terms of the susceptibility of the lossless case χ_{m0} as:

$$\chi_m\left(\Omega; F, P\right) = \frac{F\Omega^2}{1-\Omega^2}\left\{\frac{1}{1+j\frac{P\Omega\sqrt{\Omega}}{F^2(1-\Omega^2)}}\right\} = \chi_{m0}\left(1+j\sqrt{\xi(\Omega)}\right)^{-1} \tag{3.29}$$

where χ_{m0} is

$$\chi_{m0} = \frac{F\Omega^2}{1-\Omega^2}, \tag{3.30}$$

and $\xi\left(\Omega\right)$ is defined as:

$$\xi\left(\Omega\right) = \frac{P^2\Omega^3}{F^4(1-\Omega^2)^2} = \alpha^2\frac{\Omega^3}{\left(1-\Omega^2\right)^2} \tag{3.31}$$

and $\alpha = P/F^2$.

The factor α determines the level of loss in the medium. The factor is referred to as the *dissipation factor*. Since frequencies below the resonance frequency result in permeability higher than one, the frequency range $0 < \Omega < 1$ is considered to be the only frequency range of relevance when designing artificial magnetic permeability that achieves enhanced positive permeability.

The real part of (3.23) is considered as the resultant magnetic susceptibility of the medium. The real part of the magnetic susceptibility is given by:

$$\chi_{mRe}\left(\Omega; F, P\right) = \mathcal{R}e\left(\chi_m\left(\Omega; F, P\right)\right) = \frac{F^5\Omega^2\left(1-\Omega^2\right)}{F^4\left(1-\Omega^2\right)^2 + P^2\Omega^3} \tag{3.32}$$

and it can also be stated in the following form:

$$\chi_{mRe}\left(\Omega; F, P\right) = \frac{F\Omega^2}{1-\Omega^2}\left\{\frac{1}{1+\frac{P^2\Omega^3}{F^4(1-\Omega^2)^2}}\right\} = \chi_{m0}\left(1+\xi(\Omega)\right)^{-1} \tag{3.33}$$

22

The aforementioned closed form for the susceptibility function is an appropriate form which is used in chapter 4 to derive some fundamental limitations and in chapter 5 for developing the design methodology of AMMs.

$\chi_{m0}(\Omega)$, the magnetic susceptibility of lossless medium, and $\xi(\Omega)$, the loss factor, can be written in the following form:

$$\chi_{m0}(\Omega) = F \cdot f_1(\Omega) \tag{3.34}$$

$$\xi(\Omega) = \frac{P^2}{F^4} \cdot f_2(\Omega) \tag{3.35}$$

where

$$f_2(\Omega) = \frac{f_1^2(\Omega)}{\Omega} = \frac{\Omega^3}{(1 - \Omega^2)^2} \tag{3.36}$$

where $f_1(.)$ and $f_2(.)$ are only a function of Ω. This is a significant point which is used for developing a design methodology.

Using (3.29), the permeability can be written as:

$$\mu(\Omega; F, P) = 1 + \chi_m(\Omega; F, P) = 1 + \chi_0(\Omega)(1 + j\sqrt{\xi(\Omega)})^{-1} \tag{3.37}$$

Two significant parameters of an AMM are the real effective permeability and the magnetic loss tangent (MLT), expressed respectively as:

$$\mu_{Re}(\Omega) = 1 + \chi_0(\Omega)(1 + \xi(\Omega))^{-1} \tag{3.38}$$

$$\tan\delta(\Omega) = -\frac{\mu_{Im}(\Omega)}{\mu_{Re}(\Omega)} = \chi_0(\Omega)\sqrt{\xi(\Omega)}\,(1 + \chi_0(\Omega) + \xi(\Omega))^{-1} \tag{3.39}$$

Fig.3.4 shows the real and imaginary part of the effective magnetic susceptibility function for a typical AMM introduced by the presented model.

In subsequent chapters, the aforementioned equations are exploited to deriving fundamental limitation of the magnetic behavior of AMMs and methodically design AMMs meeting specific operational requirements.
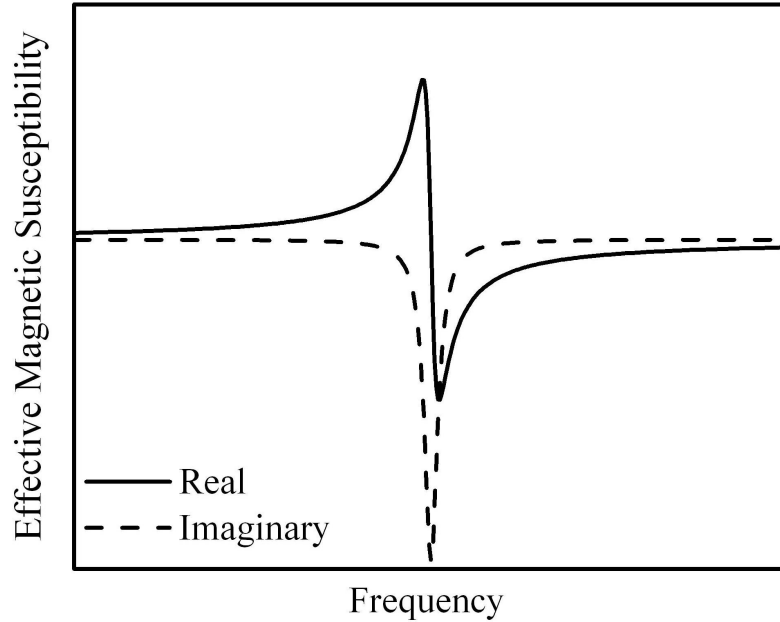
Figure 3.4: A typical response of an artificial magnetic material. The graph shows the magnetic susceptibility as a function of frequency. Note no specific frequency scale depicted.

3.2 Contribution

I derived generalized expressions for the magnetic permeability and susceptibility governing the behavior of composite engineered magnetic materials with any arbitrary shape of an inclusion. To generalize the expression for use in any frequency range, it is expressed in terms of the normalized angular frequency Ω. Therefore, for any structure, calculations of P and F are sufficient to obtain the effective magnetic behavior.

The advantage of the formula in (3.29) is that the topological properties of the inclusion's contour such as surface area and perimeter of the inclusions and the physical properties of the design appear *explicitly* in the formula as two factors. In fact, the strongest feature of the model is that inclusions with different topologies but having identical perimeter and area, result in the same values for the magnetic susceptibility and permeability.

Chapter 4

Limitations

Artificial magnetic materials are designed to provide enhanced positive permeability over a specific range of frequencies. For most applications, it is desirable to have a uniform permeability over the range of frequencies of interest, however, due to the resonating nature of inclusions, the permeability resulting from engineered magnetic materials changes rapidly with frequency [1], [2]. The variation with frequency will result in dispersion leading to limited if not poor performance in many applications related to antenna miniaturization and gain enhancement [50]. In this chapter, it is firstly shown that dispersion and loss are connected through Kramers-Kronig relations. Then, the fundamental limitations on frequency dispersion reduction in the design of artificial magnetic materials are investigated for the lossless case where the conductivity of the conductor is assumed infinite (the first section) and for the case where Ohmic losses are presented (the second section). It is shown that the dispersion in an AMM is limited by the desired operational bandwidth. Moreover, in the last sections, employing the formulation has been developed in the previous chapter, a set of constraints is derived. The constraints are shown the effect of the newly introduced parameters on the effective permeability of the medium and the magnetic loss tangent.

4.1 Kramers-Kronig Relations

In essence, the Kramers-Kronig relations describe the fundamental connection between the real and imaginary parts of a holomorphic function, and it is often used to constitute the causality constraints on theoretical formulation of physical systems [64]-[67]. Consider a complex analytic function $A(\omega) = A_{\text{Re}}(\omega) + jA_{\text{Im}}(\omega)$, where $A(\omega) \to 0$ faster than $\frac{1}{\omega}$ as $|\omega| \to \infty$. The Kramers-Kronig equation can be written as [68], [69]:

$$A_{\text{Re}}(\omega) = \frac{1}{\pi}\mathcal{P}\int_{-\infty}^{\infty}\frac{A_{\text{Im}}(\xi)}{\xi - \omega}d\xi \tag{4.1}$$

$$A_{\text{Im}}(\omega) = -\frac{1}{\pi}\mathcal{P}\int_{-\infty}^{\infty}\frac{A_{\text{Re}}(\xi)}{\xi - \omega}d\xi \tag{4.2}$$

where $\mathcal{P}$ denotes the Chauchy principal value. The relations show that real and imaginary part of such a response are not independent functions. By knowing a single part of a function, either real or imaginary part, over a continuous region on the frequency spectrum, the other part is determined. The analyticity of $\epsilon_{\text{eff}}(\omega)$ and $\mu_{\text{eff}}(\omega)$ in the upper half-ω-plane allows immediately the use of the Kramers-Kronig relations. Also, it can be shown that from the symmetry property of $\epsilon_{\text{eff}}(\omega)$ and $\mu_{\text{eff}}(\omega)$, $\epsilon_{\text{Re}}(\omega)$ and $\mu_{\text{Re}}(\omega)$ is even, and $\epsilon_{\text{Im}}(\omega)$ and $\mu_{\text{Im}}(\omega)$ is odd [11]. Thus, the Kramers-Kronig relations can be transformed to span positive frequencies as for $\epsilon_{\text{eff}}(\omega)$:

$$\epsilon_{\text{Re}}(\omega) = 1 + \frac{2}{\pi}\mathcal{P}\int_{0}^{\infty}\frac{\omega'\epsilon_{\text{Im}}(\omega')}{\omega'^2 - \omega^2}d\omega' \tag{4.3}$$

$$\epsilon_{\text{Im}}(\omega) = -\frac{2\omega}{\pi}\mathcal{P}\int_{0}^{\infty}\frac{\omega'\epsilon_{\text{Re}}(\omega') - 1}{\omega'^2 - \omega^2}d\omega' \tag{4.4}$$

and for $\mu_{\text{eff}}(\omega)$:

$$\mu_{\text{Re}}(\omega) = 1 + \frac{2}{\pi}\mathcal{P}\int_{0}^{\infty}\frac{\omega'\mu_{\text{Im}}(\omega')}{\omega'^2 - \omega^2}d\omega' \tag{4.5}$$

$$\mu_{\text{Im}}(\omega) = -\frac{2\omega}{\pi}\mathcal{P}\int_{0}^{\infty}\frac{\omega'\mu_{\text{Re}}(\omega') - 1}{\omega'^2 - \omega^2}d\omega' \tag{4.6}$$

These relations are very general mathematically, and somehow limited practically, as the physical responses are not known over the whole spectrum. Expanding $\mu_{\text{Im}}(\omega)$

from a very narrow absorption band at $\omega = \omega_0$, the integrals in (4.5) can be expanded, and $\mu_{\text{eff}}(\omega)$ stated as:

$$\mu_{\text{eff}}(\omega) = \left(\tilde{\mu} + \frac{k}{\omega_0^2 - \omega^2} + ... \right) + i \left(\frac{\pi k}{2\omega_0} \delta(\omega - \omega_0) + ... \right) \tag{4.7}$$

where k is a constant, and $\tilde{\mu}$ represents a slowly varying function.

4.2 Dispersion Limitation

A typical response of an artificial magnetic medium is shown in Fig. 3.4. This magnetic response is generic, and widely accepted in the literature [1], [12].

4.2.1 Lossless Case

By assuming zero resistance in the metallic inclusions, the resultant susceptibility of the lossless case, χ_{m0} from (3.30) and (3.24) will be a real number and is equal to:

$$\chi_{m0}(\omega) = \frac{\left(\frac{\omega}{\omega_0} \right)^2 F}{1 - \left(\frac{\omega}{\omega_0} \right)^2} \tag{4.8}$$

Assuming ω_1 and ω_2 as the lowest and highest operational frequencies ($\omega_1 < \omega_2$), and μ_1, μ_2 as the resultant permeability at these frequencies respectively, I am seeking a general relationship between, $\delta\mu = \mu_2 - \mu_1$, and, $BW = \omega_2 - \omega_1$. (Since the engineered magnetic materials are designed to provide permeability higher than one, the frequencies ω_1 and ω_2, are chosen to be less than the resonance frequency ω_0.)

Enforcing (4.8) at ω_1 and ω_2, we have:

$$\begin{cases} \chi_1 = \dfrac{F\left(\frac{\omega_1}{\omega_0} \right)^2}{1 - \left(\frac{\omega_1}{\omega_0} \right)^2} \\[4mm] \chi_2 = \dfrac{F\left(\frac{\omega_2}{\omega_0} \right)^2}{1 - \left(\frac{\omega_2}{\omega_0} \right)^2} \end{cases} \tag{4.9}$$

Solving the system of equations (4.9) for F yields:

27

$$F = \frac{\left(\omega_2{}^2 - \omega_1{}^2\right)\left(\chi_2 \chi_1\right)}{\chi_2 \omega_1{}^2 - \chi_1 \omega_2{}^2} \tag{4.10}$$

Recall that since F is the fractional area occupied by the interior of the inclusion in the unit cell, F is bound by unity. Satisfying the conditions of $0 < F < 1$ leads to restrictions on the susceptibilities at two selected frequencies. For the first condition $F > 0$, it is clear that the permeability is larger than one and therefore the susceptibility is positive for all frequencies less than ω_0, (i.e., $\mu_2, \mu_1 > 1$ and $\chi_2, \chi_1 > 0$). Consequently, since $\omega_2 > \omega_1$, we have:

$$\left(\frac{\omega_2}{\omega_1}\right)^2 \leq \frac{\chi_2}{\chi_1} \tag{4.11}$$

The above equation shows an interesting constraint which limits the ratio of the susceptibility at any two arbitrary frequencies to the square of the ratio of those frequencies. Another interesting observation is that the relationship given in (4.11) is independent of both physical and geometrical characteristics of the designed inclusion. Any effort to improve the frequency bandwidth of the resultant permeability is strictly confined to this limitation. As an example, suppose $\omega_2 = 3\omega_1$, then χ_2/χ_1 cannot be less than 9.

For the second condition, namely, $F < 1$, I consider (4.10) and after some algebraic manipulations, we have:

$$\left(\frac{\omega_2}{\omega_1}\right)^2 \leq \left(\frac{\chi_2}{\chi_1}\right)\left(\frac{\chi_1 + 1}{\chi_2 + 1}\right) \tag{4.12}$$

or equivalently:

$$\left(\frac{\omega_2}{\omega_1}\right)^2 \leq \left(\frac{\chi_2}{\chi_1}\right)\left(\frac{\mu_1}{\mu_2}\right) \tag{4.13}$$

Since the ratio of $(\chi_1 + 1)/(\chi_2 + 1)$ is always less than one, the limit achieved in (4.13) is even stronger than that of (4.11). Therefore, the change of susceptibility with frequency is even more rapid than the square of frequency.

By defining mean permeability μ_c and central frequency ω_c, respectively, as:

$$\begin{cases} \mu_c = \frac{1}{2}\left(\mu_2 + \mu_1\right) \\[2ex] \omega_c = \frac{1}{2}\left(\omega_2 + \omega_1\right) \end{cases} \tag{4.14}$$

and $\delta\chi$ and $\delta\mu$ as the deviation of susceptibility and permeability, respectively, 4.13) can be rewritten as:

$$\left(\frac{\chi_c + \frac{\delta\chi}{2}}{\chi_c - \frac{\delta\chi}{2}}\right)\left(\frac{\mu_c - \frac{\delta\mu}{2}}{\mu_c + \frac{\delta\mu}{2}}\right) \geq \left(\frac{\omega_c + \frac{BW}{2}}{\omega_c - \frac{BW}{2}}\right)^2 \tag{4.15}$$

In many application $BW \ll \omega_c$ and $\delta\mu \ll \mu_c$. Using these conditions, (4.15) can be simplified using first-order binomial expansions as:

$$\left(\frac{\omega_2}{\omega_1}\right)^2 = \left(\frac{\omega_c + \frac{BW}{2}}{\omega_c - \frac{BW}{2}}\right)^2 \cong 1 + \frac{2BW}{\omega_c} \tag{4.16}$$

$$\begin{aligned} \left(\frac{\chi_2}{\chi_1}\right)\left(\frac{\mu_1}{\mu_2}\right) &= \left(\frac{\chi_c + \frac{\delta\chi}{2}}{\chi_c - \frac{\delta\chi}{2}}\right)\left(\frac{\mu_c - \frac{\delta\mu}{2}}{\mu_c + \frac{\delta\mu}{2}}\right) \\ &\cong \left(1 + \frac{\delta\chi}{\chi_c}\right)\left(1 - \frac{\delta\mu}{\mu_c}\right) \\ &\cong 1 + \delta\mu\left(\frac{1}{\chi_c} - \frac{1}{\mu_c}\right) = 1 + \frac{\delta\mu}{\chi_c\mu_c} \end{aligned} \tag{4.17}$$

Substituting (4.16) and (4.17) in (4.13) results in:

$$\frac{BW}{\omega_c} \leq \frac{1}{2\chi_c}\left(\frac{\delta\mu}{\mu_c}\right) \tag{4.18}$$

The condition in (4.18) relates the deviation in the relative permeability to the relative bandwidth. Since the bandwidth BW is inversely proportional to the mean permeability μ_c, there is a tradeoff between maximizing the effective permeability and broadening the frequency range in which the smooth deviation of permeability is obtainable. In fact, for two different designs with the same relative permeability deviation, wider bandwidth can be achieved in the design with lower permeability.
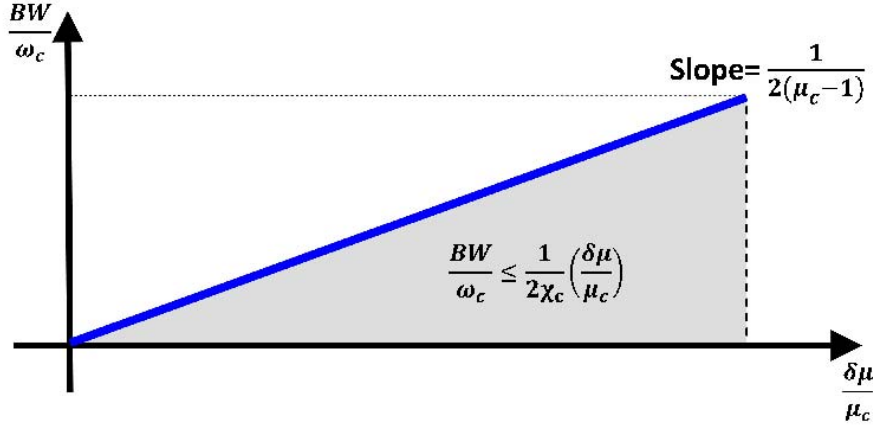
Figure 4.1: The relative frequency bandwidth is depicted versus the relative permeability deviation. The grey area determines the possible interval for the bandwidth. Notice that the slope is inversely proportional to the central susceptibility.

Fig. 4.1 illustrates (4.18) graphically. For any design, the resultant bandwidth lies in the gray area shown in Fig. 4.1. As an example, for μ_c equal to 5, requiring the relative permeability deviation to be less than 1 percent bounds the relative frequency bandwidth to 0.125%, and say, for a central frequency of $200MHz$ the bandwidths would theoretically be less than $250kHz$. As a second example, if $\mu_c = 2$, having 1% deviation in the permeability leads to a maximum of 0.5% relative bandwidth.

Although first-order terms were used in the Taylor's expansion in (4.18), it can be shown that making the approximation more accurate by including second-order terms in the expansion gives identical conclusions.

4.2.2 Lossy Case

By considering loss, the resultant permeability in (3.37) or the resultant suscepti- bility in (3.29) will have real and imaginary parts. Since only the real part affects the permeability in the artificial magnetic medium and the imaginary part appears only when introducing loss in the medium, the deviation with frequency is mostly important for the real part. In this section, the frequency deviation of the real part

will only be discussed.

As shown in previous chapter, the resultant permeability can be modeled as the response of an RLC circuit. It is expected that adding resistance or loss to the system (inclusions) leads to a smoother frequency response. Therefore, it is expected that the fundamental limits achieved for the frequency response of the permeability for the lossless case to be sufficient for the lossy case. Note that in the context of this work, the attention is only on the positive range of Ω (i.e., $0 < \Omega < 1$).

The function $\xi(\Omega)$ (Eq.3.31) has a second-order simple singularity at the normalized resonance frequency (i.e. $\Omega = 1$), thus $\xi(\Omega)$ approaches infinity as Ω approaches one. The factor α in (3.31) is a parameter that scales the magnitude of $\xi(\Omega)$ and all its derivatives. Differentiation of $\xi(\Omega)$ with respect to Ω gives:

$$\frac{d\xi(\Omega)}{d\Omega} = \alpha^2 \frac{\Omega^2 (3 + \Omega^2)}{(1 - \Omega^2)^3} = \left(\Omega + \frac{3}{\Omega}\right) \xi(\Omega) \qquad (4.19)$$

In the range $0 < \Omega < 1$, (4.19) is always positive, therefore, the function increases monotonically with respect to Ω. So, for $\Omega_2 > \Omega_1$, we have:

$$\xi(\Omega_2) \geq \xi(\Omega_1) \qquad (4.20)$$

Using (4.19), equation (3.32) leads to:

$$\frac{\chi_{m0}(\Omega_1) - \chi_{mRe}(\Omega_1)}{\chi_{mRe}(\Omega_1)} \leq \frac{\chi_{m0}(\Omega_2) - \chi_{mRe}(\Omega_2)}{\chi_{mRe}(\Omega_2)} \qquad (4.21)$$

Simplification of (4.21) results in:

$$\frac{\chi_{mRe}(\Omega_2)}{\chi_{mRe}(\Omega_1)} \leq \frac{\chi_{m0}(\Omega_2)}{\chi_{m0}(\Omega_1)} \qquad (4.22)$$

The inequality in (4.23) states that the ratio of the magnetic susceptibility at two different frequencies for the lossless case is larger than that of the lossy case. This indicates that the magnetic susceptibility function is flatter for the lossy case than for the lossless case. Note that the limit achieved in equation (4.18) is independent of the topology of the inclusion.

4.3 Physical and Geometrical Effects on Dispersion and Loss

As shown in Chapter 3, all physical properties are summarized in one parameter, P, and all geometrical properties are summarized in one parameter F. Equation (3.29) and Equation (3.37) give the magnetic susceptibility and consequently the permeability in terms of these two parameters, P and F. Therefore, the study of the effect of physical and geometrical parameters on the resultant permeability and its frequency domain behavior will be confined to F and P.

4.3.1 Effects on Real Effective Permeability

Differentiation of (3.38) with respect to F while using (3.31) gives:

$$
\begin{aligned}
\frac{\partial \mu_{Re}\left(\Omega; F\right)}{\partial F} &= \frac{\partial \chi_{Re}\left(\Omega; F\right)}{\partial F} = \frac{1}{1+\xi}\frac{\partial \chi_{m0}}{\partial F} - \frac{1}{(1+\xi)^2}\frac{\partial \xi}{\partial F} \\
&= \frac{\Omega^2\left(1-\Omega^2\right)\left(\left(1-\Omega^2\right)^2 + 5P^2\ F^{-4}\Omega^3\right)}{\left(\left(1-\Omega^2\right)^2 + P^2\Omega^3\ F^{-4}\right)^2} \\
&= \frac{\Omega^2}{1-\Omega^2}\left(\frac{1+5\xi(\Omega)}{1+\xi(\Omega)}\right)
\end{aligned}
\tag{4.23}
$$

In the frequency range of interest, $0 < \Omega < 1$, we have:

$$
\frac{\partial \mu_{Re}\left(\Omega; F\right)}{\partial F} > 0
\tag{4.24}
$$

Therefore, the larger F, the higher the permeability. Since F is defined as the ratio of the surface enclosed by the inclusion to the total surface of the unit cell, the contours which provide higher enclosed surface lead to higher permeability. On the other hand, the surface of the inclusion and its length are related to each other through the resonance frequency in (3.18). Indeed, they are inversely proportional at a fixed resonance frequency. Therefore, for all inclusions designed to operate at the same resonance frequencies, the ones that provide larger enclosed surface (or larger F) and shorter total length (i.e., perimeter) will result in higher value for permeability.
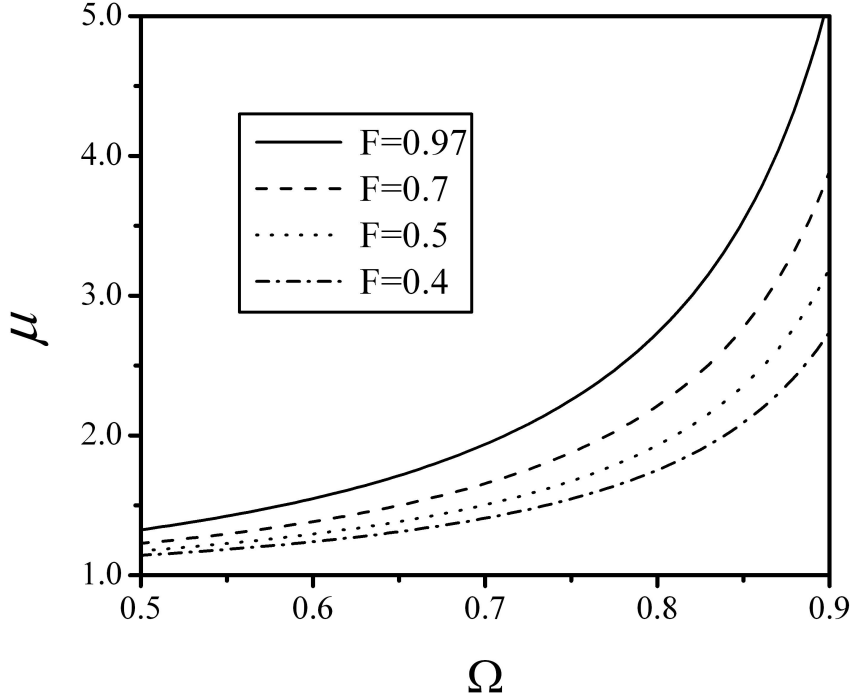
Figure 4.2: Real part of the permeability as a function of the normalized frequency, Ω, for different values of F. The inclusion trace is made of copper and the dimensions are $g = b = 0.127mm$, $\varepsilon_r = 3.38$, $\delta y = 3.028mm$, $\delta x = \delta z = 20mm$.

Fig. 4.2 shows the real part of the permeability as a function of Ω for different values of F. Furthermore, Fig. 4.2 shows that an increase in F leads to a larger value of the permeability which is expected from (4.24).

In (3.38), $\xi(\Omega)$ is a function of P. Taking the derivative of (3.38) with respect to P gives:

$$
\begin{aligned}
\frac{\partial \mu_{Re}(\Omega, P)}{\partial P} &= \frac{\partial \chi_{m Re}(\Omega, P)}{\partial P} = \frac{1}{1+\xi}\frac{\partial \chi_{m0}}{\partial F} - \frac{1}{(1+\xi)^2}\frac{\partial \xi}{\partial F} \\
&= -\frac{2}{P}\frac{F\Omega^2}{1-\Omega^2}\frac{\xi(\Omega)}{(1+\xi(\Omega))^2} = -\frac{2}{P}\frac{\xi(\Omega)}{1+\xi(\Omega)}\chi_{m Re}(\Omega; F)
\end{aligned}
\tag{4.25}
$$

Notice that (4.25) is always negative for $0 < \Omega < 1$. Therefore, by increasing P, one can expect the permeability to decrease. However, what is interesting is that for

33
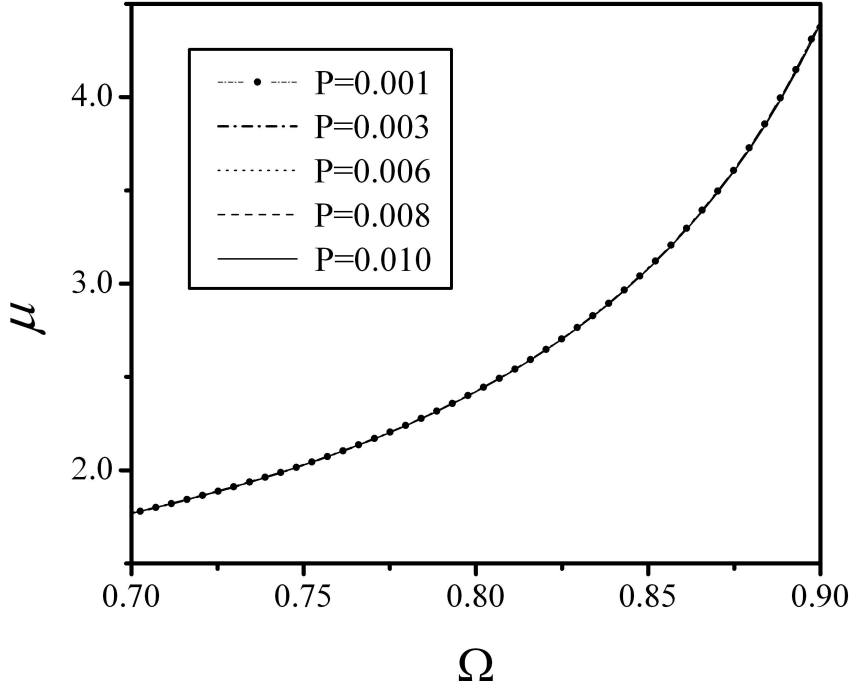
Figure 4.3: The real part of permeability for different values of P, the geometrical parameter F is assumed to be 0.8. Notice that all curves are almost overlapping.

practical considerations, μ is highly insensitive to changes in P. Fig. 4.3 shows a plot of μ vs. Ω, for the case of $F = 0.8$ (this case was simply selected as an example). one can observe that as P changes by one order of magnitude, the resultant permeability remains practically constant. Notice that the curves in Fig. 4.3 are indistinguishable. This is due to the fact that in (3.38), the only part that is a function of P is $\xi(\Omega)$ which is much smaller than 1. (Since $\alpha = P/F^2$, and from (3.29), it can be shown that for practical geometries such as those considered in Table 1, $\xi(\Omega) << 1$. Notice that I am assuming that the upper frequency of interest is not close to the resonance frequency. As the resonance frequency is approached, the function $\xi(\Omega)$ starts to diverge and is no longer much smaller than one.)

Table 4.1 shows three P values for designs proposed earlier in the literature. In all cases, the P factor was small, even in some cases smaller than the numbers I considered for the graph in Fig. 4.3.

Table 4.1: Parameters of Some Previously Designed Inclusions

Design	$A(mm^2)$	$\mathcal{K}$	$\omega_0(GHz)$	P	F
Solenoid [2]	110	2.3×10^{19}	0.998	9.8×10^{-6}	0.11
SRR [1]	100	9.0×10^{21}	32.58	4.9×10^{-4}	0.53
Hilbert-SRR [37]	400	7.5×10^{19}	0.981	2.4×10^{-2}	0.42

4.3.2   Effects on Magnetic Loss Tangent

An important parameter in designing artificial magnetic materials is the *Magnetic Loss Tangent* , $\tan \delta$, which represents the magnetic loss in the medium[1]. In most applications, it is desirable to have $\tan \delta$ as small as possible. In this section, the behavior of $\tan \delta$ with respect to the geometrical and physical parameters, F and P, is investigated.

The magnetic loss tangent is defined as:

$$\tan \delta = -\frac{\mathcal{I}m\left(\mu\left(\omega\right)\right)}{\mathcal{R}e\left(\mu\left(\omega\right)\right)} \tag{4.26}$$

Recall from (3.39), and using (3.30) $\tan \delta$ can be rewritten as:

$$\tan \delta \ = \frac{F\Omega^2\sqrt{\xi\left(\Omega\right)}}{\left(1+\xi(\Omega)\right)\left(1-\Omega^2\right)+F\Omega^2} \tag{4.27}$$

Differentiating (4.27) with respect to F, we obtain:

$$\frac{\partial(\tan \delta)}{\partial F} = -\frac{\Omega^2\left(1-\Omega^2\right)\left(1-3\xi\left(\Omega\right)\right)\sqrt{\xi\left(\Omega\right)}}{\left(\left(1+\xi(\Omega)\right)\left(1-\Omega^2\right)+F\Omega^2\right)^2} \tag{4.28}$$

In (4.28), all terms except $(1-3\xi(\Omega))$, are positive for all values of F and Ω. Since $\xi(\Omega)$ is inversely related to F (see Eq.(3.29)), $\tan \delta$ has a local maximum at a specific value of F denoted as F_{max}. In Fig. 4.4, $\tan \delta$ is plotted as a function of F for different values of P and Ω. Notice that, F_{max}, the value of F corresponding to

---

[1]Note that the physical loss in the medium is described by the imaginary part of the refractive index, extinction factor, the relation between the extinction factor and magnetic tangent is derived. Please see Appendix [A].
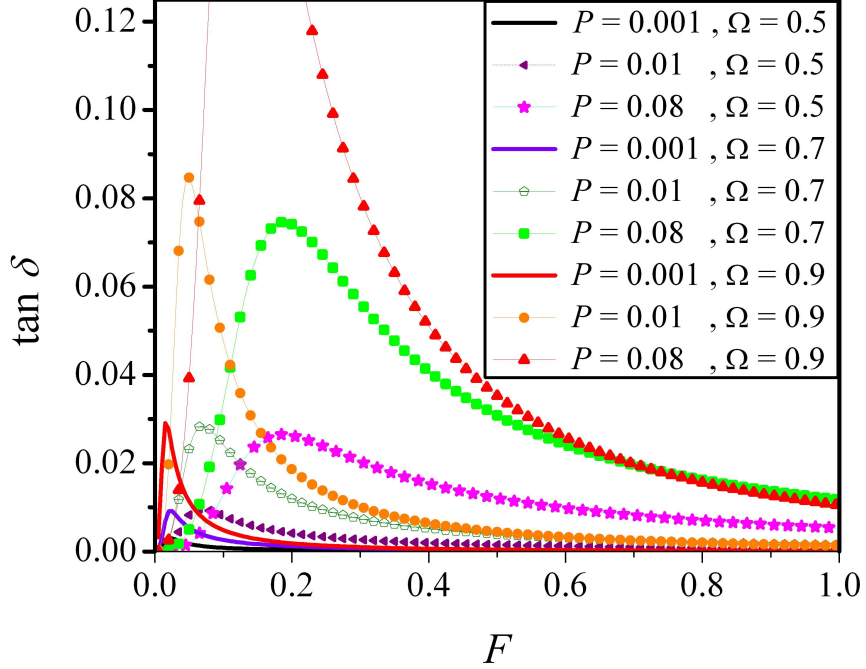
Figure 4.4: The magnetic loss tangent, $\tan\delta$, as a function of the geometrical parameter, F, for different values of P and Ω.

maximum $\tan\delta$, is relatively small compared to unity, meaning that $\tan\delta$ reaches a maximum when the area of the inclusions is small in comparison to the area of the unit cell. Since the permeability approaches unity for small values of F, it is most desirable to achieve the highest permeability, hence, F is chosen to be greater than F_{max}.

For designs with F larger than F_{max}, as shown in Fig. 4.4, increasing F leads to a smaller value of $\tan\delta$. Consequently, an optimal design is a design with inclusions whose area is close to the unit cell's area $(F \rightarrow 1)$ which leads to a lower magnetic loss. Hence, the minimum value of $\tan\delta$, achieved at $F = 1$, is:

$$\min(\tan\delta) = \left. \tan\delta \right|_{\mathrm{F}=1} \cong \Omega^2\sqrt{\xi(\Omega)} = \frac{\sqrt{\Omega^7}}{1-\Omega^2}P \qquad (4.29)$$

Fig. 4.5 shows a three dimensional presentation of $\tan\delta$ as a function of F and Ω. As shown in this figure, the maximum value of $\tan\delta$ occurs at the lower value of F.
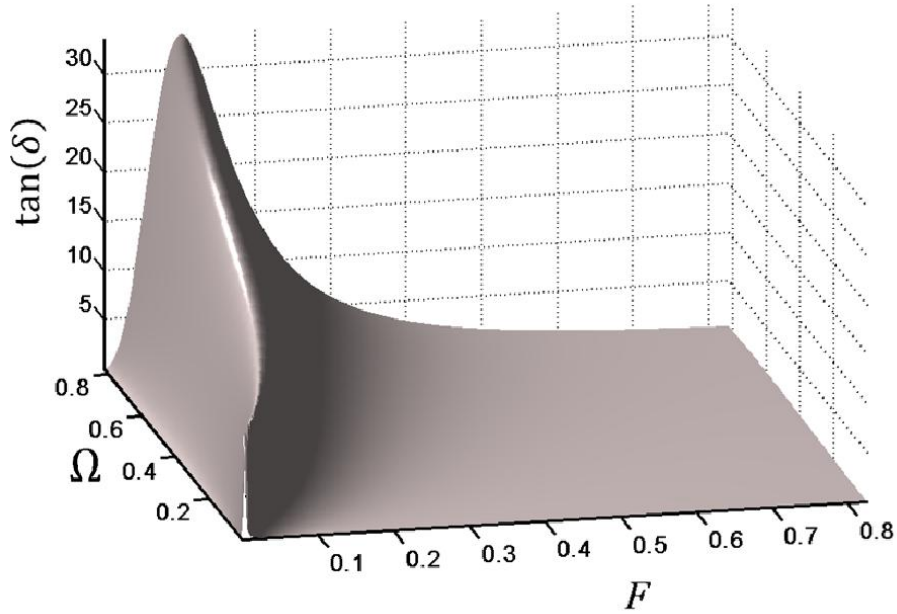
Figure 4.5: The magnetic loss tangent, $\tan\delta$, as a function of Ω and F, for $P=0.05$

For instance, for an inclusion with a physical factor P less than 0.002, the maximum of $\tan\delta$ at any frequency occurs at F less than 0.2. Moreover, as F increases, i.e., the inclusion occupies more area of the unit cell, the maximum moves to larger Ω and also becomes larger (from about 10 when Ω and F are close to zero, and more than 35 when Ω is 0.8 and F is 0.1). In addition, it can be observed that as F approaches unity $\tan\delta$ decreases.

To study the effect of physical parameters on loss, one needs to consider the derivative of $\tan\delta$ with respect to P:

$$\frac{\partial(\tan\delta\ )}{\partial P} = \frac{F\Omega^2\sqrt{\xi(\Omega)}\left((1-\xi(\Omega))\left(1-\Omega^2\right)+F\Omega^2\right)}{P((1+\xi(\Omega))\left(1-\Omega^2\right)+F\Omega^2)^2} \qquad (4.30)$$

For a specific value of P, denoted as P_{max}, the term $(1-\xi(\Omega)\left(1-\Omega^2\right)+F\Omega^2)$ vanishes, and $\tan\delta$ reaches a maximum for a certain value of F and Ω. (It is a simple exercise to show that $\tan\delta$ has only one maximum within the range of P. In Fig. 4.6, $\tan\delta$ is plotted as a function of P for different values of F and Ω. As shown in Fig. 4.6, the maximum of $\tan\delta$ function occurs for values of P much higher than
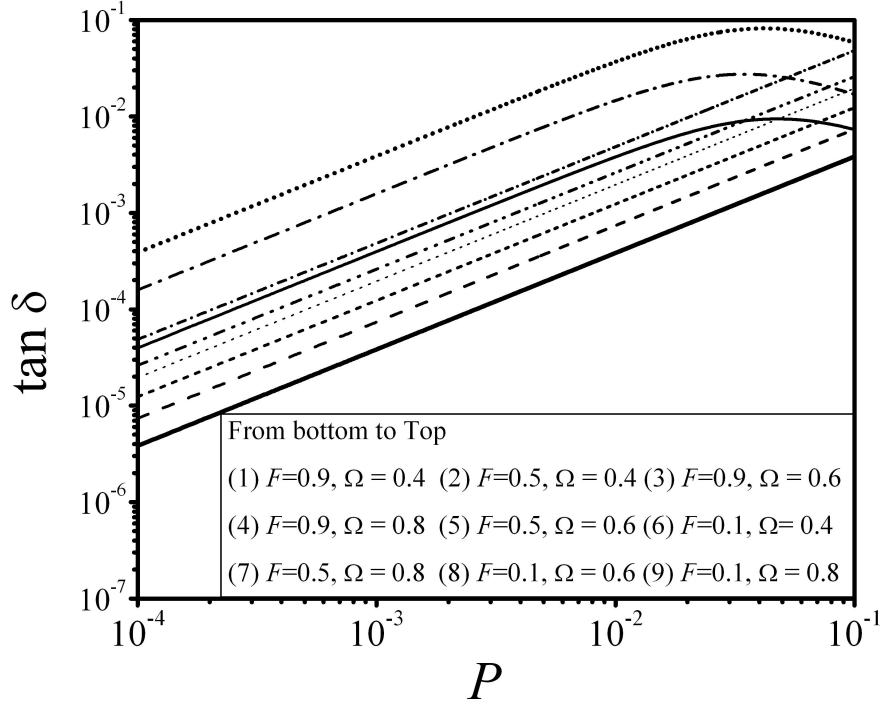
Figure 4.6: The magnetic loss tangent $\tan\delta$ as a function of the physical parameter, P for different values of F and Ω.

those used in practical structures.

4.4   The Permeability Maximum Value

In this section, the normalized frequency in which the permeability function maximizes is calculated. The normalized frequency is calculated in terms of the geometrical and physical parameters. Correspondingly, a relationship for the maximum of the permeability function is derived.

Recall from (3.33), the real part of the magnetic susceptibility can be written as

$$\chi_{mRe}(\Omega) = \chi_0(\Omega)(1 + \xi(\Omega))^{-1} \tag{4.31}$$

By limiting Ω to 0 and 1, we have:

$$\begin{cases} \lim_{\Omega \to 0} \chi_{mRe}(\Omega) = 0 \\ \lim_{\Omega \to 1} \chi_{mRe}(\Omega) = 0 \end{cases} \qquad (4.32)$$

Therefore, because $\chi_{mRe}(\Omega)$ is a positive function over the range of $\Omega \in [0,1]$, it is maximized at $\Omega_{\max} \in (0,1)$ which is the root of the first derivative of $\chi_{mRe}(\Omega)$ over an interval $(0,1)$. Taking the derivative of $\chi_{mRe}(\Omega)$ with respect to Ω,

$$\frac{1}{\chi_0} \frac{d\chi_0}{d\Omega} = \frac{1}{(1+\xi)} \frac{d\xi}{d\Omega} \qquad (4.33)$$

By substituting from (3.34), (3.35) and (3.36) in (4.33), we have

$$\mathcal{B}^2 \cdot \Omega^3 (1 + \Omega^2) - (1 - \Omega^2)^2 = 0 \qquad (4.34)$$

where $\mathcal{B} = \frac{P}{F^2}$.

It is clear that the root of (4.34) and equivalently the maximum of χ_{mRe} approaches one if and only if $P \to 0$. In previous chapter, Table.4.1, it has been shown that for practical applications, $\frac{P^2}{F^4} \ll 1$. Hence, one can assume $\Omega_{\max} = 1 - \alpha$ where $\alpha \ll 1$. Substituting $\Omega = 1 - \alpha$ in (4.34) and considering up to the second order of expansion, It is obtained:

$$(8 - 13\mathcal{B}^2)\alpha^2 + 8\mathcal{B}^2\alpha - 2\mathcal{B}^2 = 0 \qquad (4.35)$$

By solving (4.35) for α, $\Omega_{\max}$ is obtained as

$$\Omega_{\max} = 1 - \frac{1}{2}\mathcal{B} + \frac{1}{2}\mathcal{B}^2 + \mathcal{O}(\mathcal{B}^3) \qquad (4.36)$$

and accordingly

$$\mathcal{M}ax(\chi_{mRe}) \simeq \frac{F}{2\mathcal{B}} - \frac{F}{8} + \frac{3F}{64}\mathcal{B} - \frac{43F}{256}\mathcal{B}^2 + \mathcal{O}(\mathcal{B}^3) \qquad (4.37)$$

For the maximum value of $F = 1$ and $\mathcal{B} = 0.1$ the error in the calculation of the maximum value of the magnetic susceptibility is less than 0.1%. In fact, even by taking only the first two terms in (4.36) and (4.37), the error remains less than 0.1%. After substituting $\mathcal{B} = \frac{P}{F^2}$, and considering the first two term in (4.36) and (4.37), the

frequency in which the permeability maximizes and the maximum of permeability is approximately derived:

$$
\begin{cases}
\Omega_{\max} \simeq 1 - \frac{1}{2}\frac{P}{F^2} \\
\mathcal{M}ax\left(\chi_{mRe}\right) \simeq -\frac{F}{8} + \frac{F^3}{2P}
\end{cases}
\tag{4.38}
$$

Equivalently, for the permeability, we have

$$
\mathcal{M}ax\left(\mu_{mRe}\right) \simeq 1 - \frac{F}{8} + \frac{F^3}{2P}
\tag{4.39}
$$

4.5 Contribution

I presented fundamental limitations on the performance of artificial magnetic materials. A fundamental constraint expressing the effect of the relative permeability on the relative bandwidth were derived for the lossless and lossy structures. It is shown that the achieved restriction is general and does not depend on the shape of the metallic inclusions comprising the artificial magnetic medium.

The effect of the physical parameter P and geometrical parameter F, introduced in the model presented in chapter 3, on the effective permeability of the medium and the magnetic loss tangent were studied. It was found that increasing F increases the effective permeability of the medium, however, it also leads to increased dispersion. Increasing the geometrical factor F was found to decrease the loss. It was also found that the physical parameter, P has very little impact on the effective permeability and dispersion; however, it affects the loss more pronouncedly. Therefore, there is a tradeoff between increasing the permeability and decreasing the loss on the one hand, which results from increasing F, and reducing dispersion, on the other hand by decreasing F. In other words, designing inclusions with larger surface area (i.e., increasing F) results in lower loss and higher value for permeability; however, this leads to an increase in the rate of change of permeability with frequency, thus higher dispersion.

A simple but general enough circuit-based model is used for calculating the magnetic behavior of inclusions and the slab itself. Although more elaborate model proposed in literature [44], [49] consider more circuit components such as the capacitance

of the inclusions gap, inductance of the metallic routes and mutual induction between adjacent inclusions, it has been shown that the general functionality of the effective magnetic behavior of inclusions will not change [1], [2]. Thus, the derivations and conclusions, in essence, are general, and they can be applied for any application and design. It is worth noting that in this work, I only considered the magnetic loss, however, the total loss in the medium can be comprised of electric and magnetic losses. Moreover, an approximate limit for the maximum permeability attainable from an AMM and its corresponding normalized frequency are calculated.

The constraints and relations derived in this work can be used to methodically design artificial magnetic material meeting specific operational requirements.

Chapter 5

Design Methodology

In this section, I introduce a design recipe for AMMs. I propose a strategy and approach to design an AMM with specified unit cell size and effective magnetic permeability larger than unity over a range of frequencies. The resonant frequency of the inclusions can be set through the design procedure, but the permeability is designed for minimum allowable dispersion within the frequency band. Moreover, the design is desired not to exceed a certain magnetic loss tangent over a specific frequency range. The outcome of the design is the dimension of the inclusion or the geometrical and physical parameters of the medium. However, many fabrication and structural parameters cannot be varied due to fabrication and design constrains, such as the thickness of the metal of the board, the conductivity of the conductor, the permeability of the host medium, or width of the conductor's routes. Therefore, all these values will be considered as design constraints.

The procedure is summarized as follows: First step is testing the feasibility of the design. In this step, the requested values will be tested against the fundamental limitations of AMMs as discussed in [70], [56]. In the next step, by using the fixed and requested design parameters, and employing relations (3.38) and (3.39), a valid interval for the resonance frequency of the inclusions and subsequently for the geometrical and physical factors will be calculated. The provided intervals of parameters specify the magnetic properties of the structure within a range in which the desired values are located. In the third step, the frequency range of the resonance frequency and the geometrical and physical factors are modified to achieve a suitable tolerance for
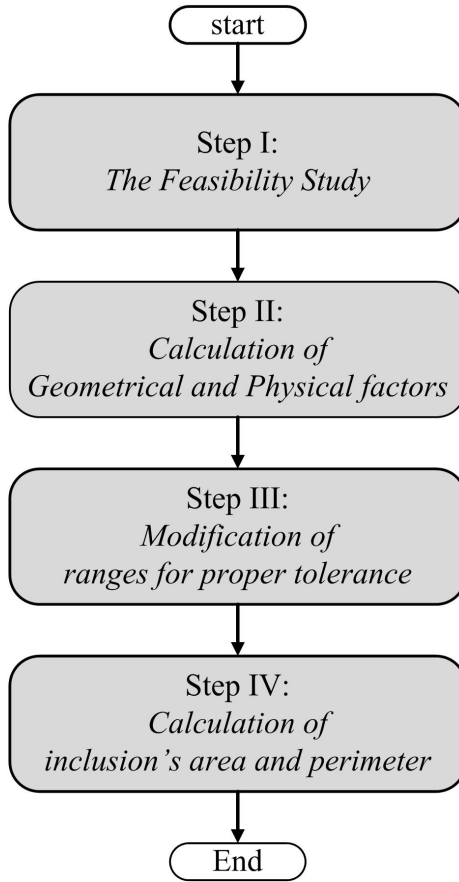
Figure 5.1: The flowchart shows the main steps to derive the geometrical and physical factors from which the area and perimeter of inclusions will be determined.

the magnetic properties of the structure. Although a very narrow range of tolerance can be obtained, it is preferable to determine the design ranges constrained by fabrication and application tolerances. Finally, by using the two calculated geometrical and physical factors, the length and area of inclusions will be derived. Fig.5.1 shows the main steps of the design methodology. A case study is considered next.

To the best of my knowledge, the synthesis approach that has been pursued in this work was never attempted before. However, a 3D full-wave simulation-based optimization algorithms can be applied to synthesize, if possible, an AMM's inclusion to achieve certain real and imaginary permeability over a specific frequency band. These algorithms extremely expensive in terms of run-time and memory requirements. For

instance, performing an optimization based on Genetic Algorithm (GA) to achieve an inclusion for a specific design needs about 10^5 epochs of a 3D full-wave simulation. Each simulation to obtain the permeability function takes a couple of hours on a modern PC with 4GB of RAM and a Quad-core Intel CPU. Thus, the total optimization time is more than 274 years (10^5 hours). Moreover, the optimization process doesn't show that if the design problem is realizable with any inclusion or not. Indeed, an non-realizable problem leads to an everlasting optimization process if memory allows. Therefore, using an optimization algorithm wouldn't be a possible methodology to design an inclusion with specific magnetic properties.

5.1 Design Case Study

In this section, the design procedure for determining the geometry of the inclusions for AMMs is described in details through a case study. Table 5.1 shows an example of a design request sheet. The designed structure can possibly be used as a substrate for miniaturizing a patch antenna operating at $600MHz$. Some variables such as conductivity and host medium permittivity were set. The design needs to meet a number of conditions such as μ_{Re} at a specific operational frequency of $f_{op} = 6.00 \times 10^8 Hz$ is equal $9.00 \pm 5.0\%$ within the frequency range of at least $2MHz$, and MLT of less than 5.00×10^{-2}.

5.1.1 Step I - The Feasibility Study

First, I verify if the frequency bandwidth is achievable within the specified tolerance for the permeability. Recall from (4.18):

$$\frac{BW}{\omega_{op}} \leq \frac{1}{2\chi_{op}} \left(\frac{\delta\mu}{\mu_{op}} \right) \tag{5.1}$$

where ω_{op}, μ_{op} and χ_{op} are the operational frequency, the effective permeability and the magnetic susceptibility, respectively. BW and $\delta\mu$ represent the frequency bandwidth and the permeability deviation, respectively. (Note that the operational frequency should not be confused with the resonance frequency of the inclusion. The

44

operational frequency basically represents a specific frequency at which certain application, say an antenna, is operating).

The second constraint is to find a boundary for the physical and geometrical factors by setting the maximum of the permeability function over all frequencies (see Fig.3.4) high enough to cover the effective permeability requirement declared in Table 5.1. From Table 5.1, the real effective permeability is $8.55 < \mu_{Re} < 9.45$, as such, the maximum of the real effective permeability function should be larger than 9.45 ($\mu_{\max} > 9.45$). Recall from (4.39):

$$\mu_{\max} \simeq 1 - \frac{F}{8} + \frac{F^3}{2P} \tag{5.2}$$

Substituting the upper value of the permeability from Table 5.1 for $\mu_{\max}$, (5.2) can be rearranged as:

$$P < \frac{4F^3}{67.6 + F} \tag{5.3}$$

which for $F = 1$ (F upper bound), one can get $P < 0.0583$, an upper limit for P.

5.1.2 Step II - Calculation of the Geometrical and Physical Factors

In this step, first valid ranges for the normalized operational frequency, geometrical factor and physical factor are being calculated consecutively. Then, by considering the constraint on the maximum value of the permeability introduced in step I, ranges are being modified for each parameter.

Solving the relation (3.38) and (3.39) simultaneously for a given value of the real effective permeability and the magnetic tangent loss, we obtain:

$$\xi(\Omega_{op}) = \left[\frac{\mu_{Re\,op}}{\chi_{m\,op}} \tan \delta_{op}\right]^2 \tag{5.4}$$

$$\chi_0(\Omega_{op}) = \chi_{m\,op} \left(1 + \left[\frac{\mu_{Re\,op}}{\chi_{m\,op}} \tan \delta_{op}\right]^2\right) \tag{5.5}$$

45

Table 5.1: Design Data Sheet

Material Specifications
Host medium: `Duroid 5880` ($\varepsilon_r = 2.2$)
Traces: `Copper`($\sigma = 59.6\frac{S}{\mu m}$)
Fabrication Technique Parameters and Design Dimensions
Trace width: $b = 200\mu m$
Trace gap: $g = 800\mu m$
Metal thickness: $t = 35\mu m$
Fabrication tolerance: 0.25%
Unit cell size: $(\delta x, \delta y, \delta z) = (20.0mm, 800\mu m, 20.0mm)$
Design Request
Inclusion type: `Metasolenoid`
Operational frequency: $f_{op} = 600MHz$
Real effective permeability: $\mu_{op} \pm \delta\mu = 9.00 \pm 5.0\%$
Bandwidth: $BW \approx 2MHz$
Magnetic Loss Tangent (MLT): $\tan\delta < 0.050$

Substituting from Table. 5.1 in (5.4) and (5.5), we obtain $\xi(\Omega_{op}) = 3.164 \times 10^{-3}$ and $\chi_0(\Omega_{op}) = 8.025$. Afterwards, ξ and χ are considered fixed parameters for the design, and Ω and P are calculated based on a valid range of F, accordingly.

By considering the definition (3.34) and sweeping F over the possible range of $[0, 1]$, the normalized operational frequency falls within $[0.9430, 1]$. Then, by using data set of (F, Ω_{op}) obtained from (3.34), the physical factor P is calculated from (3.35), and the graph of P is plotted versus the geometrical factor F in Fig.5.2. The graph shows a valid range of $[0, 0.0068]$ for P. In fact, any point on the graph in Fig.5.2 corresponds to a possible pair of (F, P) meeting the properties promised in Table.5.1 except the fact that one needs to choose a suitable pair for which the design works at a specific operational frequency (here; $600MHz$).

Next, the calculated ranges are modified to a smaller range by applying the inequality in (5.2). From Fig.5.2, the upper bound of P can be read as 6.806×10^{-3} which is clearly less than 0.0583 (see the example illustrated for inequality (5.2)). Based on the relation (5.2), $P = 6.806 \times 10^{-3}$ limits F from the below to 0.4875
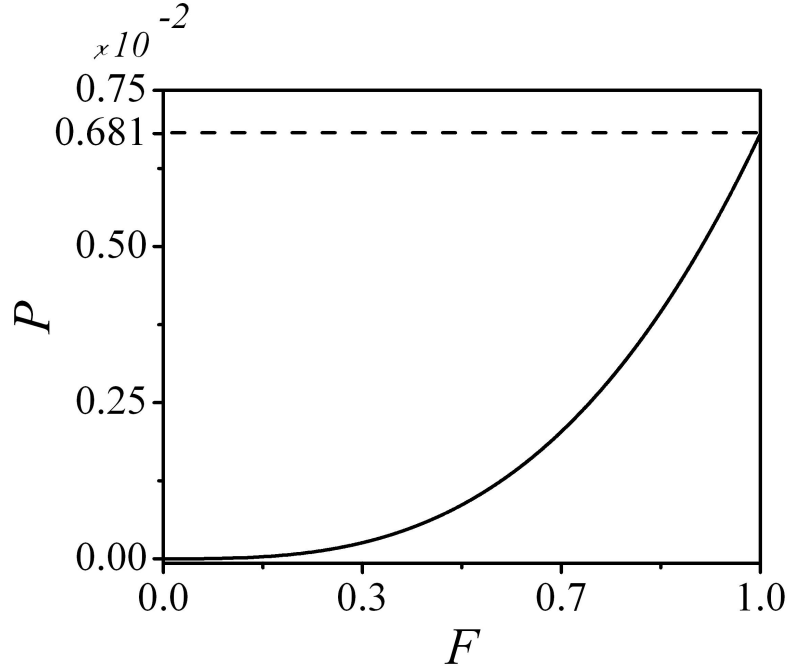
Figure 5.2: Any point on the curve represents a pair of (F, P) for which the design meet desired properties introduced in Table. 5.1.

leading to a new valid range of $[0.4875, 1]$ for F.

Fig.5.3 shows the normalized operational frequency plotted versus F with the banned values of F cross-hashed in the figure. The graph shows a valid range of $[0.9430, 0.9710]$ for Ω_{op}. The banned range of F has also been cross-hashed in the graph of P versus F (see Fig.5.4). In fact, in Fig.5.3 and Fig.5.4, the white region represent the criteria in which the maximum of the real effective permeability function goes above the requested permeability (here; 9.45).

5.1.3 Step III - Resonance Frequency Calculation

In this step, the resonance frequency for the the design is determined iteratively. Each iteration involves two parts; first, calculating a range for the resonance frequency and
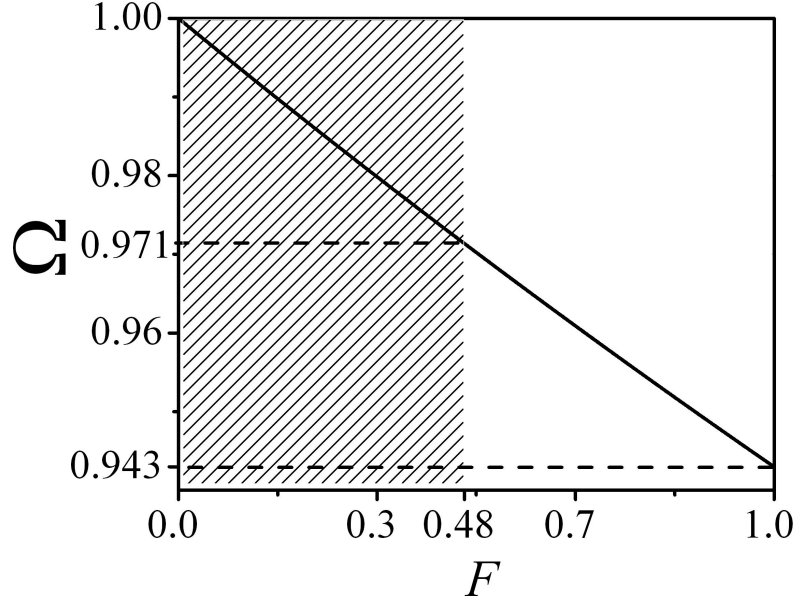
Figure 5.3: The graph shows the relation between the normalized frequency Ω and the geometrical factor F. The hashed area is an area which the peak of real effective permeability function goes under the requested permeability.

then modifying the calculated range for the geometrical and physical factors. If the iterations is successful, smaller ranges for the resonance frequency, the geometrical and physical factors are achieved. The iterations is continued so that the variations of the physical and geometrical factors over their calculated ranges are less than the fabrication tolerance indicated in the Table. 5.1. This is due to the fact that the variation of dimensions linearly affects the geometrical and physical factors [70].

In the first part, by using the data obtained in the Step II for the physical factor P, the material specifications and fabrication characteristics provided in Table. 5.1 and (3.22), an interval for the feasible resonance frequency of the realizable inclusions is calculated. Fig.5.5 shows the calculated resonance frequency as a function of P and F. Also, the improper values of F has been cross-hashed in Fig.5.5. (Note that due to the fact that F and P are not linearly dependant, the scale for the F axes remained linear, however, the P axes is not linear. Therefore, each value on the P
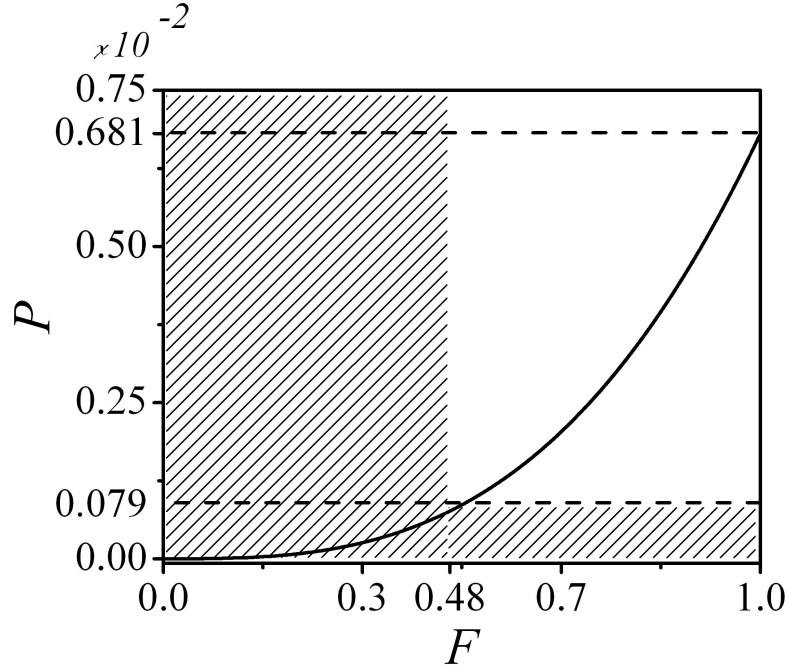
Figure 5.4: The banned area in Fig.5.2 introduced by inequality (5.2) has been cross-hashed. The white area is the permitted range for pairs of (F, P).

axes pertains to its F correspondent pair).

From Fig.5.3, It can be seen that $0.9430 < \Omega_{op} < 0.9710$ which corresponds to $617.9MHz < f_{res} < 636.3MHz$ ($617.9MHz = \frac{f_{op}}{0.9710}$). The calculated range for the resonance frequency has been marked in Fig.5.5 with two horizontal dashed-lines.

In the second part, by using (3.27) and the calculated range of the resonance frequency, the range for the physical factor is modified. Also, as the physical and geometrical factors are coupled through relation (3.35) (also, see Fig.5.4), a range for the geometrical factor is modified. The vertical dashed-lines in Fig.5.5 shows the newly modified ranges of the physical and geometrical factors. From Fig.5.5, the ranges of F and P can be read as $0.4916 < F < 0.5038$ and $8.209 \times 10^{-4} < P < 8.833 \times 10^{-4}$, respectively.

At this stage, the first iteration is over. The modified ranges of F and P are used
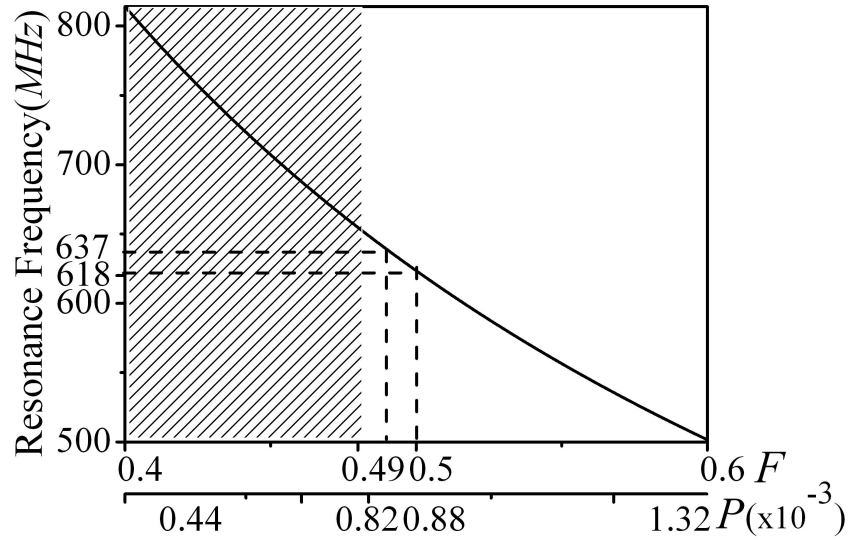
Figure 5.5: The graph shows the relation between the resonance frequency f_{res} (on vertical axes) and the geometrical factor, F (upper horizontal axes) and the physical factor, P (lower horizontal axes). The scale on F axes is linear, however, the scale on P axes is not linear.

for calculating the resonance frequency in the next iteration. With the new range of F and P, by referring to Fig.5.3, the normalized operational frequency and consequently the possible range of the resonance frequency are modified to $0.9700 < \Omega_{op} < 0.9707$ and $619.1MHz < f_{res} < 619.6MHz$.

Note that the updated range of the resonance frequency is within the previously calulated range of the resonance frequency. In general, it is not obvious that these two intervals overlap. There are three possible cases. Let $\mathcal{I}_i$ be the range of the resonance frequency calculated in the i-th iteration:

- Case 1: If $\mathcal{I}_i \subset \mathcal{I}_{i-1}$, then the new range of the resonance frequency is considered as $\mathcal{I}_i$.

- Case 2: If $\mathcal{I}_i \not\subset \mathcal{I}_{i-1}$ and $\mathcal{I}_{i-1} \cap \mathcal{I}_i \neq \emptyset$, the intersecting range would be considered as the valid range and it is renamed to $\mathcal{I}_i$.

50

- Case 3: If $\mathcal{I}_{i-1} \cap \mathcal{I}_i = \emptyset$, then no design will be obtained with the defined set of parameters. An option to provide a solution is to change the structural or fabrication parameters such as permeability of the host medium, the thickness of the conductor traces and the gap between traces.

In summary, after performing the second iteration, the values for the set $\{\Omega_{op}, F, P\}$ can be chosen from the following intervals:

$$\begin{cases} \Omega_{op} \in [0.9700, 0.9707] \\ F \in [0.4916, 0.5038] \\ P \in [8.209, 8.833] \times 10^{-4} \end{cases} \tag{5.6}$$

Note that any valid set of $\{\Omega_{op}, F, P\}$ from (5.6) specifies inclusions producing an AMM with $\mu_{Re} = 9$ and $\tan \delta < 0.05$ at the operational frequency of $f_{op} = 600 MHz$.

Next, one needs check the tolerance of F and P to determine whether to terminate the iterations and go to the next step or to proceed to the third iteration and obtain narrower ranges. From (5.6), $\delta F/F = 2.45\%$ and $\delta P/P = 7.32\%$, both are larger than the fabrication tolerance declared in Table. 5.1, thus requiring further iteration. Applying the third iteration, the lower and upper bound of the ranges of F and P become identical up to three significant digits. Therefore, F and P tolerances are smaller than the fabrication tolerance, and the iterations are terminated resulting in the following values (calculated up to three significant digits):

$$\begin{cases} \Omega_{op} \cong 0.970 \\ F \cong 0.503 \\ P \cong 8.88 \times 10^{-4} \\ f_{res} \cong 619.5 \times 10^8 \end{cases} \tag{5.7}$$

Fig.5.6 shows the result of the second and the third iterations. Note that although the number of iterations depends on the desired accuracy of the design, inaccuracy in the circuit-based model and fabrication tolerances alter the characteristics of the fabricated AMM from the designed properties. Thus, it is sometimes preferable to run Step II one iteration less than the final iteration to have wider ranges for the design parameters (i.e., F, P and f_{res}).
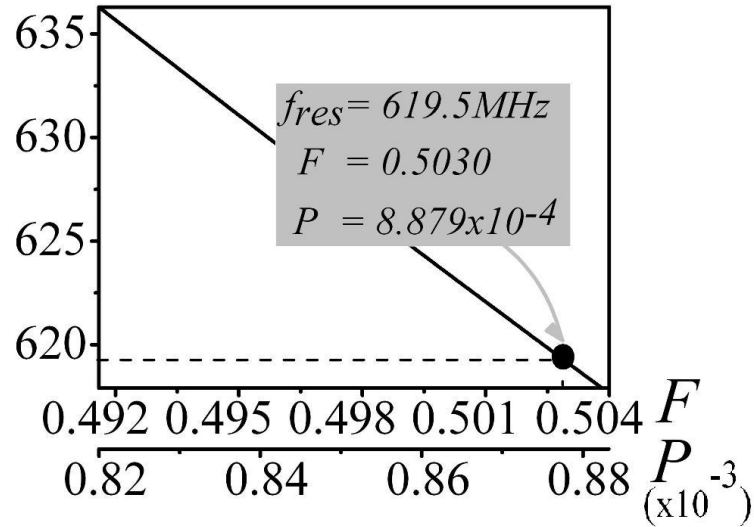
Figure 5.6: The graph shows the relation between the resonance frequency f_{res} (on vertical axes) and the geometrical factor, F, (upper horizontal axes) and the physical factor, P, (lower horizontal axes). Also, the calculated parameters in the third iteration marked in the graph.

Before continuing to the next step, one needs to check if the calculated parameters are substituted in the model (Eq. 3.38), the structure meets the design specifications. Based on the parameters calculated in (5.7), the permeability and MLT have been calculated over the requested bandwidth, and the results were summarized in Table.5.2. From Table.5.2, it can be seen that the requested frequency bandwidth of $2MHz$ associated with a permeability deviation of about 10% is satisfied.

According to Table.5.2, the MLT at the upper frequency is about 9% above the requested threshold. This is due to the fact that in the design procedure (specifically when using (5.5) and (5.4)) the value of MLT is kept 0.050 at the operational frequency $f_{op} = 600MHz$. As the MLT is a monotonically increasing function (in absolute value) before the resonance frequency, the MLT becomes less than 0.050 at the lower side of the frequency band, and becomes higher than 0.050 at the upper side of the frequency band. Because the slope of the MLT function is not clear a priori,

Table 5.2: The output summary of the design

$freq(MHz)$	μ_{Re}	$tan\delta$
599	8.58	0.047
600	9.00	0.050
601	9.48	0.054

there are two possible ways to address this issue. First, the designer can perform the design procedure by choosing a random number smaller than the value declared for MLT in the Table.5.1. This method has the risk of choosing a number too small which might fail the design procedure or choosing a number not small enough resulting in MLT violating the desired criteria. The second option is to repeat the design procedure by subtracting the MLT at the operational frequency from the difference of the MLT at the upper side of the frequency band and the desired value of MLT. For instance, in the case study considered here, the adjusted value of MLT is 0.46. This option incurs the cost of repeating the procedure one more time but it confidently gives the proper result as the MLT function curves upward for frequencies closer to the resonance frequency, and it gives a safe side for the new design so that the new MLT at the upper side of the frequency band does not exceed the desired criteria.

5.1.4 Step IV - Perimeter and Area of the Inclusion

In this step, the area and the perimeter of inclusions are determined by using the geometrical factor and the resonance frequency calculated in step III. From (3.25), the area of an inclusion is $s = FA$. Also, the perimeter and area of an inclusion are connected through the resonance frequency of the inclusion, i.e., $l = [\mathcal{Q}/2\pi f_{ref}]^2 s^{-1}$ (see (3.18)). Using these relations, the perimeter of the inclusion is plotted in Fig.5.7 versus its area over the calculated range of the resonance frequency given by (5.6).

Each point *(area,perimeter)*$=(s,l)$ of the curve in Fig.5.7 introduces a contour $\Gamma(s,l)$ with the perimeter of l and the area of s. The contour can accept any topology as long as it fits the pair (s,l).

Let $\mathcal{G}$ introduce the set (s,l) which is the outcome of the design procedure. From Fig.5.7, the end points of the *sl*-curve are:
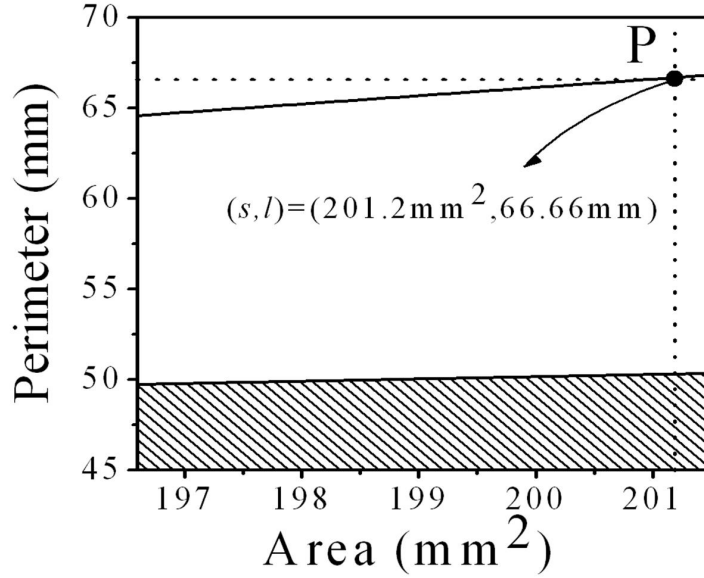
Figure 5.7: The graph shows the relation between s and l. The hashed region describes pairs of (s,l) which do not fit in any physically realized geometry.

$$(196.6mm^2, 64.56mm), (201.5mm^2, 66.79mm) \in \mathcal{G} \tag{5.8}$$

The point $P(201.2mm^2, 66.66mm)$ corresponds to the selection in (5.7). In fact, an AMM composed of inclusion's topologies with the area and perimeter equal to $201.2mm^2$ and $66.66mm$, respectively, create an analytical magnetic response similar to what summarized in Table.5.2.

Despite of the fact that the set $\mathcal{G}$ has been obtained from the physics of the problem, the pair (s,l) may or may not be fit in an actual geometrical shape. Based on Dido's isoperimetric problem [71], among all possible contours with the same surface area, the circle provides the minimum circumference. Hence, for a certain area s and perimeter l, an actual geometry satisfies Dido's inequality formulated as:

$$l \geq 2\sqrt{\pi s} \tag{5.9}$$

In Fig.5.7, the region corresponding to non-realizable geometries is cross-hashed. It can be seen from the figure that all inclusions introduced by the curve are realizable.

In other words, no pair (s, l) of inclusions introduced in $\mathcal{G}$ will be eliminated by Dido's geometrical constraint. If the set of pairs (s, l) which satisfies Dido's inequality is denoted by $\mathcal{D}$, the outcome of the design procedure is $\mathcal{G} \cap \mathcal{D}$.

In General, there are three possibilities for a curve characterized by s and l according to Dido's inequality. These possibilities are:

- Case 1: If $\mathcal{G} \subset \mathcal{D}$, then $\mathcal{G}$ is the outcome of the design procedure.

- Case2: If $\mathcal{G}$ is not completely located in $\mathcal{D}$, then $\mathcal{G} \cap \mathcal{D}$ is the outcome of the design procedure.

- Case3: If $\mathcal{G} \cap \mathcal{D} = \emptyset$, the design procedure does not provide any inclusions geometry to meet the design objectives. An option to provide a solution is to change the structural or fabrication parameters such as permeability of the host medium, the thickness of the conductor traces and the gap between traces.

Note that, as $0 < F < 1$, from (3.25), $0 < s < A$. In other words, the maximum inclusion's area which can be determined through the design methodology is less than the unit cell area A. The inclusion's perimeter is only limited from below to $2\sqrt{\pi s}$ due to Dido's inequality, and it doesn't have an upper limit. Therefore, the inclusion's perimeter can be determined to any value through the design methodology.

Fig.5.8 summarizes the design steps in a flowchart. It can also be proved that the proposed routine converges. The details of this proof is left for future work.

5.2   Discussions

5.2.1   Accuracy of the Circuit Model

Due to the small feature size of the inclusions in a composite medium and the small skin depth compared to the radiation field wavelength, the magnetic response of such a medium can be simply interpreted in terms of the geometrical parameters of the inclusions rather than electromagnetic properties of the metals. This fact, for frequencies reaching up to mid-IR, has been reported in the literature [27], [29]. However, in general, an interpretation of the magnetic response of artificial magnetic materials

based on only the area and perimeter of the inclusions is an approximate calculation. Some possible sources of the approximation are using a solenoidal estimation of the magnetic flux passing through inclusions, neglecting the capacitance of the inclusions' slit, and ignoring the variation in the curvature of the inclusions along the metallic trace. In addition, in the case of inclusions having a small area and large perimeter, there is a capacitive coupling across the different part of an individual inclusion. Moreover, the model fails for a lattice of discrete inclusions (inclusions with different geometry). However, it is important to note that if the magnetic response of the structure can be modeled by an RLC resonance circuit, it can consequently be expressed in terms of the geometry of the inclusions. The first two components for geometrical interpretation of a contour are the area and the perimeter of an inclusion. The area is related to inductance and the perimeter, to capacitance. This idea is widely used in the literature to derive the circuit model for AMMs. Many models express their calculations based on the capacitance per unit length and inductance per unit area. Therefore, this concept can be used as the first, simple and proper approximation for study of the magnetic behaviour of the medium. Incorporating the effect of the inclusion's curvature for improvement of the present model would be a part of the future work. The preliminary work can be reviewed in a previously published conference paper [III].

5.2.2   Operational Frequency

Note that most circuit models present a rough estimation of magnetic behaviour of an AMM at the vicinity of the resonance frequency. Therefore, while the observing frequency is moving away from the resonance frequency, the circuit models provide more accurate results, and many factors which are effective at resonance frequency are negligible at lower frequencies. I stress that my design methodology aims to provide a design recipe for an application that require a positive and low dispersion permeability. This can be achieved by an AMM designed to work in frequencies sufficiently away from the resonance frequency of the inclusions. In addition, the model has been tested and simulated for various design cases based on the proposed design methodology; the results showed a reasonable consistency with the desired properties. Some cases are illustrated in the following chapter.

5.2.3   Strategy in Methodology

Although the design methodology needs to incorporate a specific circuit model, it can be applied to many circuit models available in the literature. In fact, the design recipe has been developed based on a generic strategy. An interested designer may apply the same strategy to his/her personal circuit model describing an AMM, and develop a similar recipe. The circuit model exploited in this chapter is simple but general and useful, and it is used to convey the strategy behind the methodology.

The significant elements of the strategy are to extract the geometrical and physical components, and to segregate the frequency dependency in a function form. The main and most important fact of the re-formulation process (see chapter 3) is that the geometrical and physical components in a circuit model were extracted, and the extracted factors were encapsulated in a few new parameters which are frequency independent. This approach is also applicable to any new and extensively elaborated model.

Hence, the proposed methodology is generic and its accuracy can be improved by adopting a new circuit model and modifying the proposed design recipe.

5.2.4   Spatial Dispersion

The AMMs are characterized based on not only time-dispersion but also spatial dispersion. The source of spatial dispersion is the phase alteration while the electromagnetic wave is propagated throughout the AMM. In fact, the spatial dispersion would be effective for small wavelength limits (i.e. higher frequencies) for which the wavelength and the feature size of the structure (such as the unit cell size) are comparable. For large wavelengths, the spatial dispersion is negligible and the time dispersion is significantly dominant.

Baena *et al.* presented a general circuit model describing the effect of the spatial and temporal dispersion in AMMs [72]. They proposed a circuit model which describes both time and spatial dispersion of AMMs. Applying the same strategy, one can define a procedure for designing an AMM which considers the spatial dispersion as well.

5.2.5 Effects of Bianisotropy

The structure designed by the proposed methodology is bianisotropic. This phenomenon has been studied in the literature such as in the work of Marques *et al.* [36]. However, the defined methodology only addresses the magnetic response and design for specific magnetic characteristics of the medium, and the electric response was not the focus of this investigation. Without a doubt, it could be a motivation to a new study for designing AMMs with specific magnetic and electric properties. However, it limits the range of possible design, as it needs to fulfill two criteria (magnetic specifications and electric specifications) rather than solely the design for magnetic properties. Consequently, the enhanced design methodology, if possible, considers the bianisotropy effect, which would reduce the possibility of design, due to higher restriction. For example, instead of fulfilling a specific magnetic property, the structure has to fulfil excessive electric properties throughout the design procedure; proposing a design algorithm for a specific magnetic response is crucial.

5.3 Contribution

I proposed a novel design methodology for artificial magnetic material with desired properties. The design methodology was developed based on a circuit model presented in chapter 3. The analytical model shows that the magnetic properties such as the real effective permeability, the magnetic tangent loss, and the flatness of the permeability function of the medium, all depend on the geometrical properties such as surface area and perimeter of the inclusion. A four-step iterative design methodology was proposed for design of AMMs. In the first step, the feasibility of the design is tested to meet the fundamental constraints. In consecutive steps, the geometrical and physical factors of the inclusion are synthesized, and finally the area and perimeter of the inclusion is calculated. An updated range of the inclusion's area and perimeter is obtained through consecutive iterations. Finally, if the outcome of the iterative procedure results in geometrical parameters that satisfy Dido's criterion, then a physical geometry exists, thus meeting the design specifications. At the end of the chapter, a discussion to check the validity, universality, reliability, robustness and accuracy of the proposed design methodology is presented. It is noticeable that other circuit

models with more accuracy to describe AMMs' behavior can be adopted. However, the strategy behind the design methodology is nonetheless generic and can be applied to any adopted circuit-based model for AMMs.

In addition, a software code has been developed to automatically design an AMM meeting desired properties. The code receives the magnetic properties of desired AMM as an input, and generates the resistance per unit length R_0, capacitance per unit length C_0, inductance per the area L_0, $\mathcal{K}$ parameter as an intermediate output. The software also produces a series of intervals for geometrical factor F, physical factor P, normalized resonance frequency Ω, resonance frequency ω_0, area s, length l, real part of effective permeability μ_{Re} and magnetic tangent loss $\tan\delta$ at each iteration. The code provided in Appendix B for academic purposes.
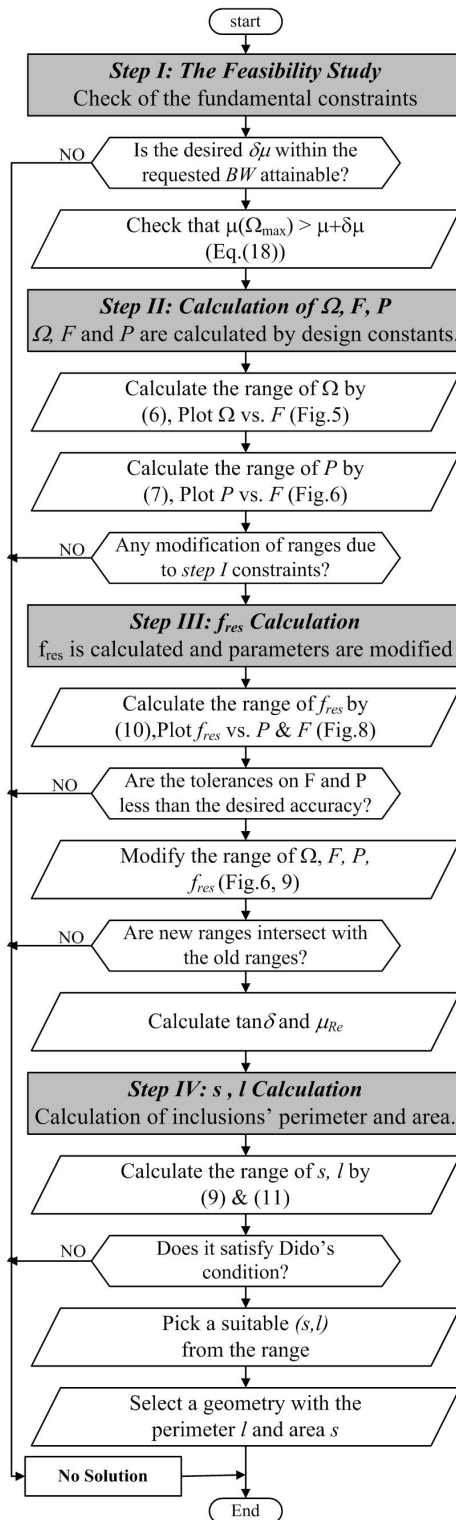
Figure 5.8: A flowchart as the design methodology.

Chapter 6

Inclusion's Geometry

Metallic open-loop inclusions are categorized in two general geometrical patterns based on the number of loops of inclusions and the coupling scheme. The first category are inclusions with multiple elements such as double split ring resonators (Fig.2.2-a) and double split square ring resonators (Fig.2.2-b) or single element but spiral (Fig.2.2-d,-e,-f) or helical shape. The second category divides inclusions into broadside-coupled or edge-coupled. Fig.6.1 shows an arbitrary inclusions contour in different categories.

The most common inclusions are split circular ring resonators and split square ring resonators. The area Ar and the perimeter Pr of a square and a circle are related through the equations of $Pr^2 = 16Ar$ and $Pr^2 = 4\pi Ar$, respectively. Therefore, the area and perimeter of the circle and square are strongly dependent, and either cannot be tuned independently of the other. Hence, the circle or the square cannot be options

(a)   (b)   (c)   (d)
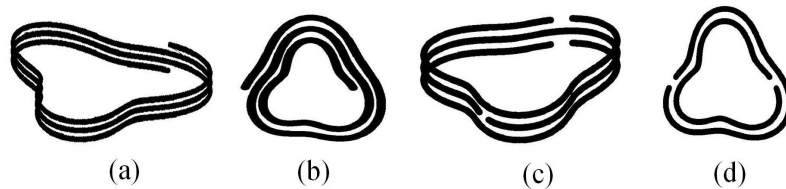
Figure 6.1: Different categories of inclusions. (a) Broadside-coupled 3-turn helical inclusion, (b) Edge-coupled 2.5-turn spiral inclusion , (c) Broadside-coupled triple split looped inclusion, (e) Edge-coupled double split looped inclusion.

for the geometry of the inclusions of an AMM with desired properties. Unlike the circle and square, the rectangle and ellipse provide independent area and perimeter relations. For the rectangle or the ellipse, the area and perimeter can be formulated using a system of equations in terms of two sides of the rectangle or in terms of the semimajor and semiminor axes of the ellipse.

For a given (Ar, Pr) pair describing an inclusion, and considering the rectangle for the inclusion's shape, the sides d_1, d_2 of the rectangle are determined by the roots of the following quadratic equation in terms of d_i where $i = 1, 2$:

$$d_i^2 - \frac{Pr}{2}d_i + Ar = 0 \tag{6.1}$$

When considering the ellipse as the inclusion's shape, the semimajor axis r_M and semiminor axes r_m of the ellipse are the roots of the following integral equation in terms of r_i where i stands for M, m:

$$Pr = 4r_i E\left(\sqrt{1 - \left(\frac{Ar}{\pi}\right)^2 r_i^{-4}}\right) \tag{6.2}$$

where $E(k) = \int_0^{\frac{\pi}{2}} \sqrt{1 - k^2 \sin^2 \theta} \, d\theta$.

Equation (6.1) has a real solution if $Pr^2 \geq 16Ar$. This inequality provides more restriction on the (s, l) pair calculated through the design methodology with respect to Dido's inequality. In summary, there is a set of geometrically realizable (s, l) pairs (i.e, $\{(s, l) | 2\sqrt{\pi s} \leq l \leq 4\sqrt{s}\}$) which cannot be realized in a rectangular topology.

Another constraint on the (Ar, Pr) pair is that the realized geometry has to be bounded within the unit cell area. It was shown in the first part of this paper that the s value determined through the design steps is bounded above by the inclusion's unit cell area. Therefore, $Ar \leq \delta x \cdot \delta z$, where δx and δz are the dimensions of the unit cell of an AMM. For the rectangular and elliptical shape inclusions, although the area and perimeter values are independent, the calculated sides of the rectangle or the major axes of the ellipse need to be smaller than the unit cell dimensions (for the rectangle: $d_i \leq \min(\delta x, \delta z)$ and for the ellipse: $r_M \leq \min(\delta x, \delta z)$).

These constraints define a set of restrictions on the the (Ar, Pr) pair realizable by a rectangular or elliptical shape. For a rectangular shape inclusion, we have

$$\begin{cases} 0 & < Ar < & \delta x \cdot \delta z \\ 4\sqrt{Ar} & < Pr < & 2(\tau + \frac{Ar}{\tau}) \end{cases} \qquad (6.3)$$

where $\tau = \min(\delta x, \delta z)$. Therefore, the maximum perimeter which can be obtained by rectangular inclusions is $2(\delta x + \delta z)$. Also, by considering the constraints for an elliptical shape inclusion, we have:

$$\begin{cases} 0 & < Ar < & \frac{\pi}{4} \delta x \cdot \delta z \\ 2\sqrt{\pi Ar} & < Pr < & 2\sqrt{\frac{1}{8}\pi^2\tau^2 + \frac{2Ar^2}{\tau^2}} \end{cases} \qquad (6.4)$$

From (6.4), the maximum area and perimeter which can be obtained by an elliptical inclusion are 78.5% of the unit cell area and $\pi\sqrt{\frac{\delta x^2 + \delta z^2}{2}}$, respectively.

As an example, I consider a Design Data Sheet discussed in the previous chapter of this work. As a result, an AMM is designed to meet the desired criteria addressed in Table 5.1. The AMM is composed of inclusions with the following (s, l) pair (recall from chapter 5):

$$(s, l) = (201.2 mm^2, 66.66 mm) \qquad (6.5)$$

If considering rectangular inclusions, then by solving equation (6.1), the dimensions of the inclusions are obtained as $d_1 = 25.4mm$ and $d_2 = 7.92mm$. The values for the dimensions of the inclusions are not acceptable because the larger side of the rectangle exceeds the unit cell size ($d_1 = 25.4mm > \delta x = 20.0mm$). Therefore, there are no rectangular inclusions to provide the desired magnetic properties.

In the case of the elliptical inclusion, by solving equation (6.2) , the semimajor and semiminor axes of the ellipse are obtained as $r_M = 15.4mm$ and $r_m = 4.16mm$. As $2r_M = 30.8mm > \delta x = 20.0mm$, thus, the ellipse cannot be confined within the unit cell.

When the calculated dimensions of the rectangular or elliptical inclusions exceed the AMM's unit cell dimensions, neither of the two geometries become a feasible choice for the inclusions shape, as a single inclusion cannot exceed the unit cell area.

In an AMM, the magnetic flux generated by the current induced on the open-loop inclusions due to the presence of an external magnetic field passes through adjacent

inclusions and enhances the magnetic flux density in the medium. Therefore, the medium is magnetized. As the inclusions are periodically distributed in an AMM, at the unit cell level, the fractional area F of the unit cell occupied by the inclusion plays the key roll in magnetization of the AMM. In fact, a larger fractional area receives more magnetic flux leading to a larger magnetization. Since $0 < F < 1$, for a given unit cell area $A = \delta x \cdot \delta z$, we have $0 < s < A$. This inequality gives an upper limit for the inclusion's area and it reveals that the fractional area is a real design parameters. Consequently, the unit cell area can be a fixed design parameter, as it has been given in Table.5.1. Note that to meet desired magnetic properties for an AMM, the perimeter of the inclusions can vary as long as it does not violate the Dido's inequality.

Thus far, it has been shown that the inclusions proposed in the literature are not appropriate candidates for a generic inclusion topology by virtue of having several geometrical limitations. my goal is to formulate generic inclusion that can be configured to produce all geometrically realizable combination of (s, l) pairs.

Three types of parametric geometries are proposed to achieve inclusions with specific area and perimeter combination while confined to a specific unit cell. The first type has a circular base combined with a sinusoidal curve, the second type has a square base combined with a square-wave curve or corrugation on its sides, and the third type is a grooved oval shape varying from an ellipse to a rectangle. Throughout, I will assume that the inclusion's trace width and thickness to be negligible.

6.1 The nth order Rose Curve Resonators, $R_n(r_0, a)$

The first inclusion's geometry is a circle which is combined with a sinusoidal curve. Henceforth, the pattern is referred to as the Rose curve (see Fig.6.3). The area of the produced curve is approximately equal to the area of the base circle because the area added with the sinusoidal crests are equal to the area reduced with the sinusoidal troughs. Although the area of the shape remains similar to the original circle, the desired perimeter can be adjusted by tuning the amplitude and choosing the frequency of the sinusoidal function. The fact that the area and perimeter of the Rose curve can be adjusted individually makes the Rose curve topology a suitable candidate for the geometry of a generic inclusion. The following equation characterizes the nth order

64

Rose curve in the polar coordinate system:

$$R_n(r_0, a) : r(\theta) = r_0 + a\cos(n\theta) \tag{6.6}$$

where $r(\theta)$ represents the position of the contour in the xz-plane, and the angle θ sweeps the curve aside from a small slit on the contour and is measured from the x-axis; thus, $\theta \in [\frac{h}{2}, 2\pi - \frac{h}{2}]$, where h is the width of the curve's opening in radians. a is the amplitude of the sinusoidal function added to a circle with the radius r_0. The order of the Rose curve, n is a positive integer number and determines the number of crests and troughs along the circle's circumference. The parameters r_0 and a are calculated so that the final curve has a certain area and perimeter. Although the parameter n can be chosen freely, for all geometrically realizable (s, l) pairs, there is always a minimum order for which the Rose curve can be configured to have the desired area and perimeter. In other words, by increasing the order and tuning the parameters, a Rose curve with arbitrary perimeter and confined within the unit cell can be generated. Fig.6.2 shows a typical topology for the Rose curve inclusion.

A zeroth order Rose curve and a Rose curve with $a = 0$ are simply a circle. Therefore, the Rose curve at most can cover $\frac{\pi}{4} \simeq 78.5\%$ of the unit cell area, and it cannot be used for design of inclusions which requires area larger than 78.5% of the unit cell area (i.e., $F > 0.7854$).

The area, $Ar[R_n(r_0, a)]$, and perimeter, $Pr[R_n(r_0, a)]$, of the nth order Rose curve can be calculated using the following relations:

$$Ar[R_n] = \pi r_0^2 + \frac{\pi a^2}{2} \tag{6.7}$$

$$Pr[R_n] = \frac{2}{\kappa} \int_{\frac{h}{2}}^{\pi} \sqrt{1 + \eta_1 \cos n\varphi + \eta_2 \cos 2n\varphi} \; d\varphi \tag{6.8}$$

where

$$\kappa = (2r_0^2 + a^2(1 + n^2))^{-\frac{1}{2}}$$
$$\eta_1 = 2r_0 a\kappa^2$$
$$\eta_2 = \kappa^2 a^2(1 - n^2)$$

65
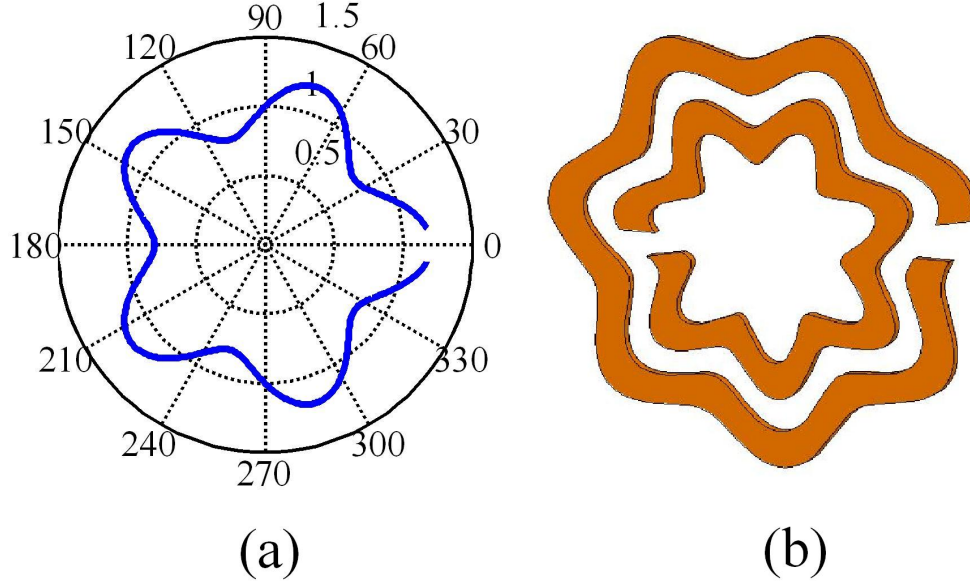
Figure 6.2: (a) A 5th order Rose curve with $r_0 = 1, a = 0.2$, (b) An edge-coupled inclusion designed using a 7th order Rose curve.

Next, I design a Rose curve to achieve the design requirements stated in (6.5). Table.6.1 presents the radius r_0 and the amplitude a of the Rose curves which is generated for different values of n ranging from 3 to 9. The last column in Table.6.1, parameter D, gives the diameter of the circle circumscribing the Rose curve. This parameter is useful to check if the Rose curve fits within the unit cell.

From Table.6.1, for the the Rose curve with $n = 3, 4$ and 5, D is larger than the unit cell size and therefore, the curve cannot fit within the unit cell since $20mm < D$. Even the 6th order Rose curve is not a good candidate for the case under consideration because if one considers the trace width of the inclusion with $n = 6$, the circumscribing circle has a diameter of $D + 0.4mm = 20.00mm$, implying the overlap of adjacent curves. Therefore, the Rose curve with $n = 7, 8$ and 9 are appropriate solutions. Rose curve with $n > 9$ presents the possibility of inter-element coupling which was not considered in the circuit model describing the AMM. Numerical analysis is performed with a full-wave three dimensional electromagnetic commercial software. [1].

---

[1]The effective parameters of the medium is determined from the physical quantities of in the propagation of the field, i.e., the reflection coefficient $S11$ and the transmission coefficient $S12$. The S-parameters have been simulated with Ansoft HFSS. Then, by use of a software application, the

Table 6.1: A Set of Candidates for Rose-Curved Inclusions

n	$r_0(mm)$	$a(mm)$	$D(mm)$
3	7.63	3.58	22.42
4	7.80	2.70	21.00
5	7.89	2.17	20.12
6	7.95	1.81	19.60
7	8.00	1.56	19.12
8	8.02	1.36	18.72
9	8.03	1.21	18.46

Fig.6.3 shows the analytically and numerically calculated permeability functions of media with inclusions introduced with Rose curves of $n = 7, 8$ and 9. The analytical response was generated using the circuit model and thus all the curves (for all the orders considered here) are expected to be identical. The numerical results were obtained using full-wave simulation using periodic boundary conditions to account for periodically positioned inclusions.

Note that the AMM is designed to work at the frequency of $600MHz$ with $2MHz$ bandwidth. Despite the fact that there is a slight shift in the resonance frequency or the maximum magnitude of the permeability function, the graphs show a robust design satisfying the design criteria. For instance, for the case of $n = 7$, the numerical simulation shows $\mu_{Re} = 9 \pm 5.6\%$ at the frequency of $599.5MHz$ with $2MHz$ bandwidth. The shift in frequency from the desired magnetic property requested in Table.5.1 is about 0.08%. The achieved MLT is 0.048 which is also within the desired range.

6.1.1 Parametric Study

Moreover, for a comprehensive study of the nth order Rose curve resonators (n-RCRs) a set of parametric study is performed. The parametric studies are to verify the general theory developed in chapter 2 and 3 on limitations and performance of inclusions and examine the potential application and general characteristics of n-RCRs.

HFSS results have been converted to desired parameters based on the extraction formula available in the literature [73], [74]. For the detail on the derivation please see Appendix C.
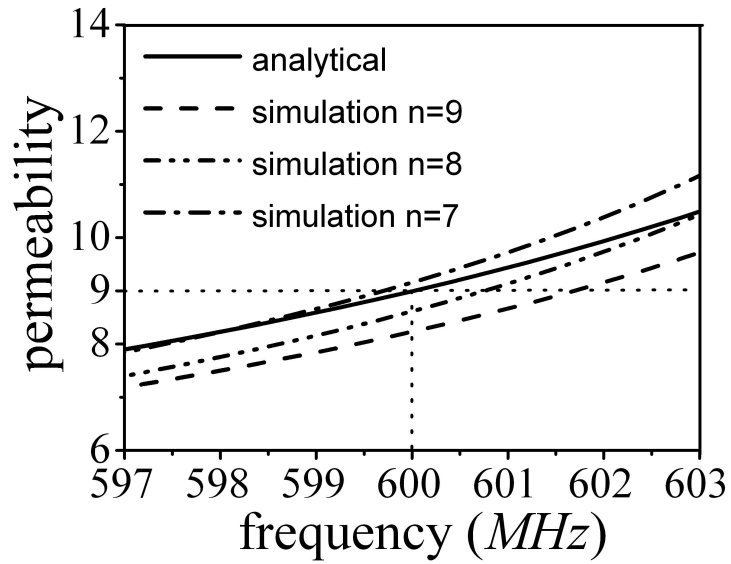
Figure 6.3: The dashed lines shows the simulated permeability function of the medium for n =7, 8 and 9. The solid line shows the analytically calculated permeability function of the medium for $n = 7, 8$ and 9. The plots of analytical solutions cannot be distinguished because they are identical.

Parametric studies are carried out on the effect of area and perimeters on the magnetic response of the same order Rose curves. Fig.6.4 shows the numerical analysis of 7th order Rose curve inclusions with similar surface area, equal to the half of the unit cell area and different perimeters. It is observed that inclusions with larger perimeter resonates at lower frequencies and thus, they provide a larger miniaturization factor,
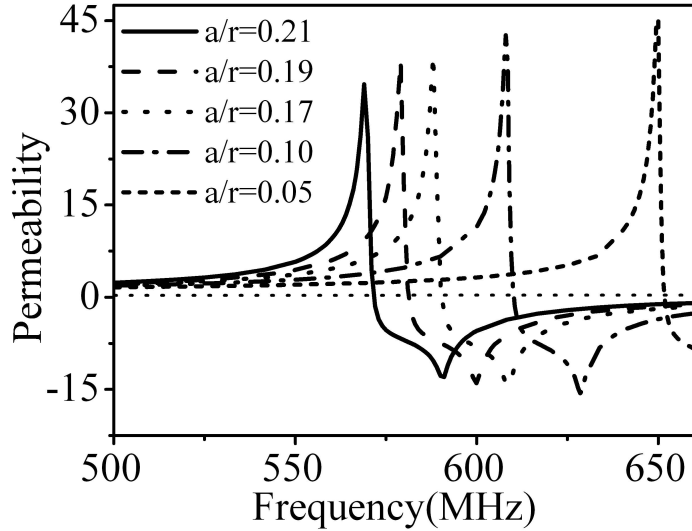
Figure 6.4: The real permeability of inclusions which occupied half of unit cell area and vary in length. (b) The real permeability of inclusions which encompasses different areas with the same trace length.

referred to as $\mathcal{M}$-factor[2] , for certain applications.

In addition, Fig.6.5 shows the numerical analysis of 7th order Rose curve inclusion with equal perimeter and different areas. The areas vary from 30% to 70% of the unit cell area. Increase in the area size leading to more flux penetration throughout the inclusions, and higher inductance. Thus, the resonance frequency is shifted down

---

[2]Miniaturization factor or $\mathcal{M}$-factor is defined as:

$$\mathcal{M}_{\text{factor}} = \frac{\lambda_0}{\ell} \tag{6.9}$$

where λ is the wavelength of an electromagnetic wave in free space, and ℓ is the form factor, feature size or the larger dimension of the structure or a unit cell of a structure.

The miniaturization is referred to two different meanings, 1) The ratio of the wavelength to the unit cell size of an AMM, This definition is useful to express the size of a unit cell of an engineered structure with respect to the radiation wavelength. Indeed, it expresses the validity of HT describing a composite medium and also the quasi-static nature of a model. 2) The ratio of the form factor or device dimension with respect to the radiation wavelength for the fabrication purposes and comparing the compactness of electronics and microwave devices.
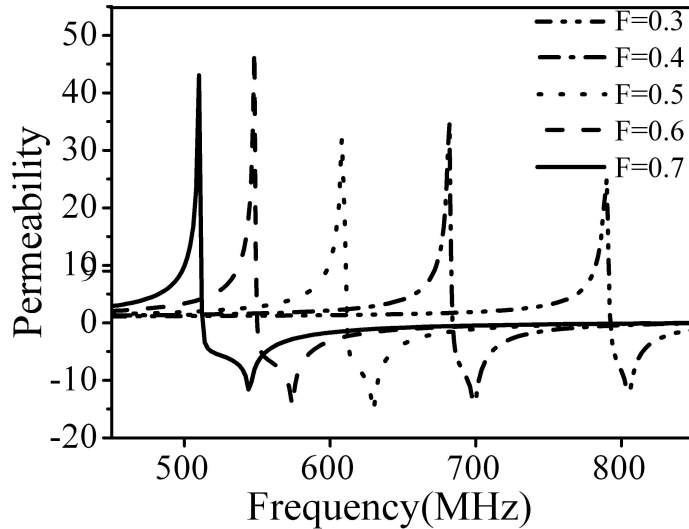
Figure 6.5: The real permeability of inclusions which encompasses different areas with the same trace length.

the spectrum and the larger-area inclusions provide a higher $\mathcal{M}$-factor.

Although two scenarios, increasing the area (perimeter) and keeping the perimeter (area) constant, leads to enhance in the $\mathcal{M}$-factor, a careful observation shows that increase in the perimeter creates a higher level of dispersion in the medium and a higher value of permeability whereas the other change generates a flatter permeability function and a lower permeability maximum value in the AMM. These observation has been predicated by the proposed model and limitations in chapters 3 and 4.

Note that near the resonance the real part of the effective permeability can be negative if the quality factor of the resonator is enough high. Another attractive feature of the proposed Rose curves is widening of the frequency bandwidth over which the medium provides negative permeability with minimized dispersion by increasing the order of RCRs. Simulations shows that the frequency bandwidth is about 2 times widened. The comparison was made for two cases of a medium composed of third order RCRs and a medium composed of seventeenth order RCRs.

In addition, the effect of curvature of the RCRs on the resonance frequency is studied. The curvature of inclusions introduces a new coupling in forms of capacitive

and inductive effect. Redefining the formulation of the magnetic response of an AMM by adding the curvature effect is a laborious task, and could be a topic of future work. I study the effect of the curvature of RCR inclusions. I compare the resonance frequency for different media composed of inclusions having identical perimeter (isoperimetric) and area (equiareal) but different curvatures. For this investigation, I define a new dimensionless measure in form of a curvature integral as:

$$\Lambda = \int \kappa^2(\theta) d\lambda \tag{6.10}$$

where $d\lambda$ is the length element and $\kappa(\theta)$ is the curvature function of the RCR normalized to the total length of the contour, defined in a polar coordinate as:

$$\kappa(\theta) = \frac{1}{Pr(\Gamma)} \frac{r^2 + 2r_\theta^2 - r_\theta r_{\theta\theta}}{(r^2 + r_\theta^2)^{\frac{3}{2}}} \tag{6.11}$$

where r_θ and $r_{\theta\theta}$ are the first and the second derivatives of $r(\theta)$, respectively.

For characterizing the effect of curvature, I considered an inclusion with structural and fabrication specifications summarized in Table 5.1. The inclusion's metallic trace follows Rose curve functions of the order $n = 3$ to $n = 50$ over the angle $\theta \in [h_n, 2\pi - h_n]$, where h_n varies for different n to keep the slit width on the inclusions equal $1mm$. The slit behaves as a capacitor in an inclusion's circuit model. In this study, inclusions' area and perimeter are kept $160mm^2$ and $60mm$, respectively.

In Fig.6.6-a, the integral curvature factor $\Lambda(n)$ is plotted versus the order of the Rose curve,n. The plot shows a linear increase in the curvature of the Rose curve. Thus, it can be considered as a proper parametrization of the curvature effect on the magnetic response. Fig.6.6-b shows the graph of resonance frequency versus the parameter Λ. In spite of the fact that the curvature does not provide a hight impact on the resonance frequency, but it shows a minimum value for a certain curvature.

6.2 The kth order Corrugated Rectangular Resonators, $C_k^i(a, h)$

The next candidate for inclusions's geometry is a square or a rectangle with corrugated sides. The corrugations are a square wave added to one side or two parallel sides of
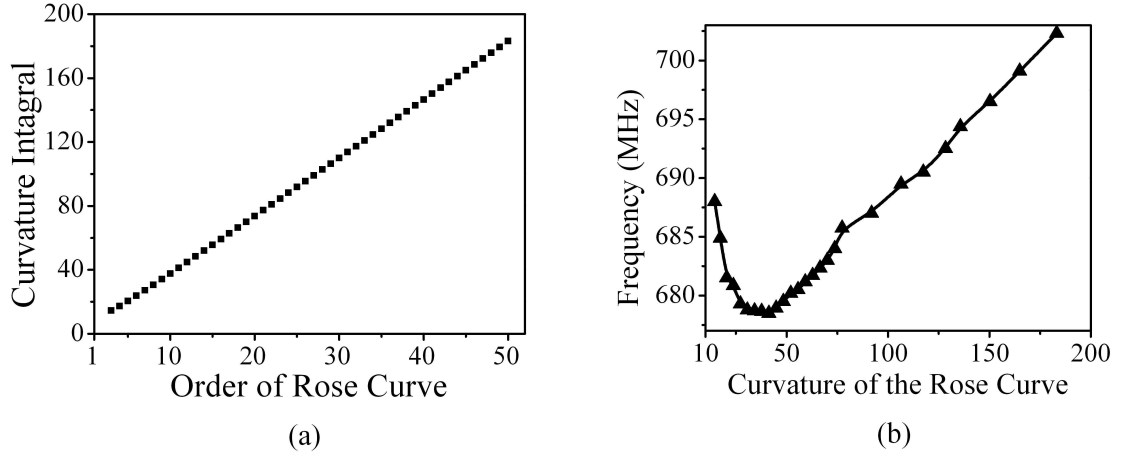
Figure 6.6: (a) The curvature integral function of the $n = 3$ to 50 has been plotted. The graph shows a linear relation between the order of the curve and its curvature integral. (b) The resonance frequency of AMMs composed of Rose curve inclusions with equal area and perimeter but different order has been plotted versus the curvature integral of the inclusions.

the base square shape. The pattern is called Corrugated rectangle and plotted in Fig.6.7. The figure shows Corrugated rectangular curve of the order $k = 0, 1$ and 2 over one side and two sides of a square.

The area of the final contour can be approximated as the area of the base square; however, the perimeter reaches a desired value by choosing the right order of the corrugation, i.e., the frequency of grooves and the amplitude of the added square wave. The area and the perimeter of the kth order Corrugated rectangular curves are calculated as

1. *One-sided Corrugated Rectangle, $C_k^1(a, h)$*

$$Ar[C_k^1] = (2k+1)^2 a^2 - kah \tag{6.12}$$
$$Pr[C_k^1] = 4(2k+1)a + (2k)h \tag{6.13}$$

2. *Two-sided Corrugated Rectangle, $C_k^2(a, h)$*

$$Ar[C_k^2] = (2k+1)^2 a^2 - 2kah \tag{6.14}$$
$$Pr[C_k^2] = 4(2k+1)a + 2(2k)h \tag{6.15}$$
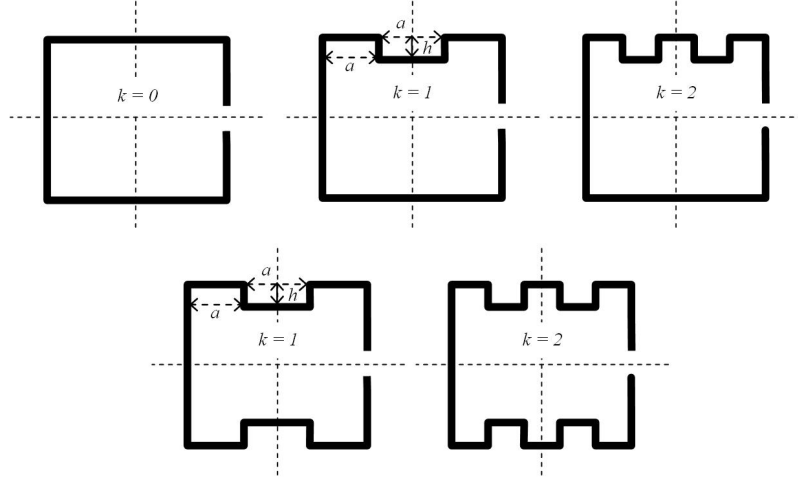
Figure 6.7: Corrugated rectangular curve of the order $k = 0, 1$ and 2. The upper figures are curves with the corrugation on one side, and lower figures are curve with the corrugation on two sides.

Note that the length of the inclusion's slits needs to be included in the final inclusion's length. Also, $L = (2k+1)a$, the length of enclosing square of the contour, has to be smaller than the unit cell length, and $h < L$ for one side corrugation and $2h < L$ for two sides corrugation. Solving for a, we obtain:

$$a = \frac{Pr}{\gamma_1} \left(1 + \sqrt{1 + 4\gamma_1 \frac{Ar}{Pr^2}} \right) \tag{6.16}$$

where $\gamma_1 = 4(2k+1)(2k+3)$; and h can be obtained from (6.12) and (6.14) for the one-sided or two-sided Corrugated rectangular inclusions, respectively, as:

$$h_1 = \frac{Pr}{\gamma_2} \left(1 + \sqrt{1 + 4\gamma \frac{Ar}{Pr^2}} \right) - \frac{Ar}{ka} \tag{6.17}$$

$$h_2 = \frac{h_1}{2} \tag{6.18}$$

where $\gamma_2 = \frac{2k+1}{4k(2k+3)}$.

It can be shown that for a given k, the maximum perimeter is $6(2k+1)a$. So, by increasing k any perimeter values is achievable. As the base curve of the Corrugated

Table 6.2: A Set of Candidates for one-sided Corrugated rectangular inclusions

k	$a(mm)$	$h(mm)$	$L(mm)$
1	4.94	3.70	14.81
2	2.92	2.06	14.60
3	2.07	1.45	14.50
4	1.60	1.12	14.43
5	1.31	0.91	14.39
6	1.10	0.77	14.36
7	0.96	0.66	14.34
8	0.84	0.59	14.32

rectangular curve is a square (i.e., where $a = 0$ or $k = 0$), the minimum possible perimeter is $Pr^2 \geq 16Ar$. Thus, by calculating k, a and h, any arbitrary (s, l) pair that satisfies the square inequality can be constructed. However, in practical applications, the corrugations width cannot be very small due coupling effects that might not be accounted for by the circuit model.

The hight and the frequency of grooves in a one-sided Corrugated rectangular curve is calculated for the area and perimeter pair given in (6.5). The results of the calculation for the Corrugated rectangular curves of the first to the sixth order were summarized in Table.6.2. The curves are confined within the unit cell area and realizable because $h < L < \delta x$.

The first, second and third order Corrugated rectangular inclusions were simulated. The simulated and the analytical result were plotted in Fig.6.8. The simulation of the AMM composed of the first order Corrugated rectangular curve shows the effective permeability equal to 9 at the central frequency of $600.9 MHz$. The shift from the desired magnetic property requested in Table.5.1 is about 0.15%. From the simulation, the frequency bandwidth for $\pm 5\%$ deviation from the central permeability is about $1.9 MHz$, and the magnetic loss tangent is less than 0.041.

Note that for the higher order curves (6, 7 and 8), if one considers the inclusion's trace width b, the grooves walls become so close that they create unpredicted capacitive coupling which was not considered in the circuit model.
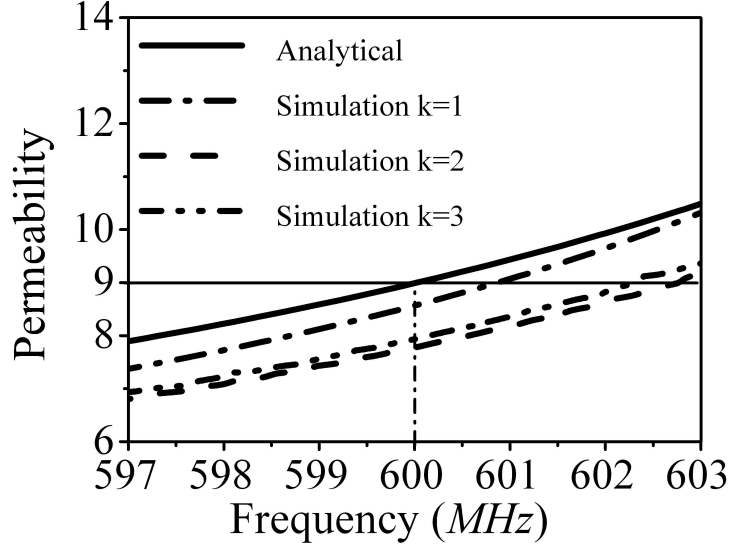
Figure 6.8: The dashed lines shows the simulated permeability function of the medium for $k = 1, 2$ and 3. The solid line shows the analytically calculated permeability function of the medium for $k = 1, 2$ and 3. The plots of analytical solutions cannot be distinguished because they are identical.

6.3 The mth order Sine Oval Resonators, $S_m(b, a_j)$

The Rose curve and the Corrugated rectangular curve have limitations. The Rose curve cannot cover the whole area of the unit cell as it has a circular base, and the Corrugated rectangular curve cannot approach the Dido's inequality [71] as it has a rectangular base. An ideal curve needs to be reconfigured to a circle for approaching Dido's inequality and to a square for covering the unit cell area. A curve that can accomplish such properties is an mth order Sine oval curve. The curve is parameterized with θ in a Cartesian coordinate system, and expressed in a vectorial form denoted by the vector $\overrightarrow{\Gamma}(x(\theta), z(\theta))$, where the components x and z are stated as

$$S_m(\beta, \alpha_j) : \theta \to \overrightarrow{\Gamma}(x, z); \quad 0 \le j \le m$$

$$\begin{cases} x(\theta) = \beta \cos(\theta) \\ z(\theta) = \alpha_0 \sin(\alpha_1 \sin(...(\alpha_{m-1} \sin(\alpha_m \sin(\theta)))...)) \end{cases} \tag{6.19}$$

The parameter θ sweeps the curve in the $xz - plane$ aside from a small slit of width h in radians; thus, $\theta \in [\frac{h}{2}, 2\pi - \frac{h}{2}]$. β and α_i are positive real numbers. A set of conditions limit the α_i parameters so that the area covered by the generated curve is simply connected. For $0 < \theta < \pi$, $z(\theta)$ should be positive in order to avoid curves with self-crossing points. For instance, considering $\theta = \pi/2$ and $m = 1$, we get $z(\pi/2) = \alpha_0 \sin(\alpha_1)$; thus, $\alpha_1 < \pi$. (The study of these conditions will not be considered here).

From (6.19), it can be shown that the zeroth order Sine oval curve with $\beta = \alpha_0 = r$ is a circle with a radius of r. However, by increasing the order m and keeping $\beta = \alpha_0 = d$ and $\alpha_1 = ... = \alpha_m = \frac{\pi}{2}$, the curve approaches a square shape with sides equal to d. The key advantage of this parametric shape is that by configuring the parameters and the order of the curve, all realizable geometries possessing a pair of (s, l), ranging from a circle to a square, can be generated. Moreover, for a certain configuration, the shape provides the minimal curvature function. Therefore, the effect of unpredicted coupling due to adjacent traces would be less than previous topologies considered in this work. Fig.6.9 shows sample shapes of the Sine oval curve.

To explicitly determine the mth order Sine oval curve, $(m + 2)$ parameters need to be calculated. one can focus on two equations expressing the area and perimeter:

$$Ar[S_m] = 2 \int_0^\pi z(\theta) x_\theta(\theta) d\theta = -2\beta \int_0^\pi z \sin \theta d\theta \tag{6.20}$$

$$Pr[S_m] = 2 \int_{\frac{h}{2}}^\pi |\overrightarrow{\Gamma}_\theta| d\theta = 2 \int_{\frac{h}{2}}^\pi \sqrt{z_\theta^2 + \beta^2 \sin^2 \theta} d\theta \tag{6.21}$$

where x_θ, z_θ and $\overrightarrow{\Gamma}_\theta$ are derivatives of $x(\theta)$, $z(\theta)$ and $\overrightarrow{\Gamma}(x, z)$ with respect to θ, respectively. The number of unknowns parameters exceeds the number of equations. Therefore, the number of unknowns needs to be reduced in order to solve the equations
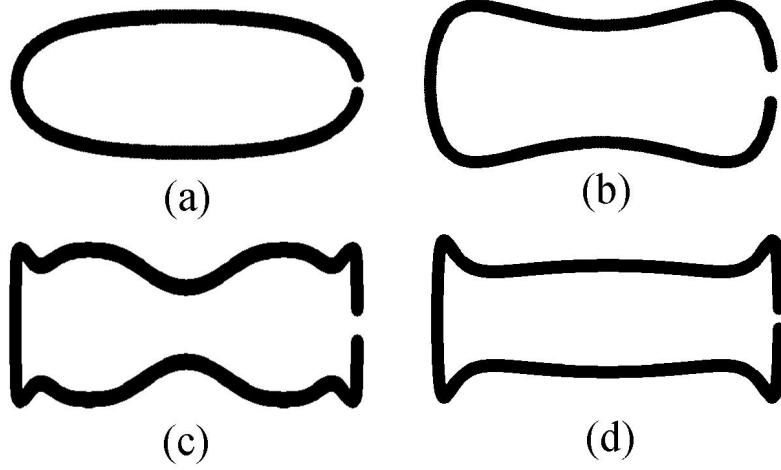
Figure 6.9: Samples of the Sine oval curve, (a) $m = 0, \beta = 1, \alpha_0 = 0.5$, (b) $m = 1, \beta = \alpha_0 = 1 \alpha_1 = 2.5$, (c) $m = 3, \beta = 1 \alpha_0 = \alpha_1 - 1 = \alpha_2 - 2 = \alpha_3 - 2.5 = 0.5$, (d) $m = 4, \beta = \alpha_0 = \alpha_3 = \alpha_4 = 1, \alpha_1 = \alpha_2 = 2.5$.

(6.20) and (6.21). one should enforce the condition $\beta = \alpha_0$, $\alpha_j = \pi/2$ for $1 \leq j \leq m-1$ and $\alpha = \alpha_m$. The first condition confines the inclusions within a box with sides of β, and they never cross the unit cell boundaries. It can be shown that the second condition makes the inclusions smoother at the edges, and with a single trough. Thus, the mth order Sine oval function reduces to

$$\begin{cases} x(\theta) = \beta \cos(\theta) \\ z(\theta) = \beta \sin(\varsigma_m(\theta)) \end{cases} \tag{6.22}$$

where

$$\varsigma_m(\theta) = \underbrace{\frac{\pi}{2} \sin(...(\frac{\pi}{2} \sin(\alpha \sin(\theta)))...)}_{m} \text{ for } m \geq 1, \text{ and } \varsigma_0(\theta) = \theta.$$

The area and the perimeter of mth order Sine oval curve formulated in (6.22) are expressed as:

$$Ar[S_m] = -2\beta^2 \int_0^\pi \sin\theta \cos(\varsigma_m(\theta)) d\theta \tag{6.23}$$

$$Pr[S_m] = 2\beta \int_{\frac{h}{2}}^\pi (\sin^2\theta + \alpha \left(\frac{\pi}{2}\right)^{m-1} \prod_{i=0}^m \cos^2(\varsigma_i(\theta)))^{\frac{1}{2}} d\theta \tag{6.24}$$

77

Table 6.3: A Set of Candidates for Sine oval inclusions

m	$\beta(mm)$	$\alpha(mm)$
1	8.50	2.61
2	8.20	2.81
3	8.09	2.94
4	8.10	3.02
5	8.21	3.07
6	8.40	3.10
7	7.93	3.11
8	8.16	3.12

For the pair expressed in (6.5), the parameters α and β are calculated for $m = 1$ to 8. The results were summarized in Table.6.3. For the zeroth order Sine oval curve, the curve reduces to a circle with the radius equal to β; therefore, there is no zeroth order Sine oval curve that holds the specified area and perimeter. Fig.6.10 shows simulation results in comparison with the analytical result. For the first order Sine oval curve, the permeability is 9 at the frequency of $600.5MHz$ which corresponds to about 0.08% shifts in frequency for the desired magnetic response expressed in Table.5.1. From the simulation, the frequency bandwidth for $\pm 5\%$ deviation over the central frequency of $600MHz$ is about $2.0MHz$, and the magnetic loss tangent is less than 0.043.

6.4 Discussion

As a summary, comparing the proposed geometries, the nth order Rose curve and k^{th} order Corrugated rectangular curve are easier to configure with respect to the mth order Sine oval curve. However, the Sine oval curve can be designed so that it provides minimal curvature function and thus less unpredicted capacitive coupling, leading to better matching between the designed and desired AMM for even higher order of the curve. For example, the results simulated for the design of the pair in (6.5) shows that the Sine oval curve provides better agreement with the desired magnetic response[3].

---

[3]It is perceivable that the Sine oval Curves can be designed to provide minimum curvature integral while possessing fixed area and perimeter, however, it is laborious task to characterize the
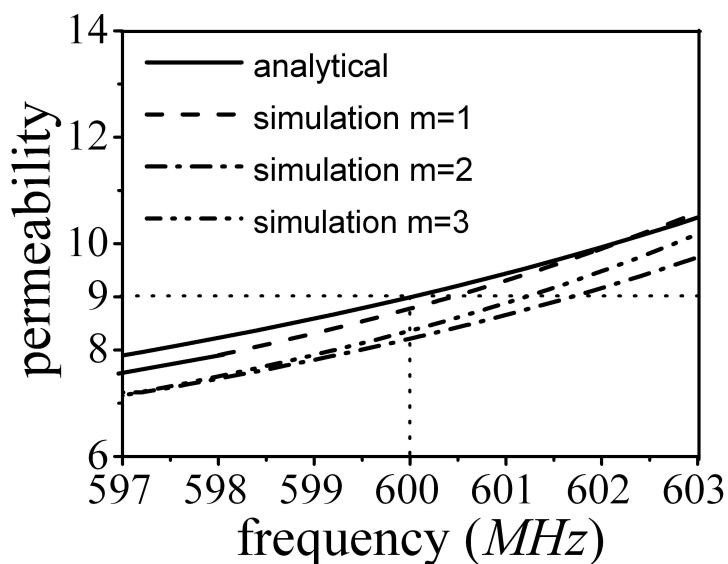
Figure 6.10: The dashed lines shows the simulated permeability function of the medium for $m =1$, 2 and 3. The solid line shows the analytically calculated permeability function of the medium for $m = 1, 2$ and 3. The plots of analytical solutions cannot be distinguished because they are identical.

For designing inclusions with area larger than 78.5% of the unit cell area, the Rose curve cannot be a candidate as it is basically a circular shape. Also, the Corrugated rectangular curve cannot be a candidate for an inclusion with the area and perimeter follows the relation $l^2 < 16s$. However, the Sine oval curve allows for design of any geometrically realizable (s, l) pair circumscribed within the unit cell area.

An important question is: Are these the only curves can be offered as a generic inclusion? if not, what else is available and how they can be generated? Definitely, there are other curves that can be realize specific area and perimeter. However, there are several points which needs to be considered for proposing a new inclusion's

Sine oval curve for such an objective. The study of characterizing curves, in general, which provide a minimum curvature integral with fixed area and perimeter has been performed by the author of this dissertation. To the best of my knowledge, no one has touched this problem with this broad objective. The new curve can also be used in design of ring resonators, which can be another subject of future work.

geometric family:

- ease of characterization for (s, l) pairs

- bijective for all realizable (s, l) pairs

- having uncorrelated area and perimeter functions

- can be compacted inside the unit cell

- provides minimum coupling

Rose curves satisfies options 1-3-4, Corrugated rectangular curves satisfies 1-3-4-5, and Sine oval curves satisfies 2-3-4-5.

6.5   Contribution

I introduced three sets of novel geometries for the inclusions topologies in order to realize AMMs with desirable magnetic properties. The introduced curves are tunable to achieve any (s, l) pair calculated through the design methodology. The geometries are the nth order Rose curve, k^{th} order Corrugated rectangular curve and m^{th} order Sine oval curve. The new inclusion topologies were used to design an AMM meeting specific criteria. Strong agreement was realized between the analytical results and the numerical simulations testifying to the robustness of the design methodology and flexibility and capability of the new geometries.

In addition, in parametric study, I investigated the potentials of Rose curve resonators as a generic candidate for AMMs. The study includes the effect of variation of the area with a fixed perimeter, variation of the perimeter with a fixed area. the effect of integral curvature on the resonance frequency of RCRs.

In addition, a Matlab software code has been developed to automatically characterize Rose curve, Corrugated rectangular curve and Sine oval Curve. The code receives the area and perimeter of a generic curve and produces a set of possible curves that possess the same area and perimeter of an input. The code also has an option of considering the length of gap in the contour and calculate the proper length of the metallic trace. In fact, the output is in a form of data set corresponding

to the parameters of Rose curve, corrugated rectangular curve and Sine oval curve. Moreover, the code inversely can receive the parameters of the Rose curve, corrugated rectangular curve and Sine oval curve and calculate the area and perimeter of the corresponding figure. In addition, this code can be linked to the code developed for design of AMMs and create a full package for design of AMMs meeting desired magnetic properties. The code has been presented in Appendix D for academic usage.

Chapter 7

Applications

The limitations, techniques and several families of inclusions introduced in previous chapters are general and can be applied to any application. However, in this chapter, I use the Rose curve inclusions in two important applications:

- Designing a highly miniaturized stop-band filter using complimentary Rose curve inclusions

- Miniaturizing a patch antenna using a slab of AMM composed of Rose curve inclusions

In the first application, the Rose curve inclusions are etched off from the ground plane to create complementary Rose curve resonators (CRCRs). CRCRs are electrically coupled to signal line to implement an ultra miniaturized stop-band microstrip filter.

The second application is a microstrip antenna being loaded with an AMM slab used as a substrate. The AMM substrate is exploited to miniaturize the size of the antenna. Such miniaturized antenna can have critical applications in narrow-bandwidth sensor networks.

7.1 A Small-Form Microstrip Stop-band Filter

Various techniques have been addressed in order to miniaturize planar microwave components. Traditionally, semi-lumped capacitors, inductors and resonators were

used for the design of microwave filters [75]. Recently, the use of electrically-small looped resonators was proposed as an alternative approach to achieve a high degree of miniaturization. In the resonant-type approach, the loading elements are complementary split ring resonators (CSRRs) [76]-[77], or complimentary spiral ring resonators (CS-RRs) [78].

The concept of complementary resonators was primarily introduced to realize resonant-based metamaterials exhibiting negative permittivity rather than permeability [79]. In fact, complementary resonator counterparts are achieved by etching the ring resonator geometry out from a metallic sheet. As the complementary ring resonators are electromagnetically dual of the ring resonators by virtue of Babinet's principle, the normal electric field to the metallic sheet excites the resonators, Thus, if complementary ring resonators are used for the ground plane of a microstrip stop-band filter, just underneath the conductor strip, they are excited and electrically coupled to the microstrip line, increases the equivalent capacitance of the structure, and consequently reduces the electrical size of the filter [77]. In addition, by invoking the duality analysis, the resonance frequency of both loop resonators and complementary resonators are *approximately* the same (some exact formulas for resonance frequency of complementary resonators can be found in [80]. Hence, the quasi-static design formula provided in chapter 3 can be used to design complementary resonators.

Several complementary resonators topologies such as complementary split ring resonators (CSRR) and complementary spiral ring resonators (CS-RR) have been used to design miniaturized filter with novel functionalities. This approach is widely addressed in the literature [81], [38] and [3]. It has been shown that CS-RR structures present more miniaturization than CSRR, and also CS-RR with higher number of turns provides a larger $\mathcal{M}$-factor. However, increasing the number of turns reduces the effective area inside the resonators and compromises the further miniaturization. Although the use of rectangular CS-RR can resolve this issue to some extent, it is still limited.

Complementary Rose Curve resonators (CRCRs) are etched from the ground plate, under the signal strip, of a microstrip stop-band filter to miniaturize the filter's dimension. Newly introduced Rose curve resonators (RCRs) are applied to enhance the $\mathcal{M}$-factor. The new complementary resonator has a higher potential for miniaturization. The miniaturization is defined as the ratio of the wavelength at which
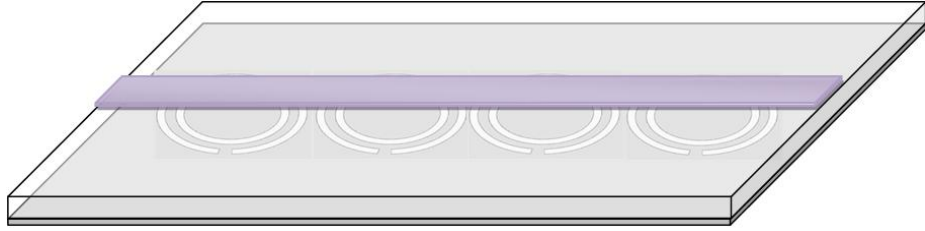
Figure 7.1: The design schematic of a stop-band microstrip transmission line based on complimentary split ring resonators.

the complementary inclusions resonate to the length of the signal strip in the filter device. Over an identical surface area occupied by the resonator, a RCR can possess more length with respect to its counterparts. Thus, CRCRs present higher equivalent capacitance and larger reduction in the electrical size of the filter. In theory, by increasing the parameters in the Rose curve parametric equation, a higher $\mathcal{M}$-factor can be obtained. However, practically, the design dimensions are limited to the fabrication technology.

7.1.1   Design and Simulation

To demonstrate the performance and compactness of the proposed stop-band filter based on CRCRs, a prototype device with four inclusions of two types is designed and simulated, and then the miniaturization factors is compared. The commercially available Rogers RO3010 ($\epsilon_r = 10.2$) is employed for the substrate. The full-wave simulator Computer Simulation Technology (CST) studio suite 2009 is used to implement the simulation setup. The setup for microstrip stop-band filter design with CSRR and CRCR are demonstrated in Fig.7.1 and Fig.7.2 , respectively. The thickness of the substrate is $1.27mm = 200mil$. The width of the strip line is chosen to be $1.2mm$ to maintain a characteristic impedance of 50Ω.

The resonance frequency of the complementary resonators are designed to be about $2.5GHz$. For circular ring resonators, this resonance frequency can be achieved by split ring resonators of radius $2.25mm$ and $2.85mm$ and the trace width of $0.3mm$ [57]. The area and perimeter corresponded to this structure is $20.43mm^2$ and $16.02mm$, respectively. For the Rose curve resonators, as it has been previously discussed, the
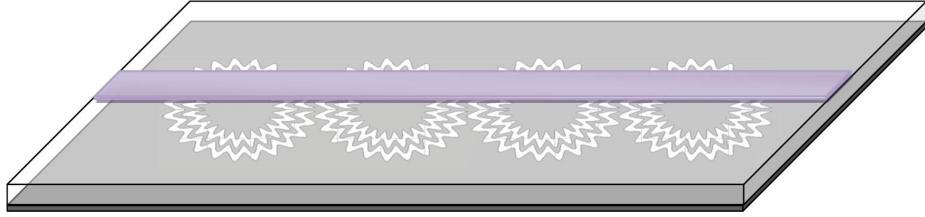
Figure 7.2: The design schematic of a stop-band microstrip transmission line based on complimentary Rose curve resonators.

resonance frequency is approximately proportional to the multiplication of the area and perimeter values. Hence, to keep the resonance frequency and increasing $\mathcal{M}$-factor, The area of the inclusions are decreased while keeping the multiplication of area and perimeter constant by increasing the perimeter correspondingly. Therefore, the Rose curve parameters, i.e., the radius of the base circle r_0 and the amplitude of the cosine function a can be calculated for different order n of the rose curve. Apparently, higher order provides more miniaturization. The filter has been designed for $n = 13$ and $n = 23$. Note that the trace width was kept $0.3mm$ for CRCRs.

The transfer function has been plotted for all cases in Fig.7.3 and Fig.7.4. It should be emphasized that the total length occupied by the CSRRs is 28 mm. Hence, compared to the signal wavelength at resonance ($45mm$), the $\mathcal{M}$-factor is $45mm/28mm = 1.6$. However, for the 13th order CRCRs the total device length is about $14mm$. Hence, the new design is three times smaller than the microstrip filter with plain ground plate. Also, the $\mathcal{M}$-factor for the 35th order CRCRs is about 4 corresponding to the device length of $11mm$. Note that the bandwidth of the filter is significantly reduced in a filter designed with a CRCRs ground plane with respect to a filter designed with a CSRRs ground plane. A suggestion to resolve the discrepancy in the frequency band-stop can be by breaking the symmetry in design such as reorient CRCRs in different angles with respect to normal axis to the ground plane or slightly resizing the inclusions to cover different but close resonance frequency in CRCRs.
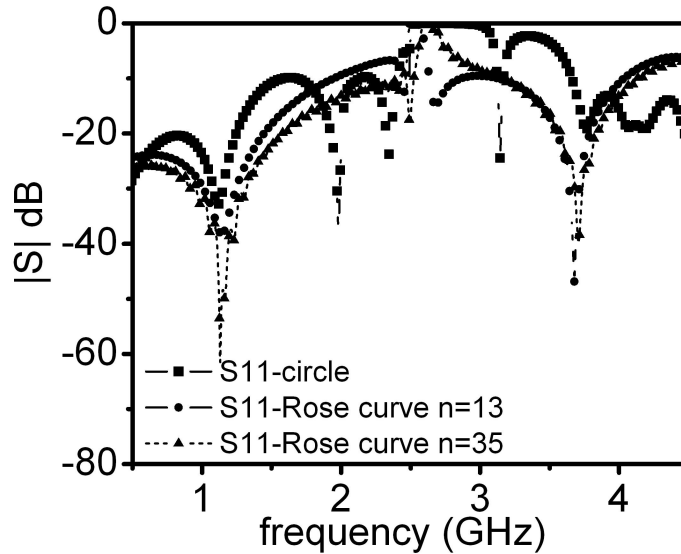
Figure 7.3: Simulated $S11$ parameters for the four-period ground plane in microstrip filter technology based on complementary resonators.

7.2 A Super-Miniaturized Low Profile Antenna

Shrinking the size, simplifying the interface and encapsulating the multi-functionality in wireless hand-held devices are of the highest priority in the communications industry. This kind of demand is very challenging for antenna designers because the smaller the devices are, the smaller the antennas should be. Of course, the smaller size antennas should retain their capability to fulfill the ever shrinking system requirements. For example, wide bandwidth and high performance are demanding parameters in the antenna design. Recently, an influx of research has been devoted to antenna miniaturization using AMMs [50], [51], [82]-[85]. AMMs seem to allow mobile-phone manufacturers to reduce the size of antennas (e.g., the planar inverted F-antennas, PIFAs) and accordingly handsets while maintaining good performance at low cost.

In this section, the performance of a patch antenna while lying on an AMM substrate is analyzed. The important question is: what are the substrate parameters while achieving desired antenna performance after size reduction? Let consider a

86
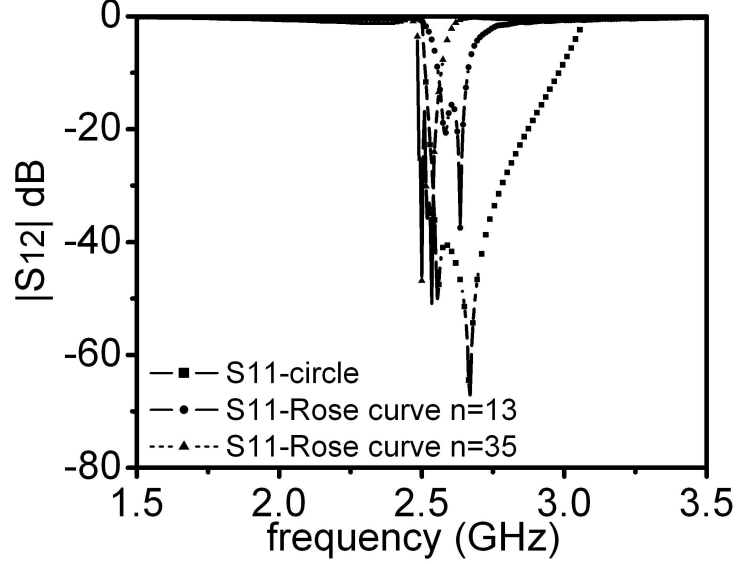
Figure 7.4: Simulated $S21$ parameters for the four-period ground plane in microstrip filter technology based on complementary resonators.

half-wavelength resonant patch antenna operating at an angular frequency ω_{op}. One can determine desire properties of the substrate, and then, design the substrate with the proposed design methodology. The size of the antenna ℓ_a is proportional to the wavelength in the substrate:

$$\ell_a \propto \lambda = \frac{\lambda_0}{\sqrt{\epsilon_{\text{eff}}\mu_{\text{eff}}}} \tag{7.1}$$

where λ_0 is the wavelength of the radiation in the free space, and ϵ_{eff} and μ_{eff} are the relative permittivity and permeability of the substrate. Increasing the effective medium parameters results in antenna size reduction. However, when the antenna is miniaturized using high permittivity dielectric, the antenna suffers from significant reduction in bandwidth and deterioration in the impedance matching [86]-[92]. Therefore, alternatively, for miniaturizing the size of the antenna, one can use magneto-dielectric materials ($\epsilon_{\text{eff}} > 1, \mu_{\text{eff}} > 1$) or high permeability material for substrate. This hypothesis has been examined by using a transmission-line analysis, and it was

87
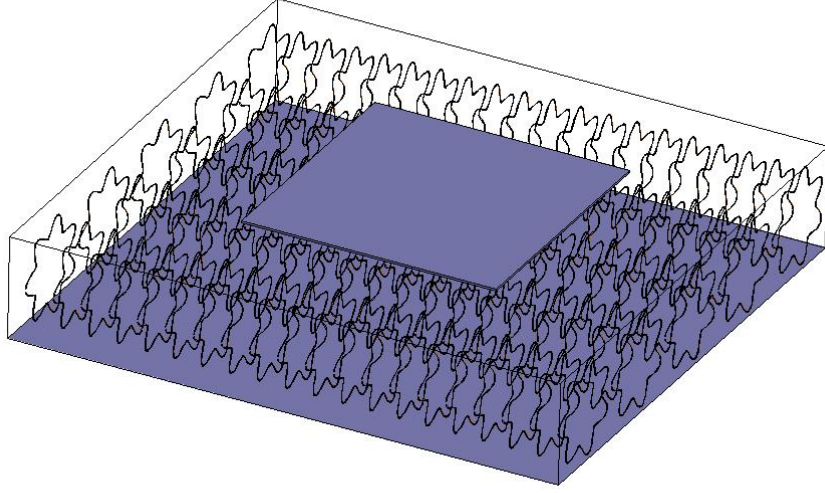
Figure 7.5: A schematic of a coaxial-fed patch antenna lying over an AMM composed of Rose curve inclusions.

verified that a substrate with $\mu_{\text{eff}} \gg \epsilon_{\text{eff}}$ and $\mu_{\text{eff}} \gg 1$ retains the antenna bandwidth and radiation quality factor after miniaturization [85], [93]. An approximate formula for the impedance bandwidth of a probe-fed patch antenna over a AMM substrate with the thickness d is given by [85]:

$$BW = \frac{96d\sqrt{\frac{\mu_{\text{eff}}}{\epsilon_{\text{eff}}}}}{\left(4\sqrt{2} + 17\sqrt{2\mu_{\text{eff}}\epsilon_{\text{eff}}}\right)\lambda_0} \tag{7.2}$$

A resonant patch antenna which is mounted on a magneto-dielectric substrate is designed to work at $600MHz$. The substrate is an AMM slab composed of Rose curve inclusions (see Fig.7.5). To check the performance of the antenna, I used a pre-designed AMM. The AMM was designed to provide $\mu_{\text{eff}} = 9 \pm 5\%$ over a frequency bandwidth of $2MHz$ and with an MLT of less than 0.05 (see chapters (5) and (6) for design procedure). Fig.7.6 shows the real effective permeability and permittivity of the designed AMM, and the electric and magnetic loss tangent in the slab medium. Moreover, Fig.7.7 shows the real and imaginary part of the refractive index and intrinsic impedance of the substrate slab. The values of effective parameters
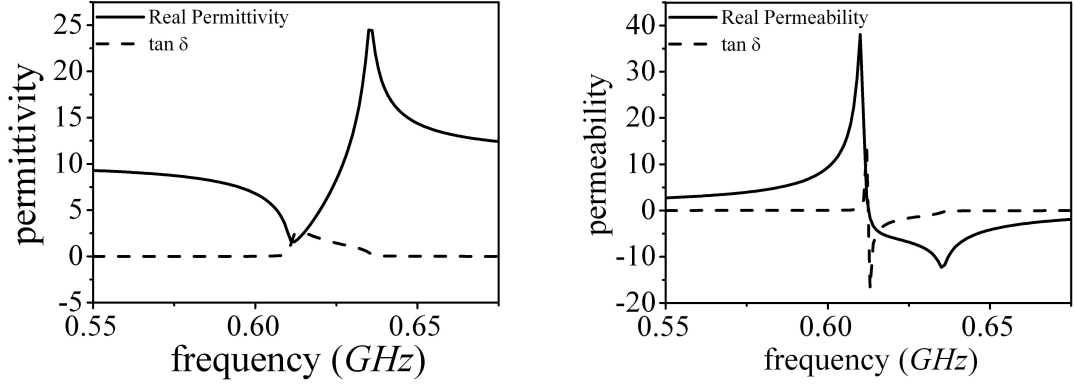
Figure 7.6: The left graph shows the permittivity and electric loss tangent function of the substrate composed of ose curve inclusions. The right graph shows the permeability and magnetic loss tangent of the substrate composed of ose curve inclusions.

at $600MHz$ are summarized in Table. 7.1. Indeed, the refractive index corresponds to the $\mathcal{M}$-factor.

To simulate the antenna setup and extract the operating parameters of antenna a full-wave antenna simulator is used. However, due to the large feature size ratio between the antenna and the AMM, a large amount of inclusions is needed to fill up the substrate. Thus, embedding the metallic inclusions in the design setup consumes a huge, and practically inefficient, resources for simulation. As a consequence, the simulation is alternatively done with a homogeneous, yet anisotropic, substrate with permittivity and permeability functions defined based on the AMM electromagnetic characteristics extracted through separate plane wave analysis.

The simulation results are compared with similar patch antenna designs with substrates composed of various AMM's inclusions' geometry. The new antenna is designed to operate at the frequency of $600MHz$. The schematic of the designed

Table 7.1: The effective parameters of designed AMM for an antenna substrate at $600MHz$.

$\epsilon_{\text{eff Re}}$	$\tan \delta_\epsilon$	μ_{effRe}	$\tan \delta_\mu$	n_{eff}	z_{eff}
6.795	9.50×10^{-3}	9.322	4.03×10^{-2}	$7.961 + j0.123$	$1.171 - j0.0292$
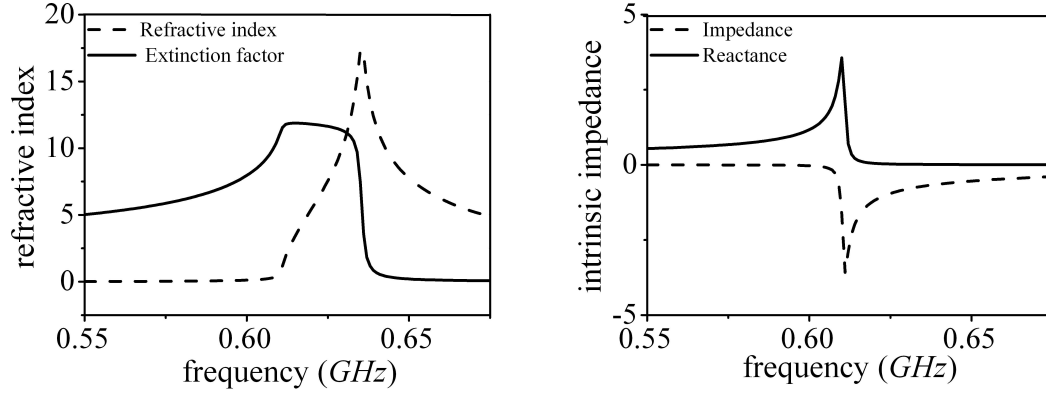
Figure 7.7: The left graph shows the refractive index and the extinction factor function of the substrate composed of ose curve inclusions. The right graph shows the real and imaginary part of the intrinsic impedance the substrate composed of ose curve inclusions.

structure is demonstrated in Fig.7.8. The simulated $S11$ is presented in Fig.7.9, and it shows a relative bandwidth ($S11 < -10dB$) of 0.67%. The bandwidth of the antenna is relatively low compared to other counterparts proposed in the literature, and is useful for narrow band antenna applications such as sensor applications. The radiation pattern is plotted in 2D and 3D in Fig.7.10 and Fig.7.11 . The numerical calculations show a maximum gain of $1.5dBi$ at the boresight with the front-to-back ratio of $4.4dB$ and 59% radiation efficiency for the miniaturized antenna. According to the design dimensions, the size of antenna in the y direction is equal to $L_y = 2.86cm$ which is 1/17.4 of $\lambda_0 = 50cm$, the wavelength at the resonance frequency of $600MHz$. Thus, a $\mathcal{M}$-factor of 8.7 is achieved using artificial magnetic substrate. The ground plane is taken at least twice of the patch size in each side to avoid restriction of the gain. For completeness, a comparison of different experiment and simulation reported in the literature summarized is in Table. 7.2.
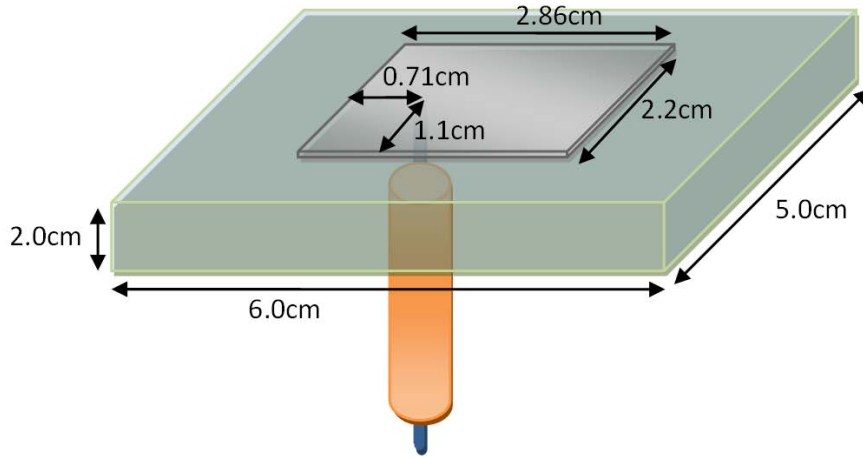
Figure 7.8: The design schematic of a coaxial-fed microstrip patch antenna.

7.3 Contribution

I examined the performance of a newly introduced n^{th} order Rose curve resonators in two key applications. The first application is a design of ultra miniaturized microstrip stop-band filter with complementary Rose curve resonators as a ground plane. The complimentary resonators' response to the electric field is in accordance with the Babinet's principle. The simulation results shows a controllable miniaturization potential for RCRs. The $\mathcal{M}$-factor can be controlled by the parameters of RCRS. Particularly, the higher order resonators make the higher miniaturizing effect due to the increase in the length of the etched trace from the ground plane. My observation shows that miniaturized devices provide narrower bandwidth, and they are limited to special applications.

Next, I tested the effect of RCRs as a constituent of the substrate on the performance of a patch antenna. Numerical simulation shows that maintaining the gain and radiation efficiency of the antenna within an acceptable range in the process of miniaturizing the antenna size is only compensated by the impedance bandwidth of the antenna. Therefore, the miniaturized antenna can suitably be exploited in sensing applications.

In general, I showed that Rose curve Resonators as a generic inclusions geometry
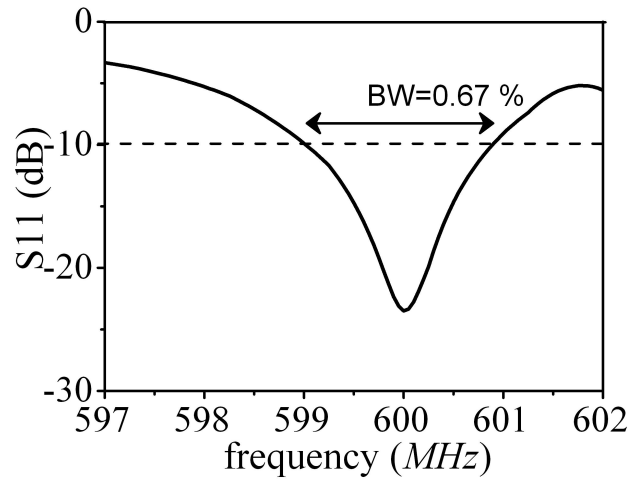
Figure 7.9: Simulated return loss of a miniaturized patch antenna.

can be uniquely reconfigured for many applications. In addition, I believe that the
Corrugated rectangular resonators and Sine oval resonators at least are able to exhibit
the same potential in different applications. It is due to the fact that they can
theoretically be tuned for many desired magnetic responses. The investigation of
their potential is a matter of future work.
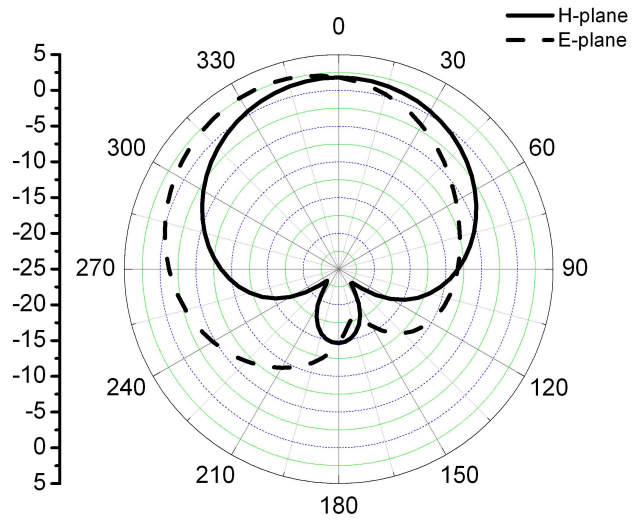
Figure 7.10: Simulated 2-D radiation pattern of a miniaturized patch antenna.
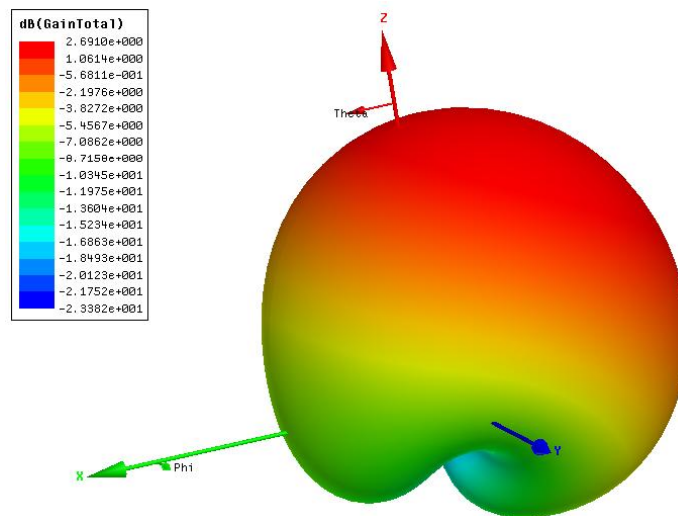
Figure 7.11: Simulated 3-D radiation pattern of a miniaturized patch antenna.

Table 7.2: Comparison table of different miniaturized antenna designs. sim=simulation results, mes=measurment results, filling=a typical AMM dispersion function.

Source	inclusion	$f_{res}MHz$	Gain	BW	Efficiency	$\mathcal{M}_{\text{factor}}$	sim/mes
[94]	Hilbert	615MHz	-3.4dB	2.1%	50%	5.8	mes
[95]	Metasolenoid	860MHz	-	1.3%	70%	1.2	mes
[96]	CSRR	3.0GHz	1.3dB	3.3%	-	1.4	sim
[96]	CSRR	2.5GHz	-0.5dB	3.2%	-	1.5	mes
[51]	Spiral	250MHz	-3.9dB	0.8%	20%	6.5	mes
[97]	filling	1.58GHz	-	6.0%	89%	1.3	sim
[98]	Using EBG	2.4GHz	5.2dB	-	90%	1.3	mes
Thesis	Rose curve	600MHz	1.5dB	0.6%	59%	8.4	sim

Chapter 8

Afterword

8.1 Summary

Several advances have been added to the existing field of metamaterials under the branch of artificial magnetic materials (AMMs). The advances include capturing fundamental limitations of the performance of AMMs and developing a design procedure and introducing inclusions for generic applications.

In the field of metamaterials, many attempts have been made towards enhancing the properties of composite media. Every day, new designs of AMM promise new advantages. However, they mostly do not seek a target, and they are designed based on the designer's passion towards proposing new geometrical configurations. Henceforth, with the set of fundamental limitations on 1) the dispersion characteristics of the permeability function, 2) the minimum achievable magnetic loss tangent through the medium, and 3) the maximum permeability attainable through geometrical manipulation, designers can define a set of design goals to approach, rather than having a random design and running everlasting optimization processes blindly. Note that the limitations are valid within linear metamaterials and at the microwave level, where the quasi-static approach for describing the composite medium is applicable. However, the range of validity encompasses many applications such as antenna miniaturization, filter design, and low profile gain enhancement, among others, using AMMs. The approach to derive the limitation is based on a common material model available in the literature [1], [12], [99].

In addition, based on a new formulation for AMMs composed of generic inclusions, a set of propositions for the effect of geometrical changes was presented. For instance, an increase in area of an inclusion increases the effective permeability of the medium, but unfortunately also leads to increased dispersion. The propositions are essentially used as design guidelines for AMMs.

Next, applying the design propositions, a general, methodical approach for the design of microwave AMMs composed of metallic broken loop resonators was outlined. The methodology was embodied based on a circuit model. The strategy, however, is general and can be adopted with other full-fledged circuit models to increase the accuracy of the design. Due to the fact that inclusions are much smaller than the electromagnetic radiation wavelength, an AMM can fully be described through an accurate RLC circuit. The design procedure was abridged in four steps, namely checking the design feasibility, calculation of the resonance frequency of an inclusion and the geometrical and physical parameter introduced in the model, modifying the parameters through iterations and calculating the area and, finally, metallic race length to fulfil the desired magnetic properties.

The outcome of the design methodology is the area and perimeter, (s, l) pair, of AMM's constituent. There are an infinite number of curves that possess a fixed area and perimeters. I introduced three families of reconfigurable geometries with the possibility of embedding in the unit cell and providing a minimum curvature integral. The introduced inclusions are the nth order Rose curve resonator (a circle added with a sinusoidal function), the kth order Corrugated rectangular resonators (a rectangle with corrugations) and the mth order Sine oval resonators. The former inclusion was studied in detail to check its potential characteristics, including being a generic inclusion for designing AMMs meeting desired magnetic properties, controllable miniaturization factor, and controllable bandwidth in which the permeability is negative.

Finally, to practically verify the features of the Rose curves, they were exploited in two crucial applications. The first application was using the complementary Rose curve resonators in design of ground plane for a small-form microstrip stop-band filter. The next application was using an AMM composed of Rose curve resonators in design of a substrate for ultra miniaturized low profile antennas.

8.2 Contributions

In this dissertation the following contributions were reported:

- A new formulation for describing artificial magnetic materials composed of parallel arrays of generic inclusion with a unique geometry has been derived.

- A new set of parameters (geometrical and physical) in the formulation of artificial magnetic materials has been introduced.

- A fundamental limitation for the minimum achievable dispersion over a specific frequency bandwidth has been derived.

- All effects of the geometrical and physical parameters on the performance of artificial magnetic materials have been reported. The report is used as design guidelines for AMM engineers.

- A design recipe based on a generic circuit model for design of an artificial magnetic material fulfilling desired specifications has been developed. The strategy used in the design recipe can also be applied to other circuit models.

- A software code for automating the AMM design has been implemented.

- The nth order Rose curve resonator as a generic family of inclusions with promising characteristics has been introduced.

- The kth order Corrugated rectangular resonators as a generic inclusion for designing an AMM has been introduced.

- The mth order Sine oval resonators as another generic inclusion for designing an AMM has been introduced.

- The effect of curvature integral of the inclusion's geometry on the performance of constructed AMM has been studied.

- A small-form microstrip stop-band filter based on complementary Rose curve resonators has been designed.

- A highly miniaturized patch antenna with an AMM substrate composed of the Rose curve resonators has been designed.

8.3   Future Prospect

Followings are some possible future works:

Reformulating and adopting other circuit models for developing design recipes:
Other circuit models available in the literature can be adopted by the defined strategy to develop a more accurate design recipe for AMMs.

Formulating a circuit model for describing the electric behavior of AMMs:
AMMs show bianisotropy. Therefore, providing a general circuit model for the permittivity function of an AMM with generic inclusions is a crucial task.

Developing an AMM's design recipe with desired magnetodielectric properties:
This problem can be solved by reformulating the permittivity function in terms of the geometrical and physical parameters of the medium. Therefore, a methodology can be developed to address the magnetic and electric properties, i.e., the permeability, permittivity and electric and magnetic tangent loss of the medium, simultaneously.

Parametric Study of Corrugated rectangular resonators:
The same parametric study can be performed for investigating the performance of the Corrugated rectangular resonators.

Parametric Study of Sine oval resonators:
The same parametric study can be performed for investigating the performance of the Sine oval resonators.

Studying the effect of inclusions on the performance of AMMs:
A circuit model can be developed to incorporate the inclusions' curvature function. The main advantage of this formulation is an increase in the accuracy of the model and design process.

Characterizing inclusion's geometry with a minimum curvature integral:
Controlling the curvature integral of an inclusion's geometry advances the design accuracy because the neglected capacitive and inductive coupling factors would be less effective. The design accuracy would then be enhanced.

Developing new applications of introduced inclusions:

The introduced inclusions can be used in many applications such as antenna miniaturization and sensitivity enhancement of near-field probes. The generic property of the inclusions made them suitable for any application that employ AMMs in their structure.

Fabrication of proposed structures:

An important future work is the fabrication and experimental characterization of the introduced inclusions. Moreover, two applications introduced in chapter 7 need to be experimentally verified.

Bibliography

[1] J. B. Penury, A. J. Holden, D. J. Robbins, and W. J. Stewart. Magnetism from conductors and enhanced nonlinear phenomena. *IEEE Transactions on Microwave Theory and Techniques*, 47(11):2075–2084, November 1999. 2, 10, 11, 13, 16, 25, 27, 35, 41, 95

[2] S. Maslovski, P. Ikonen, I. Kolmakov, and S. Tretyakov. Artificial magnetic materials based on the new magnetic particle: Metasolenoid. *Progress In Electromagnetics Research*, 54(9):61–81, September 2005. 10, 12, 13, 16, 17, 18, 19, 25, 35, 41

[3] J. D. Baena, J. Bonache, F. Martin, R. Marques, F. Falcone, T. Lopetegi, M. A. Laso, J. Garcia-Garcia I. Gil, and M. Sorolla. Equivalent circuit models for split ring resonators and complementary split rings resonators coupled to planar transmission lines. *EEE Transactions on Microwave Theory and Techniques*, 53:1451–1461, 2005. 83

[4] H. Mosallaei and K. Sarabandi. Design and modeling of patch antenna printed on magneto-dielectric embedded-circuit metasubstrate. *IEEE Transaction on Antenna and Propagation*, 55:4552, January 2007. 2

[5] S. B. Narang and I. S. Hudiara. Microwave dielectric properties of m-type barium, calcium and strontium hexaferrite substituted with co and ti. *Journal of Ceramic Processing Research*, 7(2):113116, 2006. 6

[6] W. D. Callister. *Materials science and engineering, an introduction*. John Wiley and Sons Inc, 2000. 6

[7] Laszlo Solymar and Ekaterina Shamonina. *Waves in Metamaterials*. Oxford University Press, Great Britain, 2009. 6

[8] W. Lamb, D. M. Wood, and N. W. Ashcroft. Long-wavelength electromagnetic propagation in heterogeneous media. *Physical Review B*, 21(6):2248–2266, March 1980. 6

[9] D. Rousselle, A. Berthault, O. Acher, J. P. Bouchaud, and P. G. Zerah. Effective medium at finite frequency: Theory and experiment. *Journal of Applied Physics*, 74(1):475–480, July 1993. 6

[10] L D Landau, L. P. Pitaevskii, and E.M. Lifshitz. *Electrodynamics of Continuous Media*, volume 8. Pergamon Press, second edition, 2004. 7, 20, 119

[11] John David Jackson. *Classical Electrodynamics*. John Wiley and Sons Inc, University of California, Berkeley, third edition, 1925. 7, 18, 26

[12] D. R. Smith, W. J. Padilla, D. C. Vier, S. Nemat-Nasser, and S. Schultz. Composite medium with simultaneously negative permeability and permittivity. *Physical Review Letters*, 84(18):4184–4187, 2000. 8, 27, 95

[13] D. R. Smith, W. J. Padilla, D. C. Vier, R. Shelby, S. C. Nemat-Nasser, N. Kroll, and S. Schultz. *Photonic Crystals and Light Localization in the 21st Century*, chapter Left-handed metamaterials, pages 351–371. Kluwer Academic Publishers, 2001. 8

[14] V. G. Keelage. The electrodynamics of substances with simultaneously negative values of ϵ and μ. *Soviet Physics - Unspent*, 10(4):509–514, January 1968. 8

[15] David R. Smith and Norman Kroll. Negative refractive index in left-handed materials. *Physical Review Letters*, 85(14):2934–2936, May 2000. 8

[16] A. F. Starr, P. M. Rye, D. R. Smith, and S. Nemat-Nasser. Fabrication and characterization of a negative-refractive-index composite metamaterial. *Physical Review B*, 70:113102,1–4, September 2004. 8

[17] A. L. Pokrovsky and A. L. Efros. Sign of refractive index and group velocity in left-handed media. *Solid State Commun*, 124(8):283–187, 2002. 8

[18] J. M. Williams and J. Pendry. Some problems with negative refraction. *Physics Review Letters*, 87(24):249703/1,249704/1, 2001. 8

[19] R. A. Shelby and D. R. Smith. Experimental verification of a negative index of refraction. *Science*, 292(5514):77–79, 2001. 8

[20] R. B. Greegor, C. G. Parazzoli, K. Li, B. E .C. Koltenbah, and M. Tanielian. Experimental determination and numerical simulation of the properties of negative index of refraction materials. *Optics Express*, 11:688–695, April 2003. 8

[21] J.B. Pendry. Negative refraction makes a perfect lens. *Physical Review Letters*, 85(18):3966–3969, 2000. 8

[22] N.N. Wan, D. Huang, Q. Cheng, W.X. Jiang, R. Liu, and T.J. Cui. Study of active superlens and evanescent wave amplification using an active metamaterial model. *Europe Physics Journal of Applied Physics*, 48(2):21101/1–6, November 2009. 8

[23] Bogdan-Ioan Popa and Steven A. Cummer. Direct measurement of evanescent wave enhancement inside passive metamaterials. *Physical Review E*, 73:016617/1–5, January 2006. 8

[24] K. B. Tan, C. H. Liang, T. Su, and B. Wu. Evanescent wave amplification in meta-materials. *Journal of Electromagnetic Waves and Applications*, 22(10):1318–1325, 2008. 8

[25] Hyesog Lee, Yi Xiong, Nicholas Fang, Werayut Srituravanich, Stephane Durant, Muralidhar Ambati, Cheng Sun, and Xiang Zhang. Realization of optical superlens imaging below the diffraction limit. *New Journal of Physics*, 7(255):1–16, August 2005. 8

[26] Nicholas Fang and Xiang Zhang. Imaging properties of a metamaterial superlens. *Applied Physics Letters*, 82(2):161–182, January 2003. 8

[27] Stefan Linden, Christian Enkrich, Martin Wegener, Jiangfeng Zhou, Thomas Koschny, and Costas M. Soukoulis. Magnetic response of metamaterials at 100 terahertz. *science*, 306:1351–1353, 2004. 10, 55

[28] N. Katsarakis, T. Koschny, M. Kafesaki, E. N. Economy, and C. M. Soukoulis. Electric coupling to the magnetic resonance of split ring resonators. *Applied Physics Letters*, 84(15):2943–2945, April 2004. 10

[29] Andrey K. Sarychev, Gennady Shvets, and Vladimir M. Shalaev. Magnetic plasmonic resonance. *Physical Review E*, 73:036609/1–10, March 2006. 10, 55

[30] Stefan Linden, Christian Enkrich, Gunnar Dolling, and Costas M Soukoulis. Photonic metamaterila: Magnetism at optical frequencies. *IEEE Journal of Selected Topics in Quantum Electronics*, 12(6):1097–1105, November 2006.

[31] Veladimir M Shalaev. Optical negative-index metamaterials. *Nature*, 1:41–48, 2007. 10

[32] Sergei Alexander Shelkunoff and Harald T. Antennas Friis. *Antennas: Theory and Practice.* John Wiley, 1952. 10

[33] W. N. Hardy and L. A. Whitehead. Split-ring resonator for use in magnetic resonance from 200-2000 mhz. *Review Science, Instrum*, 52(2):213–216, February 1981. 10

[34] M. V. Kostin and V. V. Shevchenko. Theory of artificial magnetic substances based on ring currents. *Journal of Communications Technology and Electronics*, 38(5):72–83, 1993. 10

[35] M. V. Kostin and V. V. Shevchenko. Artificial magnetics based on double circular elements. In *the proceeding of bian-isotropics 94, perigueux*, pages 49–56, May 1994. 10

[36] R. Marques, F. Medina, and R. Rafii-El-Idrissi. Role of bianisotropy in negative permeability and left-handed metamaterials. *Physical Review B (Condensed Matter and Materials Physics)*, 65(144440/1):144440/6, April 2002. 10, 11, 12, 58

[37] L. Yousefi and O. M. Ramahi. New artificial magnetic materials based on fractal hilbert curves. *in the Proceeding of IWAT07*, pages 237–240, March 2007. 11, 12, 35

[38] J. D. Baena, R. Marques, F. Medina, and J. Martel. Artificial magnetic metamaterial design by using spiral resonators. *Physical Review B (Condensed Matter and Materials Physics)*, 69(1):141–145, January 2004. 10, 11, 13, 83

[39] L. Zhou, W Wen, C. T. Chan, and P. Sheng. Multiband subwavelength magnetic reflectors based on fractals. *Journal of Applied Physics Letters*, 83(16):3257–3259, 2003. 11

[40] R. W. Ziolkowski and A. Erentok. Metamaterial-based efficient electrically small antennas. *IEEE Transaction of Antenna and Propagation*, 54:2113–2130, July 2006.

[41] V. Crnojevic-Bengin, V. Radonic, and B. Jokanovic. Fractal geometries of complementary split-ring resonators. *2312-2321*, 56(10):2312 – 2321, October 2008.

[42] E. Lenz and H. Henke. Homogenization of metamaterials due to fractaloid structures in the microwave regime. *Journal of Optics A: Pure and Applied Optics*, 11(11):114021, October 2009.

[43] X. Huang, Shiyi Xiao, Jiangtao Huangfu Dexin Ye, Zhiyu Wang, Lixin Ran, and Lei Zhou. Fractal plasmonic metamaterials for subwavelength imaging. *Journal of Optics Express*, 18(10):10377–10387, May 2010. 11

[44] B. Sauviac, C. R. Siovski, and S. A. Tretyakov. Double spli-ring resonators: Analytical modeling and numerical simulation. *Electromagnetics*, 24(5):317–338, February 2004. 11, 12, 18, 40

[45] A. Ishimaru, S. Lee, Y. Kuga, and V. Jandhyala. Generalized constitutive relations for metamaterials based on the quasi-static lorentz theory. *IEEE Transaction on Antenna and Propagation*, 51(10):2550–2557, October 2003. 11

[46] D. R. Smith and J. B. Pendry. Homogenization of metamaterials by field averaging. *Journal of Optic Society of America B*, 23(3):391–403, March 2006. 11

[47] M. G. Silveirinha. Metamaterial homogenization approach with application to the characterization of microstructured composites with negative parameters. 75:115104/1–15, March 2007. 11

[48] M. Shamonin, E. Shamonina, V. Kalinin, and L. Solymar. Properties of a metamaterial element: Analytical solutions and numerical simulations for a singly split double ring. *Journal of Applied Physics*, 95(57):3778–3784, 2004. 12

[49] P. Ikonen and S. A. Tretyakov. Determination of generalized permeability function and field energy density in artificial magnetics using the equivalent-circuit method. *IEEE Transaction of Antenna and Propagation*, 55(1):92–99, 2007. 12, 21, 40

[50] P. Ikonen, S. I. Maslovski, C. R. Simovski, and S. A. Tretyakov. On artificial magnetodielectric loading for improving the impedance bandwidth properties of microstrip antennas. *IEEE Transaction on Antenna and Propagation*, 54(6):1654–1662, June 2006. 12, 25, 86

[51] K. Buell, H. Mosallaei, and K. Sarabandi. A substrate for small patch antennas providing tunable miniaturization factors. *IEEE TRansaction on Microwave and Technology*, 54:135–146, January 2006. 12, 16, 86, 94

[52] M. Boybay and O. M. Ramahi. Near-field probes using double and single negative media. In *In proceedings of NATO Advanced Research Workshop: Metamaterials for Secure Information and Communication Technologies*, volume 1B, pages 725–731, May 2008. 12

[53] G. Lovat and P. Burghignoli. Shielding Effectiveness of a Metamaterial Slab. In *the proceeding of IEEE International Symposium of Electromagnetic Compatibility*, volume 1B, pages 1–5, July 2007. 12

[54] N. I. Landy, S. Sajuyigbe, J. J. Mock, D. R. Smith, and W. J.Padillal. Perfect metamaterial absorber. *Physical Review Letters, volume =*.

[55] F. Bilotti, A. Alu', N. Engheta, and L. Vegni. Features of a metamaterial based microwave absorber. In *in proceedings of the workshop on metamaterials and*

special materials for electromagnetic applications and TLC, volume 1B, pages 11–14, Roma, Italia, March 2006. 12

[56] Steven A. Cummer, Bogdan-Ioan Popa, and Thomas H. Hand. Q-based design equations and loss limits for resonant metamaterials and experimental validation. *IEEE Transaction on Antenna and Propagation*, 56(1):127–132, January 2008. 12, 42

[57] R. Marques, F. Mesa, J. Martel, , and F. Medina. Comparative analysis of edge- and broadside-coupled split ring resonators for metamaterial design. theory and experiments. *IEEE Transacion of Antennas and Propagation*, 51:25722581, October 2003. 13, 14, 84

[58] K. Buell and K. Sarabandi. A method for characterizing complex permittivity and permeability of meta-materials. In *In Proceedings of Antanna and Propagation Symposium*, volume 2, pages 408–411, June 2002. 13

[59] J. D. Baena, L. Jelinek, and R. Marqus. Towards a systematic design of isotropic bulk magnetic metamaterials using the cubic point groups of symmetry. *Physical Review B*, 76:245115/1–14, December 2007. 15

[60] S. Anantha Ramakrishna. Physics of negative refractive index materials. *Report progress in physics*, 68:449–521, January 2005. 15, 16

[61] P. Gay-Balmaz and O. J. F. Martin. Efficient isotropic magnetic resonators. *Applied Physics Letters*, 81(5):939–941, 2001. 15

[62] Y. T. Lo and W. Lee. *Antenna Handbook: Theory, Application, and Design*. Number Chapter 7. Van Nostrand Reinold Co., New York, 1988. 18

[63] R. Schinzinger and P. Laura. *Conformal mapping: methods and applications*. Elsevier, 1991. 18

[64] Ian B Mitchell. The kramers-kronig relations. Online, University of Tennessee, March 2008. 26

[65] Robert G. Brown. Classical electrodynamics-part ii. Online, Duke University Physics Department, 2007.

[66] K. E. Peiponen, V. Lucarini1, E. M. Vartiainen, and J. J. Saarinen. Kramers-kronig relations and sum rules of negative refractive index media. *The European Physical Journal B - Condensed Matter and Complex Systems*, 41(1):61–65, September 2004.

[67] Colin Warwick. Understanding the kramers-kronig relation using a pictorial proof. Online, Agilent Technologies, Inc., March 2010. 26

[68] H A Keramers. The dispersion and absorption of x-rays. *Physikalische Zeitschrift*, 30:522–523, 1929. 26

[69] R Kronig. On the theory of dispersion of x-rays. *Journal of Optical Society of America*, 12:547–757, 1926. 26

[70] O. M. Ramahi A.Kabiri, L. Yousefi. Limitations of artificial magnetic materials. *IEEE Transaction on Antenna and Propagation*. 42, 48

[71] Marvin J. Forray. *Variational Calculus in Science and Engineering*. McGraw Hill, 1968. 54, 75

[72] J. D. Baena, L. Jelinek, R. Marques, and M. Silveirinha. Unified homogenization theory for magnetoinductive and electromagnetic waves in split-ring metamaterials. *Phusical Review A*, 78:013842/1–5, July 2008. 57

[73] D. R. Smith, S. Schultz, P. Markos, and C. M. Soukoulis. Determination of effective permittivity and permeability of metamaterials from reflection and transmission coefficients. *Physical Review B*, 65:195104/1–5, April 2002. 67, 129

[74] Xudong Chen, Tomasz M. Grzegcrzyk, Bae-Jan Wue, Joe Pacheco, and Jin Au Kong. Robust methodto retrieve the constitutive effective parameters of meta-materials. *Physical Review E*, 70:016608/1–7, July 2004. 67, 129

[75] J. S. Hong and M. J. Lancaster. *Microstrip Filters for RF/Microwave Applications*. John Wiley and Sons Inc, New York, USA, 2001. 83

[76] Francisco Falcone, Txema Lopetegi, Juan D. Baena, Ricardo Marqus, Ferran Martn, and Mario Sorolla. Effective negative-ϵ stopband microstrip lines based

on complementary split ring resonators. *IEEE Microwave and Wireless components Letters*, 14(6):280–282, 2004 2004. 83

[77] J. Bonache, I. Gil, J. Garcia-Garcia, and F. Martin. Novel microstrip band pass filters based on complementary split rings resonators. *IEEE Transactions on Microwave Theory and Techniques*, 54:265–271, 2006. 83

[78] Jordi Selga, Gerard Siso, Marta Gil, Jordi Bonache, and Ferran Martn. Microwave cicuit miniaturization with complemenraty spiral resonators: Applicayion to high-pass filters and dual-band components. *Microwave and Optical Technology Letters*, 51(11):2741–2745, August 2009. 83

[79] F Falcone, T. Lopetegi, M. A. Laso, J. D. Baena, J. Bonache, R. Marques, F. Martin, and M. Sorolla. Babinet principle applied to the design of metasurfaces and metamaterials. *Physical Review Letters*, 93:197401/1–3, 2004. 83

[80] Ricardo Marqus, Ferran Martn, and Mario Sorolla. *Metamaterials with Negative Parameters: Theory, Design and Microwave Applications*. John Wiley and Sons Inc, 2007. 83

[81] J. Bonache, G. Siso, M. Gil, A. Iniesta, J. Garcia-Garcia, and F Martin. Application of composite right/left handed (crlh) transmission lines based on complementary split ring resonators (csrrs) to the design of dual-band microwave components. *IEEE Microwave and Wireless Components Letters*, 18:524–526, 2008. 83

[82] M. E. Ermutlu, C. R. Simovski, M. K. Krkkinen, P. Ikonen, S. A. Tretyakov, and A. A. Sochava. Miniaturization of patch antennas with new artificial magnetic layers. In *the proceeding of IEEE international workshop on antenna technology*, volume 1B, pages 87–90, March 2005. 86

[83] A. Foroozesh, and L. Shafai. Size reduction of a microstrip antenna with dielectric superstrate using meta-materials: artificial magnetic conductors versus magneto-dielectrics. In *the proceeding of IEEE International Symposium of Electromagnetic Compatibility*, volume 1B, pages 11–14, July 2006.

[84] M. Karkkainen and P. Ikonen. Patch antenna with stacked split-ring resonators as artificial magnetodielectric substrate. *Microwave and Optical Technology Letters*, 46(6):554–556, July 2005.

[85] R. C. Hansen and M. Burke. Antennas with magneto-dielectrics. *Microwave Optical Technology Letters*, 26(2):7578, 2000. 86, 88

[86] I. J. Bahl and P. Bhartia. *Microstrip antennas.* Artech House, Massachusettes, 1980. 87

[87] J. S. Colburn and Y. Rahmat-Samii. Patch antennas on externally perforated high dielectric constant substrates. *IEEE Transaction of Antennas and Propagation*, 47(12):17851794, 1999.

[88] K. R. Carver and J. W. Mink. Microstrip antenna technology. *IEEE Transaction of Antennas and Propagation*, AP29(1):224, 1981.

[89] R. K. Mongia, A. Ittipiboon, and M. Cuhaci. Low profile dielectric resonator antennas using a very high permittivity material. *Electronics Letters*, 30(17):13621363, 1994.

[90] Y. Hwang, Y. P. Zhang, G. X. Zheng, and T. K. C. Lo. Planar inverted f antenna loaded with high permittivity material. *Electronics Letters*, 31(20):17101712, 1995.

[91] D. R. Jackson and N. G. Alexopoulos. Simple approximate formulas for input resistance, bandwidth, and efficiency of a resonant rectangular patch. *IEEE Transaction of Antennas and Propagation*, 39(3):407409, 1991.

[92] C. A. Balanis. *Antenna theory: Analysis and design.* John Wiley and Sons Inc, New York, 1997. 87

[93] O. Edvardsson. On the influence of capacitive and inductive loading on different types of small patch / pifa structures for use on mobile phones. In *Proceeding of ICAP International Conference on Antennas and Propagation*, page 1720, Manchester, UK, April 2001. 88

[94] L. Yousfi and O. Ramahi. Miniaturized wideband antenna using engineered magnetic materials with multi-resonator inclusions. In *in the proceeding of Antennas and Propagation Society International Symposium*, pages 1885–1888, June 2007. 94

[95] P. Ikonen, S. Maslovski, and S. Tretyakov. Pifa loaded with artificial magnetic material: Practical example for two utilization strategies. *Microwave and Optical Technology Letters*, 46(3):205–210, June 2005. 94

[96] Yoonjae Lee and Yang Hao. Characterization of microstrip patch antennas on metamaterial substrates loaded with complementary split-ring resonators microwave and optical technology letters. *Microwave and Optical Technology Letters*, 50(8):2131–2135, August 2008. 94

[97] M. K. Karkkainen, S. A. Tretyakov, and P. Ikonen. Numerical study of pifa with dispersive material fillings. *Microwave and Optical Technology Letters*, 45(1):5–8, February 2005. 94

[98] E.G. Korkontzila, D.B. Papafilippou, and D.P. Chrissoulidis. Miniaturization of microstrip patch antenna for wireless applications by use of multilayered electromagnetic band gap substrate. In *IEEE Antenna and Propagation Symposium*, pages 1–6, November 2006. 94

[99] R. W. Ziolkowski. Design, fabrication, and testing of double negative metamaterials. *IEEE Transaction on Antenna and Propagation*, 51(7):1516 – 1529, July 2003. 95

[100] J. B. Pendry, A. J. Holden, Stewart, and Youngs. Extremely low frequency plasmons in metallic mesostructures. *Physical Review Letters*, 76(25):4773–4776, June 1996.

[101] M.S. Boybay and O. M. Ramahi. Near-field probes using double and single negative media. *Physical Review E - Statistical, Nonlinear, and Soft Matter Physics*, 79(1), 2009.

[102] P. Markos and C.M. Soukoulis. Numerical studies of left-handed materials and arrays of split ring resonators. *Physical Review E (Statistical, Nonlinear, and Soft Matter Physics)*, 65(3):36622–36623, March 2002.

[103] M. Gorkunov, M. Lapine, E. Shamonina, and K.H. Ringhofer. Effective magnetic properties of a composite material with circular conductive elements. *European Physical Journal B*, 28(3):263–271, August 2002.

[104] B. Lahiri, A. Z. Khokhar, R. M. DeLaRue, S. G. McMeekin, and Nigel P. Johnson. Asymmetric split ring resonators for optical sensing of organic materials. 4(3).

[105]

[106] D. R. Smith, J. Gollub, J. J. Mock, W. J. Padilla, and D. Schuring. Calculation and measurement of bianisotropy in a split ring resonator metamaterial. *Journal of Applied Physics*, 100(2):024507–024507–9, July 2006.

[107] L. D. Landau and E. M. Lifshits. *Electrodynamics of Continuous Media*. Oxford, Pergamon Press, second edition, 1984.

[108] I.V. Lindel, A. H. Sihvola, S. A. Tretyakov, and A. J. Vitanen. *Electromagnetic Wave in Chiral and Bi-Isotropic Media*. Artech House, Boston, London, 1994.

[109] A. Serdyukov, I. Semchenko, S. Tretyakov, and A. Sihvola. *Electroagnetics of Bi-anisotropic Materials: Theory and Applications*. Gordon and Breach Science Publishers, Netherlands, AMsterdam, 2001.

[110] T. H. O'Dell. *The Electromagnetics of Magneto-Electric Media*, volume XI of *Selected Topics in Solid State*. North-Holland Publishing Co., Amsterdam, 1970.

[111] Ari H. Sihvola and Ismo V. Lindell. Bi-isotropic constitutive relations. *Microwave and Optical Technology Letters*, 4(8):295–297, March 1991.

[112] Jin Au Kong. Theorems of bianisotropic media. In *Proceedings of the IEEE*, volume 60, pages 1036–1046, September 1972.

[113] S. A. Schelkunoff and H. T. Friis. *Antennas: theory and practise*. John Wiley and Sons Inc, 1952.

[114] T. G. Mackay. Linear and nonlinear homogenized composite medium as metamaterials. *Journal of Electromagnetics*, 25, February 2005.

[115] R. D. Meade J. D. Joannopoulos and J. N. Winn. *Photonic Crystals*. 1995.

[116] M. Boybay and O. M. Ramahi. Evanescent field detection using negative refractive index lenses. In *In proceedings of IEEE International Symposium of Electromagnetic Compatibility*, volume 1B, pages 5507–5510, Jun 2007.

[117] K. Min, T. V. Hong, and D. Kim. A design of a meander line antenna using magneto-dielectric material for RFID system. In *In proceedings of asia-pacific conference on microwave*, volume 4, pages 1–4, December 2005.

[118] A. Buerkle, and K. Sarabandi. TA circularly polarized magneto-dielectric resonator antenna with wideband, multi-resonant response. In *In proceedings of IEEE International Symposium of Electromagnetic Compatibility*, volume 1B, pages 487–490, July 2005.

[119] K. Sarychev and V.M. Shalaev. Electromagnetic field fluctuations and optical nonlinearities in metal-dielectric composites. *Physics Reports*, 335:275–371, March 2000.

[120] G. V. Eleftheriades, A. K. Iyer, and P. C. Kremer. Planar negative refractive index media using periodically lc loaded transmission lines. *IEEE Transaction of Microwave Technology*, 50(12):27022712, December 2002.

[121] P. Ikonen. *Artificial Dielectrics and Magnetics in Microwave Engineering: A Brief Historical Revision*. Radio Laboratory/SMARAD, Helsinki University of Technology.

[122] H. Mosallaei and K. Sarabandi. Reply to comments on design and modeling of patch antenna printed on magneto-dielectric embedded-circuit metasubstrate. *IEEE Transaction on Antenna and Propagation*, 55:29362937, October 2007.

[123] P. Ikonen and S. A. Tretyakov. Comments on design and modeling of patch antenna printed on magneto-dielectric embedded-circuit metasubstrate. *IEEE Transaction on Antenna and Propagation*, 55:29352936, October 2007.

[124] A. Erentok, R. W. Ziolkowski, J. A. Nielsen, R. B. Greegor, C. G. Parazzoli, M. H. Tanielian, Steven A. Cummer, Bogdan-Ioan Popa, Thomas Hand, D. C.

Vier, and S. Schultz. Low frequency lumped element-based negative index metamaterial. *Applied Physics Letters, volume =*.

[125] L. Yousefi, H. Attia, and O. M. Ramahi. Broadband experimental characterization of artificial magnetic materials based on a microstrip line method. *Submitted to physical review E.*

[126] K. N. Rozanova, Z. W. Li, L. F. Chen, and M. Y. Koledintseva. Microwave permeability of co2z composites. *Joirnal of Applied Physics*, 97:013905–1– 013905–7, 2004.

[127] A. L. Adenot, O. Acher, T. Taffary, and L. Longuet. Sum rules on the dynamic permeability of hexagonal ferrites. *Journal of Applied Physics*, 91:7601–7603, 2002.

[128] O. Acher and A. L. Adenot. Bounds on the dynamic properties of magnetic materials. *Physical Review B*, 62(17):11324–11327, November 2000.

[129] H. Mosallaei, and K. Sarabandi. Magneto-dielectrics in electromagnetics: concept and applications. *IEEE Transaction on Antenna and Propagation*, 52(6):1558 – 1567, June 2004.

[130] L. Yousefi, B. Mohajer-Iravani, and O. M. Ramahi. Enhanced Bandwidth Artificial Magnetic Ground Plane for Low Profile Antennas. 6:289 – 292, June 2007.

[131] M. Nagel, M. Först and H. Kurz. THz biosensing devices: fundamentals and technology. 18:601–618, April 2006.

[132] S. M. Kim, F. Hatami, and J. S. Harris. Biomedical terahertz imaging with a quantum cascade laser. *Applied Physics Letters*, 88, 153903, April 2006.

[133] L. Chen, C. K. Ong, and B. T. G. Tan. Cavity perturbation technique for the measurement of permittivity tensor of uniaxially anisotropic dielectrics. *IEEE Transaction of Instruments and Measerments*, 48:1023–1030, December 1999.

[134] A. F. Starr, P. M. Rye, D. R. Smith, and S. Nemat-Nasser. Fabrication and characterization of a negative-refractive-index composite metamaterial. *Physical Review B*, 70:113102, September 2004.

[135] D. R. Smith, D. Schurig, and J. J. Mock. Characterization of a planar artificial magnetic metamaterial surface. *Physical Review E*, 74:036604, September 2006.

[136] N. J. Damascos, R. B. Mack, A. L. Maffett, W. Parmon, and P. L. E. Uslenghi. The inverse problem for biaxial materials. *IEEE Transaction Microwave Theory and Techniques*, 32(4):400–405, April 1984.

[137] H. Chen, J. Zhang, Y. Bai, Y. Luo, L. Ran, Q. Jiang, and J. A. Kong. Experimental retrieval of the effective parameters of metamaterials based on a waveguide method. *Optics Express*, 14(26):12944–12949, December 2006.

[138] J. Baker-Jarvis, E. J. Vanzura, and W. A. Kissick. Improved technique for determining complex permittivity with the transmission/reflection method. *IEEE Transaction Microwave Theory and Techniques*, 38(8):1096–1103, August 1990.

[139] P. Queffelec, P. Gelin, J. Gieraltowski, and J. Loaec. A microstrip device for the broad band simultaneous measurement of complex permeability and permittivity. *IEEE Transactions on Magnetics*, 30(2):224–231, March 1994.

[140] Y. Heping, K.L. Virga, and J.L. Prince. Dielectric constant and loss tangent measurement using a stripline fixture. *IEEE Transaction on Advanced Packaging*, 21:441–446, November 1999.

[141] J. Hinojosa, L. Faucon, P. Queffelec, and F. Huret. S-parameter broadband measurements of microstrip lines and extraction of the substrate intrinsic properties. *Microwave and optical technology letters*, 30(1):65–69, July 2001.

[142] V. Bekker, K. Seemann, and H. Leiste. A new strip line broad-band measurement evaluation for determining the complex permeability of thin ferromagnetic films. *Journal of Magnetism and Magnetic Materials*, 270(3):327–332, 2004.

[143] J. Hinojosa. Permittivity characterization from open-end microstrip line measurements. *Microwave and Optical Technology Letters*, 49(6):1371–1374, June 2007.

[144] R. A. Pucel and D. J. Masse. Microstrip propagation on magnetic substrates. *IEEE Transaction Microwave Theory and Techniques*, 20:304–313, May 1972.

[145] J. E. Dennis and R. B. Schnabel. *Numerical methods for unconstrained optimization and nonlinear equations.* Prentice-Hall, New Jersey, USA, 1983.

[146] H. A. Wheeler. Transmission-line properties of parallel strips separated by a dielectric sheets. *IEEE Transaction Microwave Theory and Techniques*, 13(2):172–185, March 1965.

[147] S. A. Tretyakov. Research on negative refraction and backward-wave media: A historical Perspective. In *EPFL Latsis Symposium on Negative Refraction*, volume 1B, pages 30–35, February 2005.

[148] A. Sihvola. Electromagnetic Emergence in Metamaterials. In *Advances in Electromagnetics of Complex Media and Metamaterials: NATO Science Series II: Mathematics, Physics, and Chemistry*, volume 89, pages 1–17, 2003.

APPENDICES

Appendix A

Loss in Materials

The loss of energy in materials corresponds to the imaginary part of the refractive index, extinction factor. For a plane wave e^{-jkz} traveling in the z-direction, and passing through a medium with the refractive index of[1]

$$n = n' - jn'' \tag{A.1}$$

it is obtained that

$$\mathcal{E}nergy \propto |e^{-jkz}|^2 = |e^{-jnk_0z}|^2 = |e^{-jn'k_0z}e^{-n''k_0z}|^2 = e^{-2nk_0z} \tag{A.2}$$

where k_0 is a wave number in the vacuum. Clearly, from (A.2) the energy decays while the wave is propagating along z-axis in the medium.

In general, the loss presented by n'' is due to electric and magnetic losses. when an electric field is applied to a dielectric, the the electric dipole constituent (molecules) of the dielectric cannot response immediately. Since it takes a certain amount of time to rotate due to inertia of the molecule and friction and collision with other molecules. These collisions damp the energy of the applied field in form of heat. In an oscillating field the dipoles attempt to follow the direction of the field. However, due to many collision the actual energy consumes in the form of heat and creates the *electric loss* in dielectrics. The response of a medium to electric field can be interpreted in terms of

---

[1]In this calculation the engineering notation in oppose to physics notation for refractive index and constitutive parameters is considered and also $j = \sqrt{-1}$.

the polarization, proportional to the applied electric field (i.e., $P(t) = \epsilon\epsilon_0 E(t)$ where ϵ_0 is the intrinsic permittivity of the vacuum). The factor of this proportionality is the permittivity of the medium in form of

$$\epsilon = \epsilon' - j\epsilon'' \tag{A.3}$$

Note that in general the imaginary part of the permittivity includes the conduction loss as well.

The same scenario can be explained about the magnetic loss of the medium. the only difference is the exchange of electric dipoles with magnetic dipoles which respond to magnetic field. Therefore, in the case of the magnetic field the magnetization can be written proportional to the magnetic field while the permeability is the constant of proportionality (i.e., $M(t) = \mu\mu_0 H(t)$ where μ_0 is the intrinsic permeability of the vacuum). Thus, the permeability is also written in complex form

$$\mu = \mu' - j\mu'' \tag{A.4}$$

Therefore, the total loss a medium is related to electric and magnetic losses. The electric and magnetic loss tangent is defined in the following form:

$$\begin{cases} \epsilon = \epsilon'\left(1 - j\frac{\epsilon''}{\epsilon'}\right) = \epsilon'(1 + j\tan\delta_\epsilon) = |\epsilon|e^{j\delta_\epsilon} \\ \mu = \mu'\left(1 - j\frac{\mu''}{\mu'}\right) = \mu'(1 + j\tan\delta_\mu) = |\mu|e^{j\delta_\mu} \end{cases} \tag{A.5}$$

From electromagnetics, the refractive index can be written as:

$$n = \sqrt{\epsilon\mu} \rightarrow \begin{cases} n' = \sqrt{|\epsilon||\mu|}\cos\left(\frac{\delta_\epsilon + \delta_\mu}{2}\right) \\ n'' = -\sqrt{|\epsilon||\mu|}\sin\left(\frac{\delta_\epsilon + \delta_\mu}{2}\right) \end{cases} \tag{A.6}$$

From (A.6) and the definitions of the loss tangent, it can be shown that:

$$\begin{cases} n' = \frac{\pm 1}{\sqrt{2}}\sqrt{\epsilon'\mu' - \epsilon''\mu'' + \sqrt{(\epsilon'^2 + \epsilon''^2)(\mu'^2 + \mu''^2)}} \\ n'' = \frac{\pm 1}{\sqrt{2}}\sqrt{\epsilon''\mu'' - \epsilon'\mu' + \sqrt{(\epsilon'^2 + \epsilon''^2)(\mu'^2 + \mu''^2)}} \end{cases} \tag{A.7}$$

For cases in which $\tan\delta_\epsilon$, $\tan\delta_\mu \ll 1$, the relations in (A.7) are approximated as:

118

$$\begin{cases} n' \simeq \sqrt{\frac{\epsilon'\mu'}{2}}(1 + \frac{1}{8}(\tan\delta_\epsilon^2 + \tan\delta_\mu^2)) \\ n'' \simeq \frac{1}{2}\sqrt{\frac{\epsilon'\mu'}{2}}(\tan\delta_\epsilon + \tan\delta_\mu) \end{cases} \qquad (A.8)$$

Hence, from (A.8) the total loss is approximately proportional to the sum of the electric and magnetic tangent losses.

In addition from energy analysis in dispersive media, one can obtain [10]:

$$\int_0^\infty \mathcal{Q}\mathrm{d}t = \int_0^\infty \omega(\epsilon''(\omega)|\mathbf{E}|^2 + \mu''(\omega)|\mathbf{H}|^2)\mathrm{d}\omega \qquad (A.9)$$

where $\mathcal{Q}$ is heat.

Eq. (A.9) shows that the imaginary parts of the permittivity and permeability functions determine the absorption (dissipation) of energy in the medium. Two terms in (A.9) are referred to *electric* and *magnetic loss*. If the medium is in the thermodynamic equilibrium, due to the law of increase of entropy, the dissipation of energy is defined as evolution of heat, i.e., $\mathcal{Q} > 0$; otherwise, $\mathcal{Q}$ can be negative. Thus, it is proved that the imaginary parts of the effective permittivity and permeability can be negative is some frequency band.

Appendix B

Software Code for the design methodology

A MATLAB software code has been developed to automatically design an AMM meeting desired properties. The code receives the magnetic properties of desired AMM, and generates the fixed intermediate parameters of resistance per unit length R_0, capacitance per unit length C_0, inductance per the area L_0, $\mathcal{K}$ parameter and the sets of interval for output parameter of geometrical factor F, physical factor P, normalized resonance frequency Ω, resonance frequency ω_0, area s, length l, real part of effective permeability μ_{Re} and magnetic tangent loss $\tan \delta$.

B.1   Command Lines

```
function Designer(mu,Tol,BW,f_op,tandel)
\% mu: permeability
\% xi: susceptibility
\% Om: Normalized Omega
\% xi0: susceptinility at lossless
\% F: fraction of occupied area
\% alpha: dissipation factr - alpha=P/F^2

xi=mu-1;
mumax=mu+Tol*mu;
```

```matlab
mumin=mu-mu*Tol;
xsi=(mu*tandel/xi)^2;
xi0=xi*(1+xsi);

F=[0:1e-4:1]';
\% Functions of the Rose curve paper
\% function (19) - maximum mu
Pmax=@(F) 4*F.^3./(8*(mumax-1)-F);P_max0=max(Pmax(1));
\% function (6) xi0 in terms of F and Om xi0=F*Om^2/(1-Om^2)
Om=@(F) sqrt(xi0./(xi0+F));Om_1=Om(F);
F_min0=min(F);F_max0=max(F);
subplot(2,2,1); plot(F,Om_1)
P=@(F) F.^2.*sqrt(xsi./Om(F)).*(1-Om(F).^2)./Om(F); P_1=P(F);
subplot(2,2,2); plot(F,P_1);
fmax = @(F) 4*F.^3+P(F).*F-8*P(F)*(mumax-1);
fmax = @(F) 4*F.^3+P(1).*F-8*P(1)*(mumax-1);

\%figure
F_min1=fzero(fmax,0.5); %F_min1=F_min1(3);% the minimum limit for F
F_max1=F_max0;

\% calculating the resonance frequency
\% parameters
ep_r=2.2;   % substrate's espsilon
b=0.2e-3;      % b = width of the trace,
g=0.8e-3;      % g = distance between traces
t=35e-6;    % t = thickness of the traces

X=20.0e-3;Y=0.8e-3;Z=X; % dimensions of the unit cell
N=1;  % factor for different coupling types (BS = 1, ED = 2)
NN=2; % Number of wire turns

mu0=pi*4e-7;ep0=8.85e-12;sig=5.96e7; % vacuuum and copper electrical properties

A=X*Z; % area of the unit cell
L0=N^2*mu0/Y;             % inductance per unit length
```

```matlab
R0=NN*sqrt(mu0/(2*sig))/b;   % Resistance per unit length
if N==1
    u=tanh(0.5*pi*b/g);  % capacitance per unit length for Broadside-coupled
    C0=(0.25/1)*ep0*ep_r*ellipke(u)/ellipke((sqrt(1-u^2)));
else
    u=g/(2*g+b);        % capacitance per unit length for Edge-coupled
    C0=ep0*ep_r*ellipke(sqrt(1-u^2))/ellipke(u);
end
K=R0/(A^2*L0^2*C0);
\%Parameters=[ep_r;b;g;t;X;Y;Z;A]
Parameters=struct('A',A,'R0',R0,'L0',L0,'u',u,'C0',C0,'K',K)

Input=struct('mu_op',mu,'xi_op',xi,'xi0_op',xi0,'xsi_op',xsi)
Iteration0=struct('F_max',F_max0,'F_min',F_min0,'P_max',P_max0,...
'P_min',min(P_1),'Om_max',1,'Om_min',0)

\% Mu and Tan_delta Function
Alpha = @(f,p) p./f.^2;
XSI = @(f,p,om) Alpha(f,p).^2.*om.^3./(1-om.^2).^2;
XI0 = @(f,om) f.*om.^2./(1-om.^2);
MU = @(f,p,om) 1 + XI0(f,om)./(1 + sqrt(-XSI(f,p,om)));
TAN = @(f,p,om) -imag(MU(f,p,om))./real(MU(f,p,om));

\%%%%%%%%% Iteration 1 %%%%%%%%%%%%%
disp('=========================')
Om_min1=Om(1); % F=1
Om_max1=Om_1(round(F_min1*10000));
P_max1=P(1);
P_min1=P(F_min1);

Iteration1=struct('F_max',F_max1,'F_min',F_min1,'P_max',P_max1,...
'P_min',P_min1,'Om_max',Om_max1,'Om_min',Om_min1)

f_res=((K./P_1).^0.4)/(2*pi);
f_res_min=(f_op+0*BW)/Om_max1;
f_res_max=(f_op+0*BW)/Om_min1;
```

```
Resonance1=struct('f_res_min',f_res_min,'f_res_max',f_res_max)

subplot(2,2,3);
plot(F(round(F_min1*1e4):10001),f_res(round(F_min1*1e4):10001)/(1e9))
axis([F(round(F_min1*1e4)) 1 0.2 1])
%subplot(2,2,4);
f_set=[0:1e-4:F_max1];
check_TAN=real(TAN(f_set,P(f_set),Om(f_set)));

s_min1=F_min1*A;s_max1=F_max1*A;
l_min1=1/(4*pi^2*L0*C0*s_min1*f_res_min^2);
l_max1=1/(4*pi^2*L0*C0*s_max1*f_res_max^2);
Geometry1=struct('small',[s_min1 l_min1],'large',[s_max1 l_max1])

x0_max1=F_min1*Om_max1^2/(1-Om_max1^2);
x0_min1=F_max1*Om_min1^2/(1-Om_min1^2);
xsi_min1=(P_min1/F_min1^2)^2*Om_max1^3/(1-Om_max1^2)^2;
xsi_max1=(P_max1/F_max1^2)^2*Om_min1^3/(1-Om_min1^2)^2;
mu_min1=1+x0_min1*(1+sqrt(-xsi_min1))^(-1);
mu_real_min1=real(mu_min1);tan_min1=-imag(mu_min1)/mu_real_min1;
mu_max1=1+x0_max1*(1+sqrt(-xsi_max1))^(-1);
mu_real_max1=real(mu_max1);tan_max1=-imag(mu_max1)/mu_real_max1;

Mu_Tan1=struct('mu_max',mu_real_max1,'mu_min',mu_real_min1,...
    'tan_max',tan_max1,'tan_min',tan_min1)

\%%%%%%%% Iteration 2 %%%%%%%%%%%%%
disp('=========================')
[v,vinx]=min(abs(f_res-f_res_min)); F_max2=F(vinx); P_max2=P(vinx/1e4);
[v,vinx]=min(abs(f_res-f_res_max)); F_min2=F(vinx); P_min2=P(vinx/1e4);
Om_max2=Om_1(round(F_min2*10000)); Om_min2=Om_1(round(F_max2*10000));

Iteration2=struct('F_max',F_max2,'F_min',F_min2,'P_max',P_max2,...
'P_min',P_min2,'Om_max',Om_max2,'Om_min',Om_min2)
f_res_min=(f_op+0*BW)/Om_max2;
f_res_max=(f_op+0*BW)/Om_min2;
```

```
Resonance2=struct('f_res_min',f_res_min,'f_res_max',f_res_max)


sur=f_set'*A;leng=1./(4*pi^2*L0*C0*sur.*f_res.^2);
subplot(2,2,4)
plot(sur(round(F_min2*1e4):round(F_max2*1e4))...
     ,leng(round(F_min2*1e4):round(F_max2*1e4)))
s_min2=F_min2*A;s_max2=F_max2*A;
l_min2=1/(4*pi^2*L0*C0*s_min2*f_res_min^2);
l_max2=1/(4*pi^2*L0*C0*s_max2*f_res_max^2);
Geometry2=struct('small',[s_min2 l_min2],'large',[s_max2 l_max2])


x0_max2=F_min2*Om_max2^2/(1-Om_max2^2);
x0_min2=F_max2*Om_min2^2/(1-Om_min2^2);
xsi_min2=(P_min2/F_min2^2)^2*Om_max2^3/(1-Om_max2^2)^2;
xsi_max2=(P_max2/F_max2^2)^2*Om_min2^3/(1-Om_min2^2)^2;
mu_min2=1+x0_min2*(1+sqrt(-xsi_min2))^(-1);
mu_real_min2=real(mu_min2);tan_min2=-imag(mu_min2)/mu_real_min2;
mu_max2=1+x0_max2*(1+sqrt(-xsi_max2))^(-1);
mu_real_max2=real(mu_max2);tan_max2=-imag(mu_max2)/mu_real_max2;


Mu_Tan2=struct('mu_max',mu_real_max2,'mu_min',mu_real_min2,...
     'tan_max',tan_max2,'tan_min',tan_min2)


\%%%%%%%%% Iteration 3 %%%%%%%%%%%%%
disp('=========================')
[v,vinx]=min(abs(f_res-f_res_min)); F_max3=F(vinx); P_max3=P(vinx/1e4);
[v,vinx]=min(abs(f_res-f_res_max)); F_min3=F(vinx); P_min3=P(vinx/1e4);
Om_max3=Om_1(round(F_min3*10000)); Om_min3=Om_1(round(F_max3*10000));


Iteration3=struct('F_max',F_max3,'F_min',F_min3,'P_max',P_max3,...
'P_min',P_min3,'Om_max',Om_max3,'Om_min',Om_min3)


f_res_min=(f_op+0*BW)/Om_max3;
f_res_max=(f_op+0*BW)/Om_min3;
Resonance3=struct('f_res_min',f_res_min,'f_res_max',f_res_max)
```

```
s_min3=F_min3*A;s_max3=F_max3*A;
l_min3=1/(4*pi^2*L0*C0*s_min3*f_res_min^2);
l_max3=1/(4*pi^2*L0*C0*s_max3*f_res_max^2);
Geometry3=struct('small',[s_min3 l_min3],'large',[s_max3 l_max3])

x0_max3=F_min3*Om_max3^2/(1-Om_max3^2);
x0_min3=F_max3*Om_min3^2/(1-Om_min3^2);
xsi_min3=(P_min3/F_min3^2)^2*Om_max3^3/(1-Om_max3^2)^2;
xsi_max3=(P_max3/F_max3^2)^2*Om_min3^3/(1-Om_min3^2)^2;
mu_min3=1+x0_min3*(1+sqrt(-xsi_min3))^(-1);
mu_real_min3=real(mu_min3);tan_min3=-imag(mu_min3)/mu_real_min3;
mu_max3=1+x0_max3*(1+sqrt(-xsi_max3))^(-1);
mu_real_max3=real(mu_max3);tan_max3=-imag(mu_max3)/mu_real_max3;

Mu_Tan3=struct('mu_max',mu_real_max3,'mu_min',mu_real_min3,...
    'tan_max',tan_max3,'tan_min',tan_min3)
figure;
freq=[595e6:1e4:625e6]';
Resonance3
MU_REAL=real(MU(F_min3,P_min3,freq/f_res_min));
plot(freq,MU_REAL)
TAN_DEL=TAN(F_min3,P_min3,freq/f_res_min);
hold on
plot(freq,-TAN_DEL,'--')
```

B.2   Sample Output

The output of the code has been tested for a data presented in Table. 5.1.

```
Parameters =
     A: 4.0000e-004
    R0: 0.0010
    L0: 0.0016
     u: 0.3737
    C0: 3.1367e-012
```

```
    K: 8.2916e+020

Input =
     mu_op: 9
     xi_op: 8
    xi0_op: 8.0253
    xsi_op: 0.0032

Iteration0 =
     F_max: 1
     F_min: 0
     P_max: 0.0601
     P_min: 0
    Om_max: 1
    Om_min: 0
=========================
Iteration1 =
     F_max: 1
     F_min: 0.4852
     P_max: 0.0068
     P_min: 7.8878e-004
    Om_max: 0.9711
    Om_min: 0.9430

Resonance1 =
    f_res_min: 6.1787e+008
    f_res_max: 6.3628e+008

Geometry1 =
    small: [1.9407e-004 0.0694]
    large: [4.0000e-004 0.0317]

Mu_Tan1 =
     mu_max: 9.0011
     mu_min: 9.0000
    tan_max: 0.0500
```

```
      tan_min: 0.0500
===========================
Iteration2 =
     F_max: 0.5038
     F_min: 0.4916
     P_max: 8.8325e-004
     P_min: 8.2093e-004
    Om_max: 0.9707
    Om_min: 0.9700

Resonance2 =
    f_res_min: 6.1810e+008
    f_res_max: 6.1854e+008

Geometry2 =
    small: [1.9664e-004 0.0684]
    large: [2.0152e-004 0.0667]

Mu_Tan2 =
     mu_max: 9.0016
     mu_min: 9.0015
    tan_max: 0.0500
    tan_min: 0.0500
===========================
Iteration3 =
     F_max: 0.5037
     F_min: 0.5034
     P_max: 8.8272e-004
     P_min: 8.8116e-004
    Om_max: 0.9700
    Om_min: 0.9700

Resonance3 =
    f_res_min: 6.1853e+008
    f_res_max: 6.1854e+008
```

```
Geometry3 =
    small: [2.0136e-004 0.0667]
    large: [2.0148e-004 0.0667]

Mu_Tan3 =
     mu_max: 9.0015
     mu_min: 9.0015
    tan_max: 0.0500
    tan_min: 0.0500

Resonance3 =
    f_res_min: 6.1853e+008
```

Appendix C

The Effective Parameters Extraction

In this appendix, a proper formulation for determining the constitutive effective parameters of an AMM is introduce. Regardless of the extraction method, the parameters has to be calculated uniquely. Practically, the parameters which are available in experiments are the reflection coefficient and transmission coefficient of the field power. Inverting the classical relations for the reflection and transmission from a slab of homogenous material of thickness d [73], [74]:

$$\frac{1}{T} = \left[\cos(nkd) - \frac{i}{2}\left(z + \frac{1}{z}\right)\sin(nkd)\right]e^{ikd} \tag{C.1}$$

$$\frac{R}{T} = -\frac{1}{2}i\left(z - \frac{1}{z}\right)\sin(nkd)e^{ikd} \tag{C.2}$$

the refractive index n and the impedance Z are calculated as:

$$n = \pm\cos^{-1}\left(\frac{1 - r^2 - t^2}{2t}\right) \tag{C.3}$$

$$z = \pm\sqrt{\frac{(1+r)^2 - t^2}{(1-r)^2 - t^2}} \tag{C.4}$$

where $r = R$ and $t = Te^{ikd}$, from which the permitivity and permeability parameters can be calculated as:

$$
\begin{cases}
\epsilon = \frac{n}{z} \\
\mu = nz
\end{cases}
\tag{C.5}
$$

Note that in the above relations complex functions are are with multiple branches. This fact leads to ambiguities in determination of n and z and accordingly ϵ and μ. However, it can be resolved by additional knowledge from materials. from Kramers-Kronig relation (see Appendix A), it can be shown that for passive materials:

$$
\begin{cases}
\mathcal{I}m(n) > 0 \\
\mathcal{R}e(z) > 0
\end{cases}
\tag{C.6}
$$

Therefore, for $\mathcal{I}m(n)$, we get:

$$
\mathcal{I}m(n) = \pm \left\{ \frac{1}{kd} \cos^{-1} \left| \frac{1 - r^2 - t^2}{2t} \right| \right\}
\tag{C.7}
$$

For calculating (C.7), we choose the sign which is consistent with condition in (C.6). Note that the requirement that $\mathcal{I}m(n) > 0$, uniquely identifies the sign of $\mathcal{R}e(n) > 0$.

Appendix D

Software Code for an Inclusion Reconfiguration

A Matlab software code has been developed to automatically characterize Rose curve, Corrugated rectangular curve and Sine oval Curve. The code receives the area and perimeter of a curve in general and produces a set of possible curves that possess the same area and perimeter of an input. The code also has an option of considering the length of gap in the contour and calculate the proposer length of the metallic trace. In fact, the output is in a form of data set corresponding to the parameters of Rose curve, corrugated rectangle curve and Sine oval curve. Moreover, the code inversely can receive the parameters of the Rose curve, corrugated rectangle curve and Sine oval curve and calculate the area and perimeter of the corresponding figure. In addition, this code can be linked to the code developed for design of AMMs and create a full package for design of AMMs meeting desired magnetic properties.

D.1   Command Lines

```
function [amp,r]=Rose_curve(area,perimeter,lower,steps,upper,h)
for n=lower:steps:upper
    r=sqrt(area/pi);rr=r;
    minperimeter=2*r*pi;
    step = 1e-6;
```

```
a=0;
precision1=1;
precision2=1;
b=[0:step:10e-3];
while precision1>1e-10
    while precision2>1e-12
        anlen=[];
        sizeb=size(b,2);
        for u=1:sizeb
            a=b(u);
            nlen=[];
            th=h:.005:2*pi-h;
            ro=r+a*sin(n*th);
            [x,y]=pol2cart(th,ro);
            sx=size(x,2);len=0;
            for i=2:sx
                dl=sqrt((x(i)-x(i-1))^2+(y(i)-y(i-1))^2);
                len=len+dl;
            end
            len=len+sqrt((x(1)-x(sx))^2+(y(1)-y(sx))^2);
            nlen=[nlen len];
            anlen=[anlen;nlen];
        end
        [precision2,index]=min(abs(anlen-perimeter));
        amp1=b(index-1);amp2=b(index+1);step=step/100;
        b=[amp1:step:amp2];
    end
    amp=b(index);
    r=sqrt((area-pi*amp^2/2)/pi);
    precision1=abs(area-(pi*r^2+pi*amp^2/2));
    precision2;
end
maxdim=2*(r+amp);
msg=sprintf('n=%d \tamp=%.8g \tr=%.8g \tmaxdim=%.5g',n,amp,r,maxdim);
disp(msg);
end
```

D.2 Sample Output

The output of the code has been tested for thedata presented in (6.5). Units are in meters.

```
Rose_curve(200e-6,70e-3,3,1,13,1e-3)


n=3  amp=0.0037266995  r=0.0075311243  maxdim=0.022516
n=4  amp=0.0028173226  r=0.0077261455  maxdim=0.021087
n=5  amp=0.0022620675  r=0.0078168729  maxdim=0.020158
n=6  amp=0.0018887714  r=0.0078662728  maxdim=0.01951
n=7  amp=0.0016208741  r=0.0078960978  maxdim=0.019034
n=8  amp=0.0014193677  r=0.0079154706  maxdim=0.01867
n=9  amp=0.0012623406  r=0.0079287594  maxdim=0.018382
n=10  amp=0.0011365525  r=0.0079382682  maxdim=0.01815
n=11  amp=0.0010335368  r=0.0079453054  maxdim=0.017958
n=12  amp=0.00094762989  r=0.0079506588  maxdim=0.017797
n=13  amp=0.00087490059  r=0.0079548257  maxdim=0.017659
```